Laying the foundation of the effective-one-body waveform models SEOBNRv5: Improved accuracy and efficiency for spinning nonprecessing binary black holes

Lorenzo Pompili®, ^{1,*} Alessandra Buonanno®, ^{1,2} Héctor Estellés®, ¹ Mohammed Khalil®, ^{3,1,2} Maarten van de Meent®, ^{1,4} Deyan P. Mihaylov, ¹ Serguei Ossokine®, ¹ Michael Pürrer®, ^{5,6,1} Antoni Ramos-Buades®, ¹ Ajit Kumar Mehta, ^{7,1} Roberto Cotesta, ⁸ Sylvain Marsat, ⁹ Michael Boyle, ¹⁰ Lawrence E. Kidder®, ¹⁰ Harald P. Pfeiffer, ¹ Mark A. Scheel, ¹¹ Hannes R. Rüter®, ¹² Nils Vu®, ¹¹ Reetika Dudi®, ¹ Sizheng Ma, ¹¹ Keefe Mitman®, ¹¹ Denyz Melchor®, ¹³ Sierra Thomas®, ^{13,14} and Jennifer Sanchez¹⁵ ¹Max Planck Institute for Gravitational Physics (Albert Einstein Institute), Am Mühlenberg 1, Potsdam 14476, Germany ²Department of Physics, University of Maryland, College Park, Maryland 20742, USA ³Perimeter Institute for Theoretical Physics, 31 Caroline Street North, Waterloo, Ontario N2L 2Y5, Canada ⁴Niels Bohr International Academy, Niels Bohr Institute, Blegdamsvej 17, 2100 Copenhagen, Denmark ⁵Department of Physics, East Hall, University of Rhode Island, Kingston, Rhode Island 02881, USA ⁶Center for Computational Research, Tyler Hall, University of Rhode Island, Kingston, Rhode Island 02881, USA 7 Department of Physics, University of California, Santa Barbara, California 93106, USA ⁸William H. Miller III Department of Physics and Astronomy, Johns Hopkins University, 3400 North Charles Street, Baltimore, Maryland, 21218, USA ⁹Laboratoire des 2 Infinis—Toulouse (L2IT-IN2P3), Université de Toulouse, CNRS, UPS, F-31062 Toulouse Cedex 9, France ¹⁰Cornell Center for Astrophysics and Planetary Science, Cornell University, Ithaca, New York 14853, USA ¹¹Theoretical Astrophysics 350-17, California Institute of Technology, Pasadena, California 91125, USA ¹²CFisUC, Department of Physics, University of Coimbra, 3004-516 Coimbra, Portugal ¹³Nicholas and Lee Begovich Center for Gravitational Wave Physics and Astronomy, California State University Fullerton, Fullerton California 92831 USA ¹⁴Department of Physics, Syracuse University, Syracuse, New York 13244, USA ¹⁵Center for Interdisciplinary Exploration and Research in Astrophysics (CIERA), Northwestern University, 1800 Sherman Ave, Evanston, Illinois 60201, USA

(Received 11 April 2023; accepted 18 September 2023; published 15 December 2023)

We present SEOBNRv5HM, a more accurate and faster inspiral-merger-ringdown gravitational waveform model for quasicircular, spinning, nonprecessing binary black holes within the effective-one-body (EOB) formalism. Compared to its predecessor, SEOBNRv4HM, the waveform model (i) incorporates recent high-order post-Newtonian results in the inspiral, with improved resummations, (ii) includes the gravitational modes $(\ell, |m|) = (3, 2), (4, 3),$ in addition to the (2, 2), (3, 3), (2, 1), (4, 4), (5, 5) modes already implemented in SEOBNRv4HM, (iii) is calibrated to larger mass ratios and spins using a catalog of 442 numerical-relativity (NR) simulations and 13 additional waveforms from black-hole perturbation theory, and (iv) incorporates information from second-order gravitational self-force in the nonspinning modes and radiation-reaction force. Computing the unfaithfulness against NR simulations, we find that for the dominant (2,2) mode the maximum unfaithfulness in the total mass range $10-300M_{\odot}$ is below 10^{-3} for 90% of the cases (38% for SEOBNRv4HM). When including all modes up to $\ell = 5$ we find 98% (49%) of the cases with unfaithfulness below 10^{-2} (10^{-3}), while these numbers reduce to 88% (5%) when using SEOBNRv4HM. Furthermore, the model shows improved agreement with NR in other dynamical quantities (e.g., the angular momentum flux and binding energy), providing a powerful check of its physical robustness. We implemented the waveform model in a high-performance Python package (pySEOBNR), which leads to evaluation times faster than SEOBNRv4HM by a factor of 10 to 50, depending on the configuration, and provides the flexibility to easily include spin-precession and

Published by the American Physical Society under the terms of the Creative Commons Attribution 4.0 International license. Further distribution of this work must maintain attribution to the author(s) and the published article's title, journal citation, and DOI. Open access publication funded by the Max Planck Society.

^{*}lorenzo.pompili@aei.mpg.de

eccentric effects, thus making it the starting point for a new generation of EOBNR waveform models (SEOBNRv5) to be employed for upcoming observing runs of the LIGO-Virgo-KAGRA detectors.

DOI: 10.1103/PhysRevD.108.124035

I. INTRODUCTION

Gravitational-wave (GW) astronomy has rapidly advanced since the first detection of GWs from a binary black-hole (BBH) merger in 2015 [1], recording about ten events in the initial and second observing runs [2,3] and about 100 events in the third observing run [4–8] of the LIGO-Virgo detectors [9–13]. With upcoming upgrades of existing detectors and new facilities on the ground, such as Einstein Telescope [14] and Cosmic Explorer [15,16], and the space-based mission LISA [17], it is expected that the merger rates of compact binaries will significantly increase. Accurately modeling the GWs emitted by binary systems is essential to take full advantage of the discovery potential of ever more sensitive GW detectors, enriching our knowledge of astrophysics, cosmology, gravity, and fundamental physics.

Numerical relativity (NR) simulations [18–20] can provide the most accurate waveforms, but they are computationally expensive, which makes it important to develop waveform models that combine analytical approximation methods with NR results. The most commonly used approaches to build complete inspiral-merger-ringdown (IMR) waveform models of compact binaries are the NR surrogate, phenomenological, and effective-one-body (EOB) families. NR surrogate models [21–30] interpolate NR waveforms in a reduced-order representation; thus they provide us with the most accurate models for higher multipoles [24] and spin precession [23,25], but they are limited to the region of parameter space where NR simulations exist. Furthermore, their length currently restricts their use to binaries with total masses $\gtrsim 60 M_{\odot}$, unless the NR surrogates are hybridized to an inspiral approximant, such as EOB or post-Newtonian (PN) waveforms [24,30]. Inspiral-merger-ringdown phenomenological models (IMRPhenom) [31-50] combine PN and EOB waveforms for the inspiral with fits to NR results for the late inspiral and merger-ringdown parts of the waveform, and aim to be as fast as possible for data-analysis purposes. The EOB formalism [51–55] combines information from several analytical approximation methods with NR results. It maps the dynamics of a compact binary to that of a test mass (or test spin) in a deformed Schwarzschild (or Kerr) background, with the deformation parameter being the symmetric mass ratio. EOB waveform models of BBHs have been constructed for nonspinning [51–53,56–64], spinning [54,55,65–85], and eccentric binaries [86–92]. Matter effects have also been incorporated in EOB models in Refs. [93-99]. To reduce the computational cost of EOB waveforms, surrogate or reduced-order models have been developed in Refs. [100–109]. Parameter-estimation codes based on machine-learning methods, notably neural posterior estimation, are also available to speed up inference studies [110,111]. More specifically, there are currently two state-of-the-art families of EOB waveform models: SEOBNR (e.g., see Refs. [77,78,81,91,105,112]) and TEOBResumS (e.g., see Refs. [64,83,85,88,113,114]). Here, we focus on the former.

The expected increase in sensitivity during the fourth observing run (O4) [115] of the LIGO-Virgo-KAGRA (LVK) Collaboration [9,10,116], which is planned to start in May 2023, will likely allow us to observe events in unexplored regions of parameter space with high spins and large mass ratios. In these regions of parameter space state-of-the-art waveform models tend to disagree [49,77,81,117,118], as they are mostly calibrated to NR simulations having both moderate spins, say $\lesssim 0.5$, and comparable mass ratios, say 1-4, and waveform modeling systematics could be comparable to statistical errors. In order to improve the accuracy of EOB models, one takes advantage of the strong-field information from NR simulations, and also includes the latest results from the main analytical approximation methods, that is PN, post-Minkowskian, and gravitational self-force theory [119–125].

Within the SEOBNR family of EOB models, we present SEOBNRv5HM, a new IMR multipolar waveform model for quasicircular, spinning, nonprecessing BBHs. In SEOBNRv5HM we employ the most recent PN results for the three main components of the dynamics and gravitational radiation: the Hamiltonian [73,74,126], the radiation-reaction (RR) force, and waveform modes [127]. Furthermore, we directly incorporate information from second-order self-force (2GSF) [125,128,129] in the modes and RR force. SEOBNRv5HM includes the gravitational modes $(\ell, |m|) = (3, 2), (4, 3)$, in addition to the $(\ell, |m|) = (2, 2), (3, 3), (2, 1), (4, 4), (5, 5)$ modes already implemented in SEOBNRv4HM [78], and models the mode mixing in the merger ringdown of the (3,2), (4,3)modes. We calibrate SEOBNRv5HM to 442 NR waveforms, all produced with the pseudo-Spectral Einstein code (SpEC) of the Simulating eXtreme Spacetimes (SXS) Collaboration [21,22,24,25,30,77,130–140], except for a simulation with mass ratio and (dimensionless spins)

¹SEOBNRv5HM is publicly available through the Python package pySEOBNR https://git.ligo.org/waveforms/software/pyseobnr. Stable versions of pySEOBNR are published through the Python Package Index (PyPI), and can be installed via pip install pyseobnr.

 $q=8,\chi_1=0.85,\chi_2=0.85$ produced with the Einstein Toolkit code [78,141]. We also incorporate information from 13 waveforms computed by solving the Teukolsky equation in the framework of black hole (BH) perturbation theory [142,143], with mass ratio $q=10^3$ and dimensionless spins values in the range $-0.99 \le \chi \le 0.99$. This greatly extends the NR calibration coverage with respect to SEOBNRv4 [77], which used 140 NR waveforms, especially toward larger mass ratios and spins. Indeed, we include several NR simulations with mass ratios between 10 and 20, in a region of parameter space where no simulations were available when SEOBNRv4 was developed.

We validate the model by computing the unfaithfulness against NR simulations, and by comparing several dynamical quantities, such as the angular-momentum flux and binding energy, providing an important check of its physical robustness and giving confidence of its reliability when extrapolating it outside the NR calibration region. Computational efficiency is also a key aspect of waveform models, as Bayesian parameter estimation of GW events with stochastic sampling techniques typically requires millions of waveform evaluations. For this purpose, we implemented SEOBNRv5HM in a flexible, high-performance Python package (pySEOBNR [144]), which leads to evaluation times faster than SEOBNRv4HM. We then show that the SEOBNRv5HM model can be employed for GW parameter estimation with standard stochastic samplers thanks to its high computational efficiency. We perform Bayesian inference studies using SEOBNRv5HM by injecting synthetic NR signals in zero noise, and by reanalyzing GW events from previous observing runs. Further speedup in waveform evaluation time of about 1 order of magnitude can be obtained by surrogate models. We build a frequency domain reduced-order model of SEOBNRv5, following Ref. [105].

This work is part of a series of articles [125,126,144,145] describing the SEOBNRv5 family for O4 [115], and it is organized as follows. After an introduction to the notation used in this paper, in Sec. III we describe the SEOBNRv5 aligned-spin Hamiltonian and equations of motion. In Sec. IV we outline the construction of the multipolar waveform modes, highlighting improvements and differences with respect to SEOBNRv4HM, and in Sec. V we illustrate how SEOBNRv5HM is calibrated against 442 NR simulations. In Sec. VI we compare the accuracy of SEOBNRv5HM, and of other state-of-the-art waveform models, against NR simulations, and investigate the regions of parameter space where they exhibit the largest differences from NR waveforms and from each other. We also present comparisons against NR results for the angular-momentum flux and binding energy of SEOBNRv4 and SEOBNRv5. In Sec. VII we study the model's accuracy in Bayesian inference analyses, by performing a synthetic NR injection in zero noise and by analyzing GW events observed by the LVK detectors. In Sec. VIII we outline the performance of a frequency-domain reduced-order model of SEOBNRv5. Section IX summarizes our main conclusions and discusses future work. Finally, Appendixes A and B provide the complete expression for the Hamiltonian and the multipolar waveform modes used for this work. In Appendixes C and D, we provide all expressions for the fits to NR simulations entering the construction of the waveform modes. Appendix E presents some tests of the robustness of the calibration pipeline to NR waveforms, and in Appendix F we check the potential impact of including additional corrections in the RR force for a specific binary configuration. Finally, in Appendix G, we extend the comparison of Sec. VI to the state-of-the-art time-domain phenomenological model IMRPhenomTHM [47,48].

II. NOTATION

We use natural units in which c = G = 1. We consider a binary with masses m_1 and m_2 , with $m_1 \ge m_2$, and define the following combinations of the masses:

$$M \equiv m_1 + m_2, \qquad \mu \equiv \frac{m_1 m_2}{M}, \qquad \nu \equiv \frac{\mu}{M},$$

$$\delta \equiv \frac{m_1 - m_2}{M}, \qquad q \equiv \frac{m_1}{m_2}. \tag{1}$$

For binaries with nonprecessing spins of magnitude S_1 and S_2 , we define the dimensionless spins

$$\chi_{\rm i} \equiv \frac{a_{\rm i}}{m_{\rm i}} = \frac{S_{\rm i}}{m_{\rm i}^2},\tag{2}$$

where i = 1, 2, and define the following spin variables:

$$\chi_S \equiv \frac{\chi_1 + \chi_2}{2}, \qquad \chi_A \equiv \frac{\chi_1 - \chi_2}{2},$$

$$\chi_{\text{eff}} \equiv \frac{(m_1 \chi_1 + m_2 \chi_2)}{m_1 + m_2},$$

$$a_{\pm} \equiv a_1 \pm a_2 = m_1 \chi_1 \pm m_2 \chi_2.$$
(3)

The relative position and momentum vectors, in the binary's center-of-mass frame, are denoted \mathbf{r} and \mathbf{p} , with

$$p^2 = p_r^2 + \frac{L^2}{r^2}, \qquad p_r = \boldsymbol{n} \cdot \boldsymbol{p}, \qquad \boldsymbol{L} = \boldsymbol{r} \times \boldsymbol{p}, \quad (4)$$

where $n \equiv r/r$, and L is the orbital angular momentum with magnitude L. Since in this work we discuss nonprecessing (or aligned-spin) BHs, we consider equatorial orbits, and use polar-coordinate phase-space variables (r, ϕ, p_r, p_ϕ) , where the angular momentum reduces to $L = p_\phi$.

The orbital frequency is denoted Ω , and we define the dimensionless frequency parameter $v_{\Omega} \equiv (M\Omega)^{1/3}$. We also often use $u \equiv M/r$ instead of r.

III. THE SEOBNRV5 ALIGNED-SPIN HAMILTONIAN AND EQUATIONS OF MOTION

In the EOB formalism [51–55], the two-body dynamics is mapped onto the effective dynamics of a test body in a deformed Schwarzschild or Kerr background, with the deformation parametrized by the symmetric mass ratio ν . The energy map relating the effective Hamiltonian $H_{\rm eff}$ and the two-body EOB Hamiltonian $H_{\rm EOB}$ is given by

$$H_{\rm EOB} = M\sqrt{1 + 2\nu \left(\frac{H_{\rm eff}}{\mu} - 1\right)}.$$
 (5)

The generic-spin Hamiltonian we use in SEOBNRv5 is based on that of a *test mass* in a deformed Kerr background [54,66,67,71–74,126]. In contrast, the SEOBNRv4 [77,78,81] Hamiltonian was based on the one of a *test spin* in a deformed Kerr background [70,146,147].

The SEOBNRv5 Hamiltonian includes most of the 5PN nonspinning contributions, together with spin-orbit (SO) information up to the next-to-next-to-leading order (NNLO), spin-spin (SS) information to NNLO, as well as cubic- and quartic-in-spin terms at leading order (LO), corresponding to all PN information up to 4PN order for precessing spins. More details about the derivation of the generic-spin Hamiltonian, together with the full expressions, are given in Ref. [126]. Here, we summarize the structure of the aligned-spin Hamiltonian, and its zero-spin limit, highlighting where NR calibration parameters enter the expressions.

A. Nonspinning effective Hamiltonian

The effective Hamiltonian for nonspinning (noS) binaries can be written as

$$H_{\rm eff}^{\rm noS} = \sqrt{p_{r_*}^2 + A_{\rm noS}(r) \left[\mu^2 + \frac{p_{\phi}^2}{r^2} + Q_{\rm noS}(r, p_{r_*}) \right]}, \qquad (6)$$

where we use the tortoise coordinate p_{r_*} instead of p_r , since it improves the stability of the equations of motion during the plunge and close to merger [67,148]. For nonspinning binaries, r_* is defined by

$$\frac{dr_*}{dr} = \frac{1}{\xi(r)}, \qquad \xi(r) \equiv A_{\rm noS}(r) \sqrt{\bar{D}_{\rm noS}(r)}, \qquad (7)$$

with the conjugate momentum p_r , given by

$$p_{r_*} = p_r \xi(r). \tag{8}$$

For the potentials $A_{\rm noS}(r)$ and $\bar{D}_{\rm noS}(r)$, we use the 5PN results of Refs. [149,150], which are complete except for two quadratic-in- ν coefficients. The 5PN Taylor-expanded $A_{\rm noS}$ is given by

$$A_{\text{noS}}^{\text{Tay}}(u) = 1 - 2u + 2\nu u^3 + \nu \left(\frac{94}{3} - \frac{41\pi^2}{32}\right) u^4$$

$$+ \left[\nu \left(\frac{2275\pi^2}{512} - \frac{4237}{60} + \frac{128\gamma_E}{5} + \frac{256\ln 2}{5}\right) + \left(\frac{41\pi^2}{32} - \frac{221}{6}\right)\nu^2 + \frac{64}{5}\nu \ln u\right] u^5$$

$$+ \left[\nu a_6 + \left(-\frac{144\nu^2}{5} - \frac{7004\nu}{105}\right) \ln u\right] u^6, \qquad (9)$$

where $u \equiv M/r$, and we replace the coefficient of u^6 , except for the log part, by the parameter a_6 , which is calibrated to NR simulations.

The 5PN Taylor-expanded $\bar{D}_{\rm noS}(r)$ potential is given by Eq. (A1) in Appendix A. The 5.5PN contributions to $A_{\rm noS}(r)$ and $\bar{D}_{\rm noS}(r)$ are known from Refs. [63,150]; however, since we Padé resum these potentials (as explained in Sec. V), we find it more convenient to stop at 5PN. For the $Q_{\rm noS}(r)$ potential, we use the full 5.5PN expansion, which is also expanded in eccentricity to $\mathcal{O}(p_r^8)$, as given by Eq. (A2).

The calibration parameter a_6 is a function of ν ; to determine its value in the limit $\nu \to 0$, we use the GSF results of Refs. [151–153] for the frequency shift of the innermost stable circular orbit (ISCO), which is given by

$$M\Omega_{\rm ISCO}^{\rm 1SF} = 6^{-3/2} (1 + C_{\Omega}/q),$$

 $C_{\Omega} = 1.25101539 \pm 4 \times 10^{-8}.$ (10)

The ISCO can be computed from the EOB Hamiltonian by solving $(\partial H/\partial r)_{|_{p_r=0}}=0=(\partial^2 H/\partial r^2)_{|_{p_r=0}}$ for r and p_ϕ . We find the value of a_6 that gives the best agreement with $\Omega_{\rm ISC}^{\rm ISF}$ is

$$a_6|_{\nu\to 0} \simeq 39.0967.$$
 (11)

The fit we use for $a_6(\nu)$ is given by Eq. (78) below.

B. Aligned-spin effective Hamiltonian

For aligned spins, the effective Hamiltonian reduces to the equatorial Kerr Hamiltonian in the test-particle limit (TPL), with the Kerr spin a mapped to the binary's spins via $a = a_1 + a_2 \equiv a_+$. To include 4PN information for spinning binaries and arbitrary mass ratios, we use the following Ansatz [126]:

$$\begin{split} H_{\text{eff}}^{\text{align}} &\equiv H_{\text{odd}} + H_{\text{even}}, \\ &= \frac{M p_{\phi}(g_{a_{+}} a_{+} + g_{a_{-}} \delta a_{-}) + \text{SO}_{\text{calib}} + G_{a^{3}}^{\text{align}}}{r^{3} + a_{+}^{2}(r + 2M)} \\ &+ \left[A^{\text{align}} \left(\mu^{2} + p^{2} + B_{np}^{\text{align}} p_{r}^{2} + B_{np}^{\text{Kerr eq}} \frac{p_{\phi}^{2} a_{+}^{2}}{r^{2}} + Q^{\text{align}} \right) \right]^{1/2}, \end{split}$$
(12)

where the first term on the right-hand side only includes the odd-in-spin contributions (in the numerator), while the second term (square root) includes the even-in-spin contributions.

The gyrogravitomagnetic factors $g_{a_+}(r)$ and $g_{a_-}(r)$ in the SO part of the Hamiltonian (12) are sometimes chosen to be in a gauge such that they are functions of 1/r and p_r^2 only [66,71], though Refs. [69,70] made different choices. In building the SEOBNRv5 model, we find better agreement with NR waveforms when using a gauge in which $g_{a_+}(r)$ and $g_{a_-}(r)$ depend only on 1/r and p_{ϕ}^2/r^2 . The 4.5PN SO coupling was derived in Refs. [154–157], and can be included in the gyrogravitomagnetic factors [see Eqs. (30a) and (30b) in Ref. [126]]. However, when calibrating to NR simulations, we find that using a calibration term at 5.5PN has a small effect on the dynamics, and thus we only include the 3.5PN SO information [given in Eq. (A3)] with a 4.5PN SO calibration term of the form

$$SO_{calib} = \nu d_{SO} \frac{M^4}{r^3} p_{\phi} a_+. \tag{13}$$

Furthermore, the function $G_{a^3}^{\rm align}(r)$ in Eq. (12) contains S³ corrections. The nonspinning and SS contributions are included in $A^{\rm align}(r)$, $B_{np}^{\rm align}(r)$, and $Q^{\rm align}(r)$, with no S⁴ corrections needed since the Kerr Hamiltonian reproduces all even-in-spin leading PN orders for binary BHs [158]. Explicit expressions for the functions in the Hamiltonian are provided in Appendix A (and also in Ref. [126]).

When using tortoise coordinates for spinning binaries, a convenient choice for $\xi(r)$ is

$$\xi(r) = \frac{\sqrt{\bar{D}_{\text{noS}}}(A_{\text{noS}} + a_+^2/r^2)}{1 + a_+^2/r^2},\tag{14}$$

which is similar to what was used in SEOBNRv4 [67,75] except for the different resummation and PN orders in $A_{\rm noS}$ and $\bar{D}_{\rm noS}$. In the $\nu \to 0$ limit, ξ reduces to the Kerr value $(dr/dr_*) = (r^2 - 2Mr + a_+^2)/(r^2 + a_+^2)$.

C. Equations of motion and radiation-reaction force

The equations of motion for aligned spins, in terms of p_{r_*} , are given by Eq. (10) of Ref. [61], and read as

$$\dot{r} = \xi \frac{\partial H}{\partial p_{r_*}}, \qquad \dot{p}_{r_*} = -\xi \frac{\partial H}{\partial r} + \frac{p_{r_*}}{p_{\phi}} \mathcal{F}_{\phi},$$

$$\dot{\phi} = \frac{\partial H}{\partial p_{\phi}}, \qquad \dot{p}_{\phi} = \mathcal{F}_{\phi}, \tag{15}$$

where the RR force \mathcal{F}_{ϕ} is obtained by summing the GW modes in factorized form [58,59,148,159], $h_{\ell m}^{\rm F}$, which we define in Sec. IVA, that is,

$$\mathcal{F}_{\phi} \equiv -\frac{\Omega}{8\pi} \sum_{\ell=2}^{8} \sum_{m=1}^{\ell} m^2 |d_L h_{\ell m}^{\rm F}|^2, \tag{16}$$

where Ω is the orbital frequency, and d_L is the luminosity distance of the binary to the observer.

The equations of motion can be written more explicitly as follows:

$$\dot{r} = \frac{MA^{\text{align}}}{2H_{\text{EOB}}H_{\text{even}}} \left[\frac{2p_{r_*}}{\xi} \left(1 + B_{np}^{\text{align}} \right) + \xi \frac{\partial Q^{\text{align}}}{\partial p_{r_*}} \right], \quad (17a)$$

$$\dot{\phi} = \frac{M}{H_{\text{EOB}}} \left[p_{\phi} \frac{\partial \bar{H}_{\text{odd}}}{\partial p_{\phi}} + \bar{H}_{\text{odd}} + \frac{A^{\text{align}}}{H_{\text{even}}} \frac{p_{\phi}}{r^2} (1 + B_{npa}^{\text{Kerr eq}} a_+^2) \right], \tag{17b}$$

$$\dot{p}_{r_*} = -\frac{M\xi}{H_{\rm EOB}} \left(\frac{\partial H_{\rm even}}{\partial r} + p_{\phi} \frac{\partial \bar{H}_{\rm odd}}{\partial r} \right) + \frac{p_{r_*}}{p_{\phi}} \mathcal{F}_{\phi}, \tag{17c}$$

where we define $\bar{H}_{\rm odd} \equiv H_{\rm odd}/p_{\phi}$. The derivative of $H_{\rm even}$ is given by

$$\frac{\partial H_{\text{even}}}{\partial r} = \frac{1}{2H_{\text{even}}} \left(K_0 p_{\phi}^2 + K_1 \right),\tag{18a}$$

$$K_{0} \equiv A^{\text{align}} \left[-\frac{2}{r^{3}} (1 + B_{npa}^{\text{Kerr eq}} a_{+}^{2}) + \frac{a_{+}^{2}}{r^{2}} \frac{dB_{npa}^{\text{Kerr eq}}}{dr} \right] + \frac{dA^{\text{align}}}{dr} \left(\frac{1}{r^{2}} + \frac{a_{+}^{2}}{r^{2}} B_{npa}^{\text{Kerr eq}} \right),$$
(18b)

$$K_{1} \equiv A^{\text{align}} \left\{ \frac{p_{r_{*}}^{2}}{\xi^{2}} \left[\frac{dB_{np}^{\text{align}}}{dr} - \frac{2}{\xi} \frac{d\xi}{dr} (1 + B_{np}^{\text{align}}) \right] + \frac{\partial Q^{\text{align}}}{\partial r} \right\} + \frac{dA^{\text{align}}}{dr} \left[\mu^{2} + \frac{p_{r_{*}}^{2}}{\xi^{2}} (1 + B_{np}^{\text{align}}) + Q^{\text{align}} \right].$$
(18c)

When evolving the equations of motion, we use the same quasicircular adiabatic initial conditions derived in Ref. [55], and then integrate numerically Eq. (15) to solve for the binary dynamics.

In SEOBNRv5, one can also employ the postadiabatic (PA) approximation for the inspiral dynamics, which allows for speeding up the evaluation of the model, especially for very long waveforms [62,160]. This technique has been

used extensively with great success in the TEOBResumS family of models (see, e.g., Refs. [85,113,114,160,161]), and recently also in the SEOBNRv4HM_PA model [112]. To obtain explicit algebraic equations for the momenta, we follow the same procedure as described in Refs. [160,161], which results in the following equations:

$$p_{r_*} = \frac{\xi}{2(1 + B_{np}^{\text{align}})} \left[\mathcal{F}_{\phi} \left(\frac{dp_{\phi}}{dr} \right)^{-1} \frac{2H_{\text{EOB}}H_{\text{even}}}{MA^{\text{align}}} - \xi \frac{\partial Q^{\text{align}}}{\partial p_{r_*}} \right], \tag{19}$$

$$\begin{split} K_0 p_{\phi}^2 + 2H_{\text{even}} \frac{\partial \bar{H}_{\text{odd}}}{\partial r} p_{\phi} + K_1 \\ + \frac{2H_{\text{even}} H_{\text{EOB}}}{M \xi} \left(\frac{dp_{r_*}}{dr} \frac{dr}{dt} - \frac{p_{r_*}}{p_{\phi}} \mathcal{F}_{\phi} \right) = 0. \end{split} \tag{20}$$

Here, the only unknowns are the explicit p_{r_*} in the left-hand side of the first equation, and the explicit p_ϕ^2 and p_ϕ in the second; all the other instances of p_{r_*} and p_ϕ are obtained from previous orders. We employ the PA approximation at eighth order.

IV. THE SEOBNRV5 MULTIPOLAR WAVEFORM

In this section, we describe the building blocks used in the construction of the multipolar spinning, nonprecessing waveform modes $h_{\ell m}$ of the SEOBNRv5HM model. We closely follow the construction of the SEOBNRv4HM model [78] and highlight differences when needed.

In general, the complex linear combination of GW polarizations, $h(t) \equiv h_+(t) - ih_\times(t)$, can be expanded in the basis of -2 spin-weighted spherical harmonics [61] as follows:

$$h(t; \lambda, \iota, \varphi_0) = \sum_{\ell \ge 2} \sum_{|m| \le \ell} {}_{-2} Y_{\ell m}(\iota, \varphi_0) h_{\ell m}(t; \lambda), \qquad (21)$$

where λ denotes the intrinsic parameters of the compact binary source, such as masses $(m_{1,2})$ and spins $(\chi_{1,2})$. The waveform modes $h_{\ell m}$ depend on only three parameters (q,χ_1,χ_2) , since the waveform scales trivially with the total mass M. The parameters (ι,φ_0) describe the binary's inclination angle (computed with respect to the direction perpendicular to the orbital plane) and the azimuthal direction to the observer, respectively.²

In the EOB framework, the GW modes defined in Eq. (21) are decomposed into inspiral-plunge and merger-ringdown modes. In SEOBNRv5HM, we model the (2,2)

and the largest subdominant modes [78]: (3,3), (2,1), (4,4), (3,2), (5,5), and (4,3). For aligned-spin binaries $h_{\ell m} = (-1)^{\ell} h_{\ell - m}^*$, therefore we restrict the discussion to (ℓ, m) modes with m > 0. We have

$$h_{\ell m}(t) = \begin{cases} h_{\ell m}^{\text{insp-plunge}}(t), & t < t_{\text{match}}^{\ell m} \\ h_{\ell m}^{\text{merger-RD}}(t), & t > t_{\text{match}}^{\ell m} \end{cases}, \tag{22}$$

where we define $t_{\text{match}}^{\ell m}$ as

$$t_{\text{match}}^{\ell m} = \begin{cases} t_{\text{peak}}^{22}, & (\ell, m) = (2, 2), (3, 3), (2, 1), \\ & (4, 4), (3, 2), (4, 3) \\ t_{\text{peak}}^{22} - 10M, & (\ell, m) = (5, 5), \end{cases}$$
(23)

where t_{peak}^{22} is the peak of the (2,2)-mode amplitude. The choice of a different attachment point for the (5,5) mode is motivated, as in Ref. [78], by the fact that at late times the error in some of the NR waveforms used to calibrate the model is too large to accurately extract the quantities that are needed to build the full inspiral-merger-ringdown waveforms (see below). For the same reason, since typically $t_{\text{peak}}^{\ell m} - t_{\text{peak}}^{22} > 0$ [61,142], we emphasize that the merger-ringdown attachment for all other modes is done at the peak of the (2,2) mode, rather than at each mode's peak time as in other EOB models [61,113].

A. Inspiral-plunge $h_{\ell m}$ modes

The inspiral-plunge EOB waveform modes can be written as

$$h_{\ell m}^{\text{insp-plunge}} = h_{\ell m}^{\text{F}} N_{\ell m}, \tag{24}$$

where $h_{\ell m}^{\rm F}$ is a factorized, resummed form of the PN-expanded GW modes for aligned spins in circular orbits [59,148,159], while $N_{\ell m}$ is the nonquasicircular (NQC) correction, aimed at incorporating relevant radial effects during the plunge, toward the merger.

The factorized inspiral modes are written as

$$h_{\ell m}^{\rm F} = h_{\ell m}^{\rm N} \hat{S}_{\rm eff} T_{\ell m} f_{\ell m} e^{i\delta_{\ell m}}. \tag{25}$$

The first factor, $h_{\ell m}^{(N,\epsilon_{\ell m})}$ is the leading (Newtonian) order waveform, and its explicit expression is [59,159]

$$h_{\ell m}^{\rm N} = \frac{\nu M}{d_L} n_{\ell m} c_{\ell + \epsilon_{\ell m}}(\nu) v_{\phi}^{\ell + \epsilon_{\ell m}} Y_{\ell - \epsilon_{\ell m}, -m} \left(\frac{\pi}{2}, \phi\right). \tag{26}$$

Here d_L is the luminosity distance of the binary to the observer, $Y_{\ell m}$ is the scalar spherical harmonic, $\epsilon_{\ell m}$ is the parity of the mode, such that

²In general, the GW polarizations emitted by a quasicircular BBH depend on its masses and spins $\lambda = \{m_1, m_2, \chi_{1,2}\}$, the angles (ι, φ_0) , the luminosity distance of the binary to the observer d_L , and the time of arrival t_c . Inserting back units, the modes scale as $\sim GM/(c^2d_L)$.

$$\epsilon_{\ell m} = \begin{cases} 0, & \ell + m \text{ is even} \\ 1, & \ell + m \text{ is odd} \end{cases}, \tag{27}$$

and the functions $n_{\ell m}$ and $c_k(\nu)$ are given by

$$n_{\ell m} = \begin{cases} \frac{8\pi(im)^{\ell}}{(2\ell+1)!!} \sqrt{\frac{(\ell+1)(\ell+2)}{\ell(\ell-1)}}, & \ell+m \text{ is even} \\ \frac{-16i\pi(im)^{\ell}}{(2\ell+1)!!} \sqrt{\frac{(2\ell+1)(\ell+2)(\ell^2-m^2)}{(2\ell-1)(\ell+1)\ell(\ell-1)}}, & \ell+m \text{ is odd}, \end{cases}$$
(28)

and

$$c_k(\nu) = \left(\frac{1 - \sqrt{1 - 4\nu}}{2}\right)^{k - 1} + (-1)^k \left(\frac{1 + \sqrt{1 - 4\nu}}{2}\right)^{k - 1}.$$
(29)

Finally, v_{ϕ} in Eq. (26) is given by

$$v_{\phi} = M\Omega r_{\Omega},\tag{30}$$

where Ω is the orbital frequency and

$$r_{\Omega} = \left. \left(\frac{\partial H_{\text{EOB}}}{\partial p_{\phi}} \right)^{-2/3} \right|_{p_{\sigma} = 0}. \tag{31}$$

The (dimensionless) effective source term $\hat{S}_{\rm eff}$ is given by either the effective energy $E_{\rm eff}$ or the orbital angular momentum p_{ϕ} , both expressed as functions of $v_{\Omega} \equiv (M\Omega)^{1/3}$, such that

$$\hat{S}_{\text{eff}} = \begin{cases} \frac{E_{\text{eff}}(v_{\Omega})}{\mu}, & \ell + m \text{ even,} \\ v_{\Omega} \frac{p_{\phi}(v_{\Omega})}{M\mu}, & \ell + m \text{ odd,} \end{cases}$$
(32)

where $E_{\rm eff}$ is related to the total energy E via the EOB energy map $E = M\sqrt{1 + 2\nu(E_{\rm eff}/\mu - 1)}$.

The factor $T_{\ell m}$ in Eq. (25) resums an infinite number of leading logarithms entering the tail contributions [162], and is given by

$$T_{\ell m} = \frac{\Gamma(\ell + 1 - 2i\hat{k})}{\Gamma(\ell + 1)} e^{\pi\hat{k}} e^{2i\hat{k}\ln(2m\Omega r_0)}, \qquad (33)$$

where $\Gamma(...)$ is the Euler gamma function, $\hat{k} \equiv m\Omega E$, and the constant r_0 takes the value $2M/\sqrt{e}$ to give agreement with waveforms computed in the test-body limit [159].

The remaining part of the factorized modes (25) is expressed as an amplitude $f_{\ell m}$ and a phase $\delta_{\ell m}$, which are computed such that the expansion of $h_{\ell m}^{\rm F}$ agrees with the PN-expanded modes. For nonspinning binaries, $f_{\ell m}$ is further resummed as [59] $f_{\ell m} = (\rho_{\ell m})^{\ell}$ to reduce the magnitude of the 1PN coefficient, which grows linearly with ℓ . Following Refs. [75,76,159], for spinning binaries

we separate the nonspinning and spin contributions for the odd m modes, such that

$$f_{\ell m} = \begin{cases} \rho_{\ell m}^{\ell}, & m \text{ even,} \\ (\rho_{\ell m}^{\text{NS}})^{\ell} + f_{\ell m}^{\text{S}}, & m \text{ odd,} \end{cases}$$
(34)

where $\rho_{\ell m}^{\rm NS}$ is the nonspinning part of $\rho_{\ell m}$, while $f_{\ell m}^{\rm S}$ is the spin part of $f_{\ell m}$.

The explicit expressions for $\rho_{\ell m}$, $f_{\ell m}$ and $\delta_{\ell m}$ that are used in the SEOBNRv5HM model are provided in Appendix B, and are mostly similar to those in SEOBNRv4HM as derived in Refs. [75,77,78,159]. The main differences are as follows:

- (1) We correct the $\mathcal{O}(v^5\delta\chi_A\nu)$ coefficient in ρ_{22} , whose value is 19/42, but was mistakenly replaced in the SEOBNRv4 code by 196/42.
- (2) We add in ρ_{22} the next-to-leading order (NLO) spin-squared contribution at 3PN and the LO spin-cubed part at 3.5PN, which are given by Eq. (4.11a) of Ref. [127].
- (3) We add all the known spin terms in the (3,2) and (4,3) amplitudes [Eqs. (B2a) and (B5b) from Ref. [127]].
- (4) We correct the expressions for the (2,1) mode. As pointed out in Ref. [127], the $\mathcal{O}(v^6\chi^2v^2)$ terms in the (2,1) mode in the SEOBNRv4HM model [78] are not correct, as well as the $\mathcal{O}(vv^5)$ nonspinning part of δ_{21} , whose coefficient had the value -493/42 [59,61] instead of -25/2, due to an error in the (2,1) mode in Ref. [163], which was later corrected in an erratum.
- (5) We consistently include the high-order PN terms from Appendix A of Ref. [78] in the RR force, and not just in the waveform modes.

The new terms we add in the modes were derived in Ref. [127], which was made public when the model was close to being finalized; hence, we only added the terms we considered most important, and we will add in a future update of the model all the 3.5PN contributions to the waveform modes, as derived in Refs. [127,164]. We remark that adding additional PN information in the waveform modes (except for the phases) modifies the energy flux (i.e., the RR force), and would require a recalibration of the EOB dynamics to NR simulations.

As discussed in the SEOBNRv4HM model of Ref. [78], the presence of minima, close to merger, in the amplitude of some modes, leads to the introduction of additional calibration parameters before applying the NQC corrections. The modes for which this is needed are the (2,1), (5,5), and (4,3). The minima occur for $q \sim 1$ and large $|\chi_A|$, and can lead to unphysical features in the amplitude after applying the NQC corrections if they occur close to the attachment point $t \sim t_{\rm match}$. For the (2,1) mode, this behavior is also found in NR simulations, while for the (5,5) and (4,3) we do not observe it in the NR waveforms at our disposal, and is likely an artifact of the PN-expanded modes [78].

Calibration terms in the modes take the form $c_{\ell m} v_{\Omega}^{\beta_{\ell m}}$, and are added in $f_{\ell m}$, with $\beta_{\ell m}$ being the lowest PN order not already included. The calibration parameter $c_{\ell m}$ is determined by imposing the following condition:

$$|h_{\ell m}^{F}(t_{\text{match}}^{\ell m})| \equiv |h_{\ell m}^{N} \hat{S}_{\text{eff}} T_{\ell m} e^{i\delta_{\ell m}} f_{\ell m} (c_{\ell m})|_{t=t_{\text{match}}^{\ell m}},$$

$$= |h_{\ell m}^{NR}(t_{\text{match}}^{\ell m})|,$$
for $(\ell, m) = (2, 1), (5, 5), (4, 3),$ (35)

where $|h_{\ell m}^{\rm NR}(t_{\rm match}^{\ell m})|$ is the amplitude of the NR modes at the matching point, given by fits in parameter space in Appendix C.

The remaining $N_{\ell m}$ factor in the inspiral-plunge modes (24) is the NQC correction and reads as

$$N_{\ell m} = \left[1 + \frac{\hat{p}_{r_*}^2}{(r\Omega)^2} \left(a_1^{h_{\ell m}} + \frac{a_2^{h_{\ell m}}}{\hat{r}} + \frac{a_3^{h_{\ell m}}}{\hat{r}^{3/2}} \right) \right] \times \exp \left[i \left(b_1^{h_{\ell m}} \frac{\hat{p}_{r_*}}{r\Omega} + b_2^{h_{\ell m}} \frac{\hat{p}_{r_*}^3}{r\Omega} \right) \right], \tag{36}$$

where $\hat{r} \equiv r/M$ and $\hat{p}_{r_*} \equiv p_{r_*}/\mu$. The use of the NQC corrections guarantees that the modes' amplitude and frequency agree with NR input values (see below), given in Appendix C, at the matching point $t_{\text{match}}^{\ell m}$. In particular, one fixes the five constants $(a_1^{h_{\ell m}}, a_2^{h_{\ell m}}, a_3^{h_{\ell m}}, b_1^{h_{\ell m}}, b_2^{h_{\ell m}})$ by requiring the following [76–78]:

(1) The amplitude of the EOB modes is the same as that of the NR modes at the matching point $t_{\text{match}}^{\ell m}$:

$$|h_{\ell m}^{\text{insp-plunge}}(t_{\text{match}}^{\ell m})| = |h_{\ell m}^{\text{NR}}(t_{\text{match}}^{\ell m})|. \tag{37}$$

We note that this condition is different from that in Eq. (35) because it affects $h_{\ell m}^{\text{insp-plunge}}(t_{\text{match}}^{\ell m})$ and not $h_{\ell m}^{\text{F}}(t_{\text{match}}^{\ell m})$. Because of the calibration parameter in Eq. (35), for the modes (2,1), (5,5), and (4,3), this condition becomes simply $|N_{\ell m}|=1$.

(2) The first derivative of the amplitude of the EOB modes is the same as that of the NR modes at the matching point $t_{\text{match}}^{\ell m}$:

$$\left. \frac{d|h_{\ell m}^{\text{insp-plunge}}(t)|}{dt} \right|_{t=t_{\text{makeh}}^{\ell m}} = \frac{d|h_{\ell m}^{\text{NR}}(t)|}{dt} \bigg|_{t=t_{\text{makeh}}^{\ell m}}. \quad (38)$$

(3) The second derivative of the amplitude of the EOB modes is the same as that of the NR modes at the matching point $t_{\text{match}}^{\ell m}$:

$$\left. \frac{d^2 |h_{\ell m}^{\text{insp-plunge}}(t)|}{dt^2} \right|_{t=t_{\text{match}}^{\ell m}} = \left. \frac{d^2 |h_{\ell m}^{\text{NR}}(t)|}{dt^2} \right|_{t=t_{\text{match}}^{\ell m}}.$$
 (39)

(4) The frequency of the EOB modes is the same as that of the NR modes at the matching point $t_{\text{match}}^{\ell m}$:

$$\omega_{\ell m}^{\mathrm{insp-plunge}}(t_{\mathrm{match}}^{\ell m}) = \omega_{\ell m}^{\mathrm{NR}}(t_{\mathrm{match}}^{\ell m}).$$
 (40)

(5) The first derivative of the frequency of the EOB modes is the same as that of the NR modes at the matching point $t_{\text{match}}^{\ell m}$:

$$\left. \frac{d\omega_{\ell_m}^{\text{insp-plunge}}(t)}{dt} \right|_{t=t_{\text{orbito}}^{\ell_m}} = \left. \frac{d\omega_{\ell_m}^{\text{NR}}(t)}{dt} \right|_{t=t_{\text{orbito}}^{\ell_m}}.$$
 (41)

The rhs of Eqs. (37)–(41) (usually called *input values*), is given as fitting formulas for every point of the parameter space (ν, χ_1, χ_2) in Appendix C. These fits are produced using the NR SXS catalog [130,131], and BH-perturbation-theory waveforms described in Sec. V. We point out that the NQC corrections and the $c_{\ell m}$ calibration coefficients are not included in the SEOBNRv5HM radiation-reaction force.

In the SEOBNRv5 model, the input values are enforced at $t = t_{\text{match}}^{\ell m}$, given in Eq. (23) as a function of t_{peak}^{22} . We take

$$t_{\text{peak}}^{22} = t_{\text{ISCO}} + \Delta t_{\text{ISCO}}^{22},$$
 (42)

where $t_{\rm ISCO}$ is the time at which $r = r_{\rm ISCO}$, with $r_{\rm ISCO}$ the radius of the geodesic ISCO in Kerr spacetime [165] with the same mass and spin as the remnant, computed with NR fitting formulas [166,167], and $\Delta t_{\rm ISCO}^{22}$ is a calibration parameter, to be determined by comparing against NR simulations. In the SEOBNRv4 model, the merger time was given by

$$t_{\text{peak}}^{22} = t_{\text{peak}}^{\Omega} + \Delta t_{\text{peak}}^{22},\tag{43}$$

with $t_{\rm peak}^{\Omega}$ being the peak of the orbital frequency. The purpose of $\Delta t_{\rm peak}^{22}$ is still to introduce a time delay between the peak of the orbital frequency and the peak of the (2,2) mode, as observed in the test-body limit [142,143,168]. However, we find the new definition to be more robust, since it is independent of features in the late dynamics, like the existence of a peak in the orbital frequency, which is not necessarily present for all BBH parameters when the Hamiltonian and modes are not the same as the ones used in the SEOBNRv4 model. More specifically, in the latter the A potential was designed (log resummation) [69,70] in such a way as always to guarantee the presence of the light ring (the peak in the orbital frequency) for aligned-spin binaries. This is no longer the case when the Padé resummation of the A potential is employed, as done in SEOBNRv5 (see below).

Another notable improvement in the SEOBNRv5HM waveforms is the addition of 2GSF calibration coefficients in the nonspinning modes and RR force from Ref. [125]. In that work, one defines

$$\rho_{\ell m} = \rho_{\ell m}^{(0)} + \nu \rho_{\ell m}^{(1)} + \mathcal{O}(\nu^2), \tag{44}$$

and augments the $\rho_{\ell m}^{(1), {\rm EOB}}$ by adding an extra polynomial $\Delta \rho_{\ell m}^{(1)}$ in v_{Ω}^2 starting at the lowest order in v_{Ω}^2 not already included. The $\Delta \rho_{\ell m}^{(1)}$ are determined by fitting to the numerical $\rho_{\ell m}^{(1), {\rm GSF}}$ results, leading to the following expressions:

$$\Delta \rho_{22}^{(1)} = 21.2v_{\Omega}^8 - 411v_{\Omega}^{10},\tag{45a}$$

$$\Delta \rho_{21}^{(1)} = 1.65 v_{\Omega}^6 + 26.5 v_{\Omega}^8 + 80 v_{\Omega}^{10}, \tag{45b}$$

$$\Delta \rho_{33}^{(1)} = 12v_{\Omega}^8 - 215v_{\Omega}^{10},\tag{45c}$$

$$\Delta \rho_{32}^{(1)} = 0.333 v_{\Omega}^6 - 6.5 v_{\Omega}^8 + 98 v_{\Omega}^{10}, \tag{45d}$$

$$\Delta \rho_{44}^{(1)} = -3.56 v_{\Omega}^6 + 15.6 v_{\Omega}^8 - 216 v_{\Omega}^{10}, \qquad (45e)$$

$$\Delta \rho_{43}^{(1)} = -0.654 v_{\Omega}^4 - 3.69 v_{\Omega}^6 + 18.5 v_{\Omega}^8, \tag{45f}$$

$$\Delta \rho_{55}^{(1)} = -2.61 v_{\Omega}^4 + 1.25 v_{\Omega}^6 - 35.7 v_{\Omega}^8. \tag{45g}$$

In the 2GSF calibration, terms $\Delta \rho_{\ell m}^{(1)}$ are then added directly to the full (not ν expanded) $\rho_{\ell m}$ coefficients. In Ref. [125], it is also found beneficial to include additional terms in the (3,2) and (4,3) modes obtained by matching to the PN expansions of the test-mass limit (TML) GW energy flux. Thus, we add the following terms:

$$\begin{split} \Delta \rho_{32}^{(0),\text{TML}} &= \left(-\frac{1312549797426453052}{176264081083715625} \right. \\ &\left. + \frac{18778864}{12629925} \text{eulerlog}(2, v_{\Omega}) \right) v_{\Omega}^{10}, \quad (46\text{a}) \end{split}$$

$$\begin{split} \Delta \rho_{43}^{(0),\text{TML}} &= \left(-\frac{2465107182496333}{460490801971200} \right. \\ &\left. + \frac{174381}{67760} \text{eulerlog}(3, v_{\Omega}) \right) v_{\Omega}^{8}, \end{split} \tag{46b}$$

where we define

$$eulerlog(m, v_{\Omega}) \equiv \gamma_E + \log(2mv_{\Omega}), \tag{47}$$

in which γ_E is the Euler constant.

B. Merger-ringdown $h_{\ell m}$ modes

The merger-ringdown modes are constructed with a phenomenological Ansatz, using information from NR simulations and TML waveforms. The Ansatz we employ for the modes (2,2), (3,3), (2,1), (4,4), (5,5), which show

monotonic amplitude and frequency evolution, is the same as the one implemented in Refs. [77,78] and reads as

$$h_{\ell_m}^{\text{merger-RD}}(t) = \nu \tilde{A}_{\ell_m}(t) e^{i\tilde{\phi}_{\ell_m}(t)} e^{-i\sigma_{\ell_{m0}}(t - t_{\text{match}}^{\ell_m})}, \quad (48)$$

where $\sigma_{\ell m0} = \sigma_{\ell m}^{R} - i \sigma_{\ell m}^{I}$ is the complex frequency of the least-damped quasinormal mode (QNM) of the remnant BH. The QNM frequencies are obtained for each (ℓ, m) mode as a function of the BH's final mass and spin using the QNM Python package [169]. The BH's mass and spin are in turn computed using the fitting formulas of Refs. [166,167], respectively. The Ansätze for the two functions $\tilde{A}_{\ell m}$ and $\tilde{\phi}_{\ell m}$ in Eq. (48) are the following [77,78]:

$$\tilde{A}_{\ell m}(t) = c_{1,c}^{\ell m} \tanh\left[c_{1,f}^{\ell m}(t - t_{\text{match}}^{\ell m}) + c_{2,f}^{\ell m}\right] + c_{2,c}^{\ell m},\tag{49}$$

$$\tilde{\phi}_{\ell m}(t) = \phi_{\text{match}}^{\ell m} - d_{1,c}^{\ell m} \log \left[\frac{1 + d_{2,f}^{\ell m} e^{-d_{1,f}^{\ell m} (t - t_{\text{match}}^{\ell m})}}{1 + d_{2,f}^{\ell m}} \right], \quad (50)$$

where $\phi_{\mathrm{match}}^{\ell m}$ is the phase of the inspiral-plunge mode (ℓ, m) at $t = t_{\mathrm{match}}^{\ell m}$. The coefficients $d_{1,c}^{\ell m}$ and $c_{i,c}^{\ell m}$ (i = 1, 2) are constrained by the requirement that the amplitude and phase of $h_{\ell m}(t)$ in Eq. (22) are continuously differentiable at $t = t_{\mathrm{match}}^{\ell m}$, and can be written in terms of $c_{1,f}^{\ell m}$, $c_{2,f}^{\ell m}$, $\sigma_{\ell m}^{\mathrm{R}}$, $|h_{\ell m}^{\mathrm{insp-plunge}}(t_{\mathrm{match}}^{\ell m})|$, $\partial_t |h_{\ell m}^{\mathrm{insp-plunge}}(t_{\mathrm{match}}^{\ell m})|$, as follows:

$$c_{1,c}^{\ell m} = \frac{1}{c_{1,f}^{\ell m}} \left[\partial_t \middle| h_{\ell m}^{\text{insp-plunge}}(t_{\text{match}}^{\ell m}) \middle| -\sigma_{\ell m}^{\text{R}} \middle| h_{\ell m}^{\text{insp-plunge}}(t_{\text{match}}^{\ell m}) \middle| \right] \cosh^2(c_{2,f}^{\ell m}), \tag{51}$$

$$c_{2,c}^{\ell m} = \frac{\left|h_{\ell m}^{\text{insp-plunge}}(t_{\text{match}}^{\ell m})\right|}{\nu} - \frac{1}{c_{1,f}^{\ell m}\nu} \left[\partial_{t} |h_{\ell m}^{\text{insp-plunge}}(t_{\text{match}}^{\ell m})\right| - \sigma_{\ell m}^{R} \left|h_{\ell m}^{\text{insp-plunge}}(t_{\text{match}}^{\ell m})\right| \left] \cosh(c_{2,f}^{\ell m}) \sinh(c_{2,f}^{\ell m}), \quad (52)$$

or in terms of $d_{1,f}^{\ell m}, d_{2,f}^{\ell m}, \sigma_{\ell m}^{\text{I}}, \omega_{\ell m}^{\text{insp-plunge}}(t_{\text{match}}^{\ell m})$ for $d_{1,c}^{\ell m}$

$$d_{1,c}^{\ell m} = \left[\omega_{\ell m}^{\text{insp-plunge}}(t_{\text{match}}^{\ell m}) - \sigma_{\ell m}^{\text{I}}\right] \frac{1 + d_{2,f}^{\ell m}}{d_{1,f}^{\ell m} d_{2,f}^{\ell m}}.$$
 (53)

The remaining parameters in Eqs. (49) and (50) are the free coefficients $c_{i,f}^{\ell m}$ and $d_{i,f}^{\ell m}$, i=1, 2.

The NQC corrections ensure that the waveform's amplitude and frequency coincide with the NR input values at $t=t_{\rm match}^{\ell m}$, and make the merger-ringdown modes independent of the EOB inspiral modes, allowing for an independent calibration of the two. To obtain $c_{i,f}^{\ell m}$ and $d_{i,f}^{\ell m}$, we first extract them from each NR and TML waveform by least-square fits, and then interpolate the values obtained across the parameter space using polynomial fits in ν and χ . While

in Ref. [78] the same polynomial was used for most of the free coefficients, in this work we use a recursive-featureelimination (RFE) [170] algorithm with polynomial features of third and fourth order, depending on the quantity to fit. Applying a log transformation to some of the coefficients is also beneficial, both to improve the quality of the fits and to ensure the positivity of those quantities when extrapolating outside of the region where NR data are available. Finally, we apply a similar RFE strategy to most of the fits for the input values, the only exceptions being the fits of the amplitude of the odd-m modes and their derivatives. The odd-m modes vanish in the equal-mass and equal-spin limit, since they need to satisfy the symmetry under rotation $\varphi_0 \to \varphi_0 + \pi$; therefore, the corresponding amplitudes are better captured by ad hoc nonlinear Ansätze that enforce this limit by construction (see also Appendix D).

C. Mode mixing in the (3,2) and (4,3) merger-ringdown $h_{\ell m}$ modes

The merger-ringdown (3,2) and (4,3) modes show post-merger oscillations [56,171], mostly related to the mismatch between the *spherical* harmonic basis used for extraction in NR simulations, and the *spheroidal* harmonics adapted to the perturbation theory of Kerr BHs. Because of this, it is not possible to use the same Ansatz of Eqs. (48)–(50) straightforwardly.

Equation (21) can be formulated in terms of -2 spin-weighted *spheroidal* harmonics as

$$h(t; \lambda, \iota, \varphi_0) = \sum_{\ell' > 2} \sum_{|m| \le \ell'} \sum_{n \ge 0} {}_{-2} S_{\ell'mn}(\iota, \varphi_0)^S h_{\ell mn}(t, \lambda), \quad (54)$$

where $S_{\ell mn} \equiv S_{\ell m}(a_f \sigma_{\ell mn})$ are the -2 spin-weighted spheroidal harmonics associated with the QNM frequencies $\sigma_{\ell mn}$, and with $a_f M_f$ being the spin angular momentum of the final BH of mass M_f [172]. The superscript S denotes that the ${}^S h_{\ell mn}$ modes are expanded in the spheroidal harmonics basis.

One can switch from the spherical harmonic basis to the spheroidal harmonic basis via

$${}_{-2}S_{\ell'mn} = \sum_{\ell > |m|} \mu_{m\ell\ell'n-2}^* Y_{\ell m}, \tag{55}$$

where $\mu_{m\ell\ell'n}$ are mode-mixing coefficients, which we compute using fits provided in Ref. [173] (more complex fits can be found in Ref. [174]), and the star denotes the usual complex conjugation. Inserting Eq. (55) in Eq. (54) for the spheroidal harmonics we get

$$h(t;\iota,\varphi_0) = \sum_{\ell' \geq 2} \sum_{|m| \leq \ell'} \sum_{n \geq 0} \sum_{\ell \geq |m|} {}_{-2} Y_{\ell m}(\iota,\varphi_0)^S h_{\ell m n}(t) \mu_{m\ell\ell' n}^*,$$

where we have suppressed the λ parameter from the expression to ease the notation. Comparing Eq. (56) with Eq. (21), we obtain the following relation between spherical and spheroidal modes,

$$h_{\ell m}(t) = \sum_{\ell' \ge |m|} \sum_{n \ge 0} {}^{S} h_{\ell' m n}(t) \mu_{m \ell \ell' n}^{*}. \tag{57}$$

Starting from Eq. (57), we can model the mode-mixing behavior [48,175] to obtain monotonic functions that can be fitted by the Ansatz already used for the other modes. Practically, it is not feasible to sum over all the spheroidal modes to get each spherical mode, so we make a few reasonable approximations. First, we neglect the overtone (n > 0) contributions in the right-hand side of Eq. (57), because their decay times are $\gtrsim 3$ times smaller than the dominant overtone n = 0. Second, for a given (ℓ, m) mode, we neglect the contributions from the spheroidal modes with $\ell' > \ell$ since their amplitudes are subdominant compared to the $(\ell, m, 0)$ mode. With these approximations, we can rewrite Eq. (57) as

$$h_{\ell m}(t) \simeq \sum_{\ell' \le \ell} {}^{S} h_{\ell' m \, 0}(t) \mu_{m\ell\ell' 0}^{*}.$$
 (58)

Writing it explicitly for the modes of interest,

$$h_{22}(t) \simeq \mu_{2220}^* {}^{S} h_{220}(t),$$
 (59a)

$$h_{33}(t) \simeq \mu_{3330}^* h_{330}(t),$$
 (59b)

$$h_{32}(t) \simeq \mu_{2320}^* {}^{S}h_{220}(t) + \mu_{2330}^* {}^{S}h_{320}(t),$$
 (59c)

$$h_{43}(t) \simeq \mu_{3430}^* {}^{S}h_{330}(t) + \mu_{3440}^* {}^{S}h_{430}(t).$$
 (59d)

From these equations, we can solve for the ${}^S\!h_{\ell m0}$ modes to obtain

$${}^{S}h_{320}(t) \simeq \frac{h_{32}(t)\mu_{2220}^* - h_{22}(t)\mu_{2320}^*}{\mu_{2330}^*\mu_{2220}^*},$$
 (60a)

$${}^{S}h_{430}(t) \simeq \frac{h_{43}(t)\mu_{3440}^* - h_{33}(t)\mu_{3430}^*}{\mu_{3330}^*\mu_{3440}^*}.$$
 (60b)

We show in Fig. 1 the characteristics of the ${}^Sh_{\ell m0}$ mode obtained from the spherical mode $h_{\ell m}$ via Eqs. (60a) and (60b) for the NR waveform SXS:BBH:2138. The h_{32} mode shows oscillations in its amplitude and frequency, while the ${}^Sh_{320}$ mode obtained from Eq. (60a) has a nearly monotonic behavior. Most importantly, the frequency of the ${}^Sh_{320}$ mode oscillates around the QNM frequency predicted in BH perturbation theory for the spheroidal (3,2,0) mode.

Thus, we model the spheroidal ${}^Sh_{lm0}$ modes using the Ansatz of Eq. (48), where in Eq. (50) $\phi_{\ell m}^{\rm match}$ is replaced by ${}^S\phi_{\ell m0}^{\rm match}$, which is the phase of ${}^Sh_{lm0}$ at $t=t_{\ell m}^{\rm match}$. In Eqs. (51)

(56)

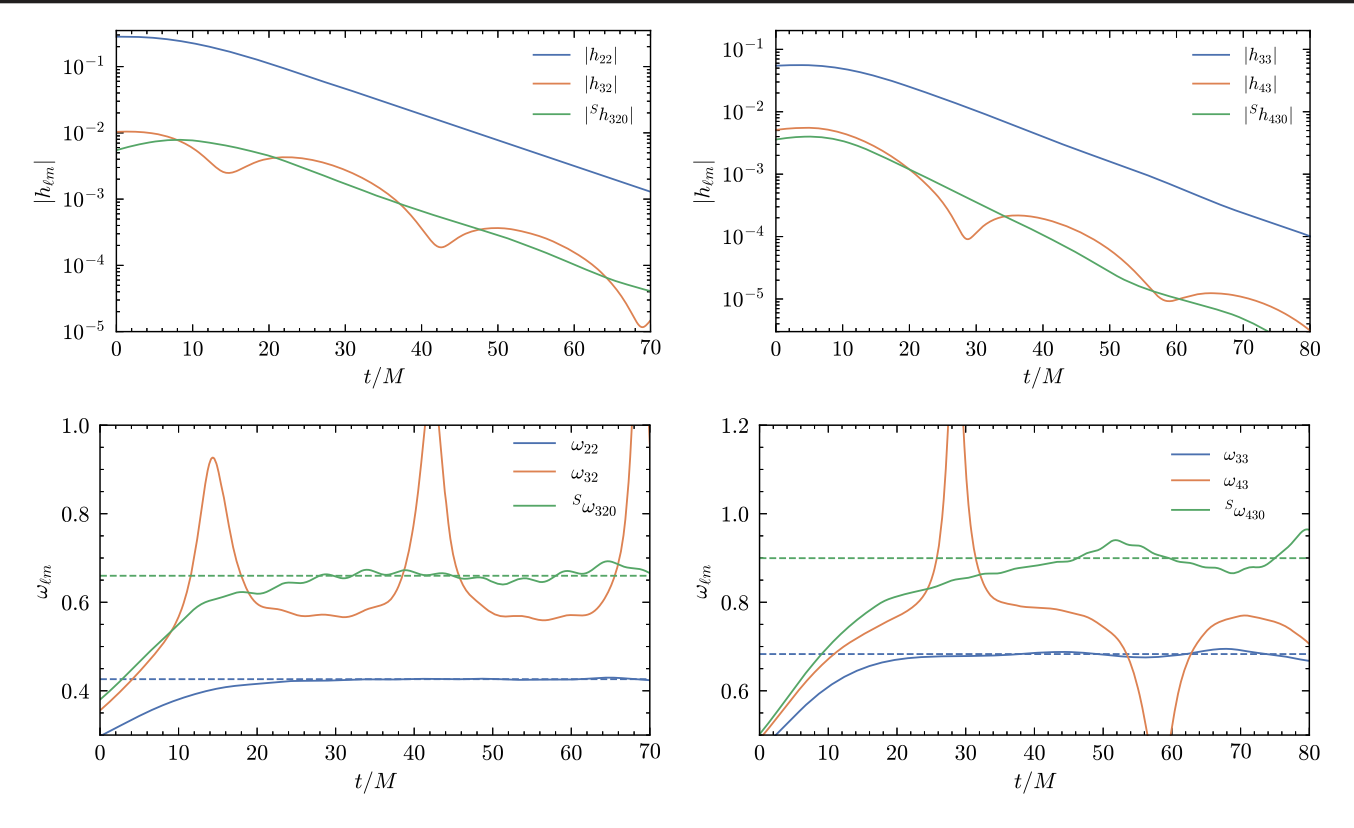


FIG. 1. Mode mixing in the NR simulation SXS: BBH: 2138 ($q = 3.0, \chi_1 = -0.6, \chi_2 = 0.4$). Upper panel: amplitude of the modes $|h_{\ell m}|$ and of $|{}^Sh_{\ell m0}|$, after the mode-mixing removal [Eqs. (60a) and (60b)]. We denote with t = 0 the time of the peak of the (2,2)-mode amplitude. Lower panel: frequencies of the modes $h_{\ell m}$ and of ${}^Sh_{\ell m0}$. The ringdown frequencies of the ${}^Sh_{320}$ and ${}^Sh_{430}$ modes are well approximated by the (3,2,0) and (4,3,0) QNM frequencies (dashed horizontal lines) after the mode-mixing removal.

and (52) we replace $h_{\ell m}$ by ${}^Sh_{lm0}$, and in Eq. (53) we replace $\omega_{\ell m}$ by ${}^S\omega_{\ell m0}$. Once we have a model for ${}^Sh_{320}$ and ${}^Sh_{430}$, it is straightforward to obtain the (3,2) and (4,3) modes by combining them with the (2,2) and (3,3) ones previously obtained by inverting Eqs. (60a) and (60b).

The NQC corrections for the inspiral-plunge $h_{\ell m}$ modes require the values for the spherical NR modes $h_{\ell m}^{\rm NR}(t_{\ell m}^{\rm match})$, and those are the quantities that we fit and interpolate across the parameter space. However, we need the input values for ${}^Sh_{lm0}^{\rm match} \equiv {}^Sh_{lm0}(t_{\ell m}^{\rm match})$ and its derivative in order to fix the coefficients $c_{i,c}^{\ell m}$ and $d_{i,c}^{\ell m}$. They can be derived from Eqs. (60a) and (60b) starting from the $h_{\ell m}$ input values.

First, we introduce the following quantities:

$$\rho = |\mu_{m\ell\ell'0}| \frac{|h_{\ell'm}^{\text{match}}|}{|\mu_{m\ell'\ell'0}||h_{\ell'm}^{\text{match}}|}, \tag{61a}$$

$$\delta \phi = \phi_{\text{match}}^{\ell'm} - \phi_{\text{match}}^{\ell m} - \arg(\mu_{m\ell\ell'0}) + \arg(\mu_{m\ell'\ell'0}), \quad (61b)$$

$$F = \sqrt{(1 - \rho \cos(\delta \phi))^2 + \rho^2 \sin^2(\delta \phi)}, \tag{61c}$$

$$\dot{\rho} = |\mu_{m\ell\ell'0}| \left(\frac{\partial_t |h_{\ell'm}^{\text{match}}|}{|h_{\ell m}^{\text{match}}|} - \frac{|h_{\ell'm}^{\text{match}}|}{|h_{\ell m}^{\text{match}}|^2} \partial_t |h_{\ell m}^{\text{match}}| \right), \quad (61d)$$

$$\delta \dot{\phi} = \partial_t \phi_{\text{match}}^{\ell' m} - \partial_t \phi_{\text{match}}^{\ell m}, \tag{61e}$$

$$\dot{F} = \frac{(\rho \dot{\rho} + \rho \sin(\delta \phi) \delta \dot{\phi} - \dot{\rho} \cos(\delta \phi))}{F},$$
(61f)

where $|h_{\ell m}^{\rm match}| \equiv |h_{\ell m}^{\rm insp-plunge}(t_{\rm match}^{\ell m})|$. Then,

$$|{}^{S}h_{\ell m 0}^{\mathrm{match}}| = \frac{|h_{\ell m}^{\mathrm{match}}|F}{|\mu_{m\ell\ell 0}|},\tag{62a}$$

$${}^{S}\phi_{\text{match}}^{\ell m0} = \phi_{\text{match}}^{\ell m} + \arg(\mu_{m\ell\ell 0}) + \arctan\left(\frac{-\rho\sin(\delta\phi)}{1 - \rho\cos(\delta\phi)}\right), \tag{62b}$$

$$\partial_t |^S h_{\ell m 0}^{\text{match}}| = \frac{(\partial_t |h_{\ell m}^{\text{match}}| F + |h_{\ell m}^{\text{match}}| \dot{F})}{|\mu_{m \ell \ell 0}|}, \tag{62c}$$

$${}^{S}\omega_{\ell m0}^{\text{match}} = \omega_{\ell m}^{\text{match}} + \frac{(\rho^{2}\delta\dot{\phi} - \rho\cos(\delta\phi)\delta\dot{\phi} - \dot{\rho}\sin(\phi))}{E^{2}}, \quad (62d)$$

where for the (3,2) mode $m=2, \ell=3, \ell'=2$, and for the (4,3) mode $m=3, \ell=4, \ell'=3$.

V. CALIBRATION TO NUMERICAL-RELATIVITY WAVEFORMS

The inspiral-plunge modes described in Sec. VI are functions of the binary parameters (q,χ_1,χ_2) , the initial orbital frequency Ω_0 at which the evolution is started, and a set of calibration parameters, which are determined as a function of (q,χ_1,χ_2) such that we maximize the agreement between the waveform model and NR simulations of BBHs. In the SEOBNRv5 model we employ the following calibration parameters:

- (1) a_6 : a 5PN, linear in ν , parameter that enters the nonspinning $A_{\text{noS}}(u)$ potential of Eq. (9).
- (2) d_{SO} : a 4.5PN spin-orbit parameter, that enters the odd-in-spin part of the effective Hamiltonian [see Eqs. (12) and (13)].
- Eqs. (12) and (13)].

 (3) $\Delta t_{\rm ISCO}^{22}$: a parameter that determines the time shift between the Kerr ISCO, computed from the final mass and spin of the remnant [166,167], and the peak of the (2,2)-mode amplitude, as given by Eq. (42). We remark that this quantity is different from $\Delta t_{\rm peak}^{22}$ used in the SEOBNRv4 model, where it corresponded to the time difference between the peak of the orbital frequency (light ring) and the peak of the (2,2)-mode amplitude.

The resummation of the analytical information that enters the EOB potentials is critical in determining the model's flexibility to reduce differences with NR waveforms. In the SEOBNRv5 model we perform a (1,5) Padé resummation of the Taylor-expanded potential $A_{\rm noS}^{\rm Tay}(u)$, given by Eq. (9), while treating $\ln u$ as a constant, i.e., we use

$$A_{\text{noS}}(u) = P_5^1[A_{\text{noS}}^{\text{Tay}}(u)].$$
 (63)

The Padé resummation of $A_{\rm noS}$ was originally introduced in Ref. [53] to guarantee the presence of an ISCO in the EOB dynamics at 3PN order for any mass ratio. It was then adopted in nonspinning and initial spinning EOBNR models (e.g., see Refs. [57,61,67]), and in all TEOBResumS models (e.g., see Refs. [58,66,83,85,113]). For $\bar{D}_{\rm noS}(u)$ we perform a (2,3) Padé resummation of the 5PN Talyor-expanded $\bar{D}_{\rm noS}^{\rm Tay}(u)$ given by Eq. (A1) in Appendix A, such that

$$\bar{D}_{\text{noS}}(u) = P_3^2 [\bar{D}_{\text{noS}}^{\text{Tay}}(u)].$$
 (64)

This resummation of $\bar{D}_{\rm noS}(u)$ was recently explored in Ref. [176], although combined with different choices for $A_{\rm noS}(u)$ and $Q_{\rm noS}(u)$ than the ones used in SEOBNRv5. TEOBResumS includes information through 3PN order in $\bar{D}_{\rm noS}(u)$, which is Taylor expanded $[D_{\rm noS}(u) \equiv 1/\bar{D}_{\rm noS}(u)$ is inverse-Taylor resummed] [113,114].

The SEOBNRv4 model adopted a log resummation for these potentials, which was designed to guarantee the presence of a light ring (a peak in the orbital frequency) for aligned-spin binaries. The light ring was needed to determine the point at which to attach the merger-ring-down waveforms, based on $\Delta t_{\rm peak}^{22}$. The use of $\Delta t_{\rm ISCO}^{22}$ as reference for the attachment of the merger ringdown in the SEOBNRv5 model eliminates the dependence on the existence of a peak in the orbital frequency. This enables us to use resummed potentials that may not necessarily exhibit a light ring, but lead to a better agreement with NR simulations compared to the log-resummed ones in SEOBNRv4.³

Similarly, the different resummation of the generic-spin Hamiltonian in SEOBNRv5, based on that of a test mass in a deformed Kerr background [54,73,74,126], instead of on the one of a test spin [70,146,147] as in SEOBNRv4, is a crucial factor in achieving high faithfulness compared to NR simulations. Notably, this change allows us to reach higher accuracy with just one spin-dependent calibration parameter in the Hamiltonian ($d_{\rm SO}$), surpassing what could be obtained by tuning three such parameters in SEOBNRv4.

We calibrate SEOBNRv5HM to 442 NR waveforms, all produced with the SpEC code of the SXS Collaboration [21,22,24,25,30,77,130–140], except for a simulation with mass ratio and dimensionless spins $q=8,\chi_1=0.85,\chi_2=0.85$ produced with the Einstein Toolkit code [78,141]. We also incorporate information from 13 waveforms computed by solving the Teukolsky equation in the framework of BH perturbation theory [142,143], with mass ratio $q=10^3$ and dimensionless spin values in the range $-0.99 \le \chi \le 0.99$.

In Fig. 2 we show the coverage of NR and BH-perturbation-theory waveforms projected on the binary's parameters ν and $\chi_{\rm eff} = (\chi_1 m_1 + \chi_2 m_2)/M$, separated in different regions. In the first region $1 \le q \le 3$ there is a large number of configurations with both BHs carrying spin. The spins' magnitude reach $\chi_{1,2} = 0.998$ in the equal-mass limit, while they are limited to $\chi_{1,2} = 0.85$ for q = 3. The NR coverage in this region is mostly comparable to SEOBNRv4HM. The second region is $3 < q \le 10$. This region includes a significant number of configurations, with primary spins $-0.9 \le \chi_1 \le 0.85$, and is much more densely populated than for SEOBNRv4HM. The third region is $10 < q \le 20$, and it includes simulations with spins only on the heavier BH, with spin magnitudes only up to

³An updated NR calibration of the SEOBNRv4 nonspinning Hamiltonian, using the SEOBNRv5 RR force and gravitational modes, is presented in Appendix A of Ref. [125], confirming that the improvements observed can be predominantly attributed to the updated Hamiltonian.

⁴The full list of simulations is provided as an ancillary file in https://arxiv.org/src/2303.18039v1/anc/NR_simulations.json. For each simulation we list the mass-ratio q, the dimensionless spins $\chi_{1,2}$, the initial orbital frequency Ω_0 , the initial eccentricity e_0 , and the number of orbits $N_{\rm orb}$ up to the merger.

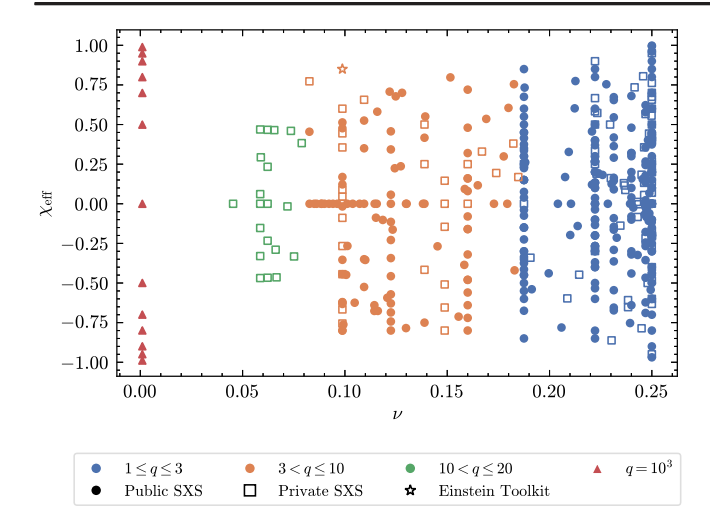


FIG. 2. NR and BH-perturbation-theory waveforms used to calibrate SEOBNRv5HM, projected on the binary's parameters ν and $\chi_{\rm eff} = (\chi_1 m_1 + \chi_2 m_2)/M$. We highlight four regions as explained in the text, and use different markers to distinguish between 327 simulations from the public SXS catalog [131], 114 private SXS waveforms, one Einstein Toolkit simulation, and 13 Teukolsky-code waveforms. We refer to private waveforms as all those which cannot be downloaded from the SXS website [130] at the time of this publication.

 $\chi_1 = 0.5$, or nonspinning waveforms. SEOBNRv4HM was not calibrated to any NR simulation in this region. Finally, the fourth region covers the 13 Teukolsky-code waveforms, with $q = 10^3$ and dimensionless spin values in the range $-0.99 \le \chi \le 0.99$.

The rest of this section explains how we determine the calibration parameters by comparing the SEOBNRv5 waveform model to NR waveforms. We closely follow the procedure adopted in Ref. [77] and highlight differences when needed.

A. Calibration requirements

In order to calibrate the waveform model to NR we first need to establish when two waveforms are close to each other. Given two waveforms $h_1(t)$ and $h_2(t)$, we introduce the match, which is defined as the noise-weighted inner product [177,178]

$$(h_1|h_2) \equiv 4\text{Re} \int_{f_1}^{f_h} \frac{\tilde{h}_1(f)\tilde{h}_2^*(f)}{S_n(f)} df,$$
 (65)

where $\tilde{h}_1(f)$ and $\tilde{h}_2(f)$ indicate Fourier transforms, and $S_n(f)$ is the one-sided power spectral density of the detector noise, which we assume to be the design zero-detuned high-power noise power spectral density (PSD) of Advanced LIGO [179]. The faithfulness is then defined as the overlap between the normalized waveforms, maximized over the relative time and phase shift, that is,

$$\langle h_1 | h_2 \rangle = \max_{\phi_c, t_c} \frac{(h_1(\phi_c, t_c) | h_2)}{\sqrt{(h_1 | h_1)(h_2 | h_2)}}.$$
 (66)

In Eq. (65), we fix $f_h = 2048$ Hz and choose f_l to be $f_l = 1.35 f_{\rm start}$, where we identify the start of the NR simulation $f_{\rm start}$ as the peak of the NR waveform in the frequency domain. The choice of a buffer factor of 1.35 is needed to exclude features caused by the Fourier transform, which would spoil the match. This is particularly important when comparing a time-domain signal and a frequency-domain approximant, as will be done in the following sections. We fix $f_h = 2048$ Hz. We taper the time-domain waveforms using a Planck window function [180], before transforming them in the frequency domain.

Given the binary parameters

$$\mathbf{\Lambda} \equiv \{q, \chi_1, \chi_2\},\tag{67}$$

and calibration parameters

$$\boldsymbol{\theta} \equiv \{a_6, d_{SO}, \Delta t_{ISCO}^{22}\},\tag{68}$$

we define the *unfaithfulness* (or *mismatch*) of h_{EOB} to h_{NR} , for the same physical parameters Λ , and as a function of the calibration parameters θ , as

$$\mathcal{M}(\boldsymbol{\theta}) = 1 - \langle h_{\text{EOB}}(\boldsymbol{\Lambda}; \boldsymbol{\theta}) | h_{\text{NR}}(\boldsymbol{\Lambda}) \rangle.$$
 (69)

The goal that we set for the calibration of the SEOBNRv5 model is to find values of the calibration parameters $\theta(\Lambda)$ such that the (2,2) mode matches with the NR (2,2) mode above 99.9% (for the SEOBNRv4 model the goal was set to 99%). The 10^{-3} requirement as maximum mismatch is challenging, but still reasonable, considering that other state-of-the-art aligned-spin approximants [44,47,83] can reach mismatches of 10^{-3} or smaller against most of the NR configurations. More importantly, we need to push the accuracy of the SEOBNR models in view of more sensitive runs with current facilities and new detectors on the ground and in space [181]. A 10^{-4} goal would be extremely challenging, and would demand a more sophisticated calibration with additional parameters, as well as a careful treatment of NR errors, which are often of this order of magnitude (as estimated, for example, by comparing different resolutions or extrapolation orders of the same simulation). We also require, as in the SEOBNRv4 model, that the difference in merger time $\delta t_{\mathrm{merger}}$ [defined as the peak of the (2,2)-mode amplitude] after a low-frequency phase alignment is smaller than 5M, as the mismatch alone is not very sensitive to such differences.

 $^{^5}$ If f_l < 10 Hz, or when comparing different waveform models between each other, we instead take f_l = 10 Hz.

B. Nested-sampling analysis

Given the dimensionality of the problem and the large number of NR simulations at our disposal, it is especially important to devise a computationally efficient and flexible calibration procedure. For this work, we improve on the strategy adopted in the SEOBNRv4 model, which consisted of a Markov-chain Monte Carlo (MCMC) analysis to obtain a posterior distribution for the calibration parameters for each NR simulation. MCMC methods allow one to easily explore high-dimensional parameter spaces, and have the advantage of providing information on the structure of the calibration space, particularly on the correlations between calibration parameters. For our problem, we find the best computational performance with nested sampling [182], using the sampler NESSAI [183] through Bilby [184]. We compare our result to other samplers available in Bilby and to the EMCEE [185] MCMC sampler used to calibrate SEOBNRv4 for a few cases, finding consistent results.

We define the likelihood function to be

$$P(h^{\rm NR}|\boldsymbol{\theta}) \propto \exp\left[-\frac{1}{2}\left(\frac{\mathcal{M}_{\rm max}(\boldsymbol{\theta})}{\sigma_{\mathcal{M}}}\right)^{2} - \frac{1}{2}\left(\frac{\delta t_{\rm merger}(\boldsymbol{\theta})}{\sigma_{t}}\right)^{2}\right],$$
(70)

where $\mathcal{M}_{\rm max}(\theta)$ is the maximum unfaithfulness between EOB and NR waveforms over the total mass range $10M \leq M_{\odot} \leq 200M$, $\sigma_{\mathcal{M}}$ is chosen to be 10^{-3} , and σ_{t} is chosen to be 5M, to impose our calibration requirements. We carry out the calibration for 441 SXS NR waveforms plus 1 Einstein Toolkit NR waveform, as summarized above. We take uniform priors for all calibration parameters, specifically $a_{6} \in [-500, 500]$, $\Delta t_{\rm ISCO}^{22} \in [-100, 40]$, $d_{\rm SO} \in [-500, 500]$.

For each NR simulation we obtain a posterior distribution $P(\boldsymbol{\theta}|h^{\text{NR}})$ whose mean and variance (and mutual correlations between the parameters) relate to the calibration requirements. The next step in the calibration procedure is to compute a fit for the calibration parameters as functions of the binary parameters $\theta(\Lambda)$, starting from the set of calibration posteriors. In some cases, the correlations between the parameters lead to a secondary mode. To obtain a more regular fit, we select only one mode of each calibration posterior, based on continuity considerations. After this step, we discard samples that do not satisfy the calibration requirements for each posterior. If this would discard more than 50% of the points, we instead keep half of the original samples of the selected mode with the best likelihood values. We do this since, for a few of the most challenging NR simulations, like SXS:BBH:1124 with $q = 1, \chi_1 = \chi_2 = 0.998$, we do not find values of the calibration parameters that satisfy both requirements on \mathcal{M}_{max} and δt_{merger} . In Fig. 3 we show an example of a calibration posterior for the NR simulation SXS: BBH: 2420.

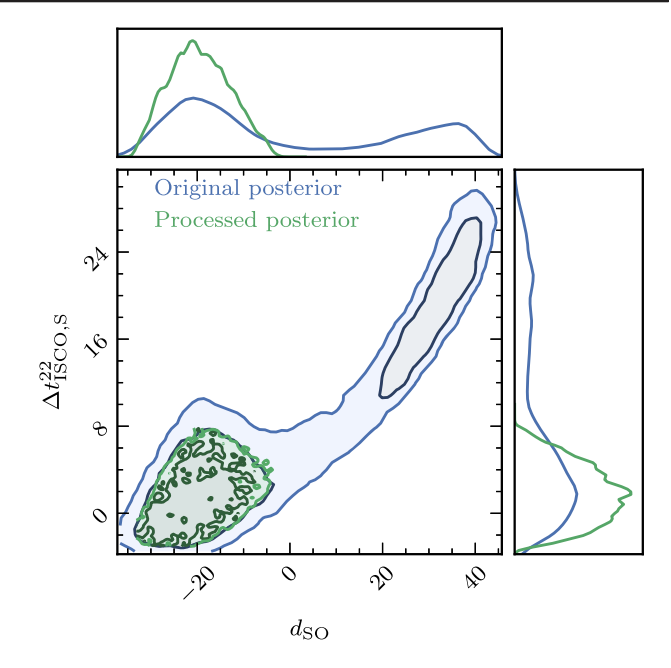


FIG. 3. Posterior for the calibration parameters $\{d_{SO}, \Delta t_{ISCO,S}^{22}\}$, obtained by comparing to the NR simulation SXS:BBH:2420 $(q=1.0,\chi_1=0.2,\chi_2=0.2)$. The blue posterior is the result of the nested-sampling analysis described in Sec. VB, and shows values mostly clustered around two distinct regions or *modes*. The green posterior is what we obtain after removing one of the two modes and keeping only the points with $\mathcal{M}_{max} < 10^{-3}$ and $\delta t_{merger} < 5M$. We use these *processed posteriors* to obtain fits for the calibration parameters across parameter space.

As done for the SEOBNRv4 model, we find it convenient to perform the calibration hierarchically, starting from noS and then moving to aligned-spin waveforms. First, we sample over 18 nonspinning configurations (the remaining 21 nonspinning simulations are only used for validation) using as calibration parameters

$$\boldsymbol{\theta}_{\text{noS}} \equiv \{a_6, \Delta t_{\text{ISCO noS}}^{22}\}. \tag{71}$$

We then fix $a_6(\nu)$, $\Delta t_{\rm ISCO,noS}^{22}(\nu)$ by the respective fits, as described in the next section, and sample over the remaining 403 aligned-spin configurations using as calibration parameters

$$\boldsymbol{\theta}_{\mathrm{S}} \equiv \{d_{\mathrm{SO}}, \Delta t_{\mathrm{ISCO,S}}^{22}\},$$
 (72)

where

$$\Delta t_{\rm ISCO}^{22} = \Delta t_{\rm ISCO,noS}^{22} + \Delta t_{\rm ISCO,S}^{22}, \tag{73}$$

and $\Delta t_{\rm ISCO,S}^{22}$ is assumed to vanish in the nonspinning limit. We investigate the possibility of adding a spin dependence to a_6 , or adding a spin-spin calibration parameter $d_{\rm SS}$ at 5PN order similar to the one used in the SEOBNRv4 model, but we find no significant improvements—for example by

comparing the mismatch and time to merger against NR taking the maximum likelihood points of the calibration posteriors. On the other hand, limiting the sampling to two dimensions makes it faster, and produces more Gaussian-like posteriors which are significantly simpler to fit.

C. Calibration-parameter fits and extrapolation

We now discuss how we obtain fits for the calibration parameters $\theta = \{a_6, \Delta t_{\rm ISCO}^{22}, d_{\rm SO}\}$ as functions of the binary parameters $\Lambda = \{q, \chi_1, \chi_2\}$, given the calibration posteriors. To help with the extrapolation, we also use some knowledge of the conservative dynamics in the $\nu \to 0$ limit. For a_6 we employ Eq. (11), which is obtained by requiring that the ISCO shift predicted by the SEOBNRv5 Hamiltonian agrees with the 1GSF ISCO shift, as explained is Sec. III A. For $\Delta t_{\rm ISCO}^{22}$ we estimate the test-mass values, for different spin magnitudes, using the results of Ref. [143]. We do so by imposing that the difference between the peak of the (2,2) mode and the peak of the orbital frequency in the EOB testmass-limit waveforms matches the one measured in the Teukolsky-code waveforms (see, e.g., Fig. 13 of Ref. [143]). We then convert the corresponding value to the difference between the ISCO and the peak of the (2,2)-mode amplitude. Since the Teukolsky-code waveforms were produced using a different EOB dynamics, we prefer to relate those quantities closer to merger, and not directly match the difference between the ISCO and the peak of the (2,2) mode of Teukolsky-code and EOB waveforms. Nevertheless, we find that the difference is not very large.

In the nonspinning limit, the data for $\theta_{\rm noS} = \{a_6, \Delta t_{\rm ISCO,noS}^{22}\}$ are simple enough to allow for an independent direct fit of the maximum-likelihood point of the calibration posteriors and TML values, using least square fits. For a_6 we use a quartic polynomial in ν , while for $\Delta t_{\rm ISCO,noS}^{22}$, that is an Ansatz of the form

$$\Delta t_{\rm ISCO,noS}^{22} = (a_0 + a_1 \nu + a_2 \nu^2 + a_3 \nu^3) \nu^{-1/5 + a_4 \nu}, \quad (74)$$

where the $\nu^{-1/5}$ factor ensures the expected test-mass scaling for $(t_{\rm peak}^{22}-t_{\rm ISCO})$ [52], and provides a better extrapolation of the fit in the $\nu\to 0$ limit. Figure 4 shows the $\{a_6,\Delta t_{\rm ISCO,noS}^{22}\}$ data and the resulting fits.

For the aligned-spin fit of $\theta_{\rm S} = \{d_{\rm SO}, \Delta t_{\rm ISCO,S}^{22}\}$, we use a similar approach as in the SEOBNRv4 model [77], with a few important differences. We fit the median of the calibration posteriors, instead of the mean, as this provides better unfaithfulness when comparing against NR. In principle, fitting the maximum-likelihood also for aligned-spin cases would give the best result, but does not turn out to be a viable option due to the lack of regularity in the data. We use three variables in the fit (ν, a_+, a_-) , instead of just (ν, χ) , where $\chi = \chi_S + \chi_A \delta/(1 - 2\nu)$, as this provides a better result, also when using a subset of NR

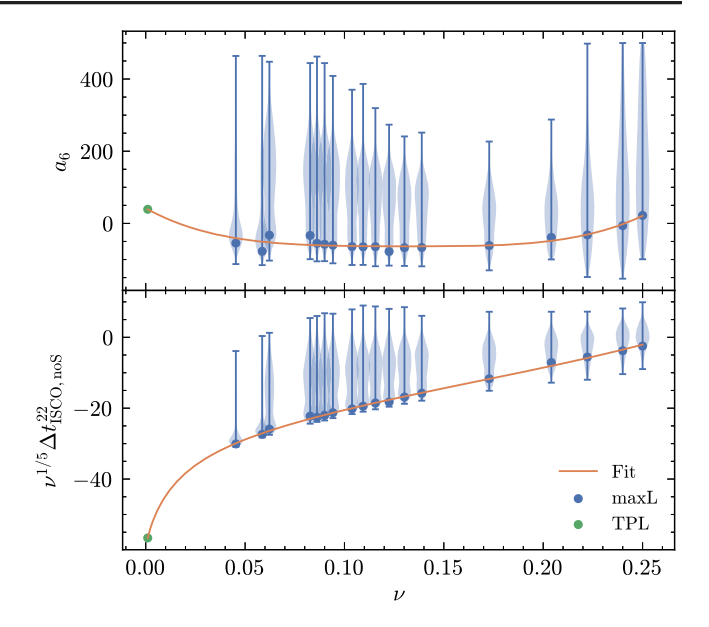


FIG. 4. Fits for the nonspinning calibration parameters $\theta_{\rm noS} = \{a_6, \Delta t_{\rm ISCO,noS}^{22}\}$. The parameters are obtained by least-square fits of the maximum likelihood points (blue dots) of the calibration posteriors (shaded violins), for a set of NR simulations with different mass ratios ν , together with estimates of the test-mass limit values (green dots). We rescale $\Delta t_{\rm ISCO,noS}^{22}$ by $\nu^{1/5}$ to improve its extrapolation in the $\nu \to 0$ limit. No processing is needed for the nonspinning calibration posteriors, as the maximum likelihood point lies in the same mode for all configurations.

simulations for the fit (see also Appendix E), or when comparing to independent sets of NRHybSur3dq8 [24] waveforms not used in the calibration. We rescale $\Delta t_{\rm ISCO,S}^{22}$ by $\nu^{1/5}$ to ensure the correct test-mass scaling.

More specifically, after removing secondary modes and discarding samples that do not meet the calibration requirements, and after rescaling $\Delta t_{\rm ISCO,S}^{22}$ by $\nu^{1/5}$, we consider the medians $\langle \boldsymbol{\theta}_{\rm S} \rangle_{(n)}$ and covariance matrices $C_{{\rm S}(n)}$ of the calibration posteriors, with n labeling each of the 442 NR simulations. We parametrize $d_{\rm SO}$ by a cubic polynomial in (ν, a_+, a_-) and $\Delta t_{\rm ISCO,S}^{22} \nu^{1/5}$ by a cubic polynomial in (ν, a_+, a_-) with an additional a_+^4 feature. We determine the coefficients of these polynomials by minimizing the following function, using a Sequential Least Squares Programming minimization algorithm [77],

$$\chi_{s}^{2} \equiv \sum_{n \in \mathcal{S}_{s}} \frac{w}{2} (\boldsymbol{\theta}_{S} - \langle \boldsymbol{\theta}_{S} \rangle_{(n)}) (C_{S}^{-1})_{(n)} (\boldsymbol{\theta}_{S} - \langle \boldsymbol{\theta}_{S} \rangle_{(n)})^{T} + \chi_{TML}^{2},$$
(75)

where $\chi^2_{\rm TML}$ is a term that penalizes deviations from the test-mass limit of $\Delta t^{22}_{\rm ISCO,S}$ and takes the form

$$\chi_{\text{TML}}^{2} = \sum_{\chi, \neq 0} \frac{(\Delta t_{\text{ISCO,S}}^{22} - \Delta t_{\text{ISCO},\chi_{i}}^{22,\text{TML}})^{2}}{\sigma_{\text{TML}}^{2}},$$
 (76)

in which $\Delta t_{\rm ISCO,\chi_i}^{22,\rm TML}$ are the estimated test-mass values of $\Delta t_{\rm ISCO,S}^{22}$, for different spin magnitudes χ_i for which Teukolsky waveforms are available, and we take $\sigma_{\rm TML}=5M$. As for the SEOBNRv4 model, the function w is a weighting function of the form

$$w \equiv \chi_1^2 + \chi_2^2 + \frac{|\chi|}{2\nu},\tag{77}$$

which accounts for the inhomogeneous distribution of NR simulations in the BBH parameter space.

We finally list the calibration-parameter fits:

$$a_6 = 329523.262\nu^4 - 169019.14\nu^3 + 33414.4394\nu^2 - 3021.93382\nu + 41.787788,$$
 (78)

$$\Delta t_{\rm ISCO,noS}^{22} = \nu^{-1/5 + 10.051322\nu} (55565.2392\nu^3 - 9793.17619\nu^2 - 1056.87385\nu - 59.62318), \tag{79}$$

$$\Delta t_{\rm ISCO,S}^{22} = \nu^{-1/5} (-6.789139 a_{+}^{4} + 5.399623 a_{+}^{3} + 6.389756 a_{+}^{2} a_{-} - 132.224951 a_{+}^{2} \nu + 49.801644 a_{+}^{2}$$

$$+ 8.392389 a_{+} a_{-}^{2} + 179.569825 a_{+} a_{-} \nu - 40.606365 a_{+} a_{-} + 384.201019 a_{+} \nu^{2} - 141.253182 a_{+} \nu$$

$$+ 17.571013 a_{+} - 16.905686 a_{-}^{2} \nu + 7.234106 a_{-}^{2} + 144.253396 a_{-} \nu^{2} - 90.192914 a_{-} \nu + 14.22031 a_{-}), \tag{80}$$

$$d_{SO} = -7.584581a_{+}^{3} - 10.522544a_{+}^{2}a_{-} - 42.760113a_{+}^{2}\nu + 18.178344a_{+}^{2} - 17.229468a_{+}a_{-}^{2} + 362.767393a_{+}a_{-}\nu - 85.803634a_{+}a_{-} - 201.905934a_{+}\nu^{2} - 90.579008a_{+}\nu + 49.629918a_{+} - 7.712512a_{-}^{3} - 238.430383a_{-}^{2}\nu + 69.546167a_{-}^{2} - 1254.668459a_{-}\nu^{2} + 472.431938a_{-}\nu - 39.742317a_{-} + 478.546231\nu^{3} + 679.52177\nu^{2} - 177.334832\nu - 37.689778.$$

$$(81)$$

To ensure a robust behavior of the fits between the last calibration points and extreme-mass-ratio limit, we perform exhaustive checks of the sanity of the waveform model across a broad range of the parameter space $(q \in [1, 100],$ covering the full spin range). The tests include visual inspections of the waveforms, assessing stability in response to perturbations of the intrinsic parameters, verifying the monotonicity of the amplitude and frequency of the (2,2) mode up its peak and confirming that the higher modes consistently maintain amplitudes smaller than the (2,2) mode, up to the merger.

VI. PERFORMANCE OF THE SEOBNRV5HM MODEL AGAINST NUMERICAL-RELATIVITY SIMULATIONS

To assess the impact of the improvements introduced in the SEOBNRv5HM waveform model, we compare it to the set of NR simulations described in Sec. V, and to other state-of-the-art aligned-spin approximants. We do so by performing unfaithfulness computations, as well as comparisons of angular-momentum flux and binding energy against NR. Finally, we assess the computational efficiency of the model for GW data-analysis purposes, providing benchmarks.

A. Faithfulness for multipolar waveforms

The GW signal emitted by a quasicircular aligned-spin BBH system depends on 11 parameters: the masses and spins $\lambda = \{m_{1,2}, \chi_{1,2}\}$, the direction of the observer from the source described by (ι, φ_0) , the luminosity distance d_L , the polarization angle ψ , the location in the sky of the detector (θ, ϕ) , and the time of arrival t_c . The strain in the detector caused by a passing GW can be expressed as

$$h(t) \equiv F_{+}(\theta, \phi, \psi) h_{+}(t; \iota, \varphi_{0}, d_{L}, \lambda, t_{c})$$
$$+ F_{\times}(\theta, \phi, \psi) h_{\times}(t; \iota, \varphi_{0}, d_{L}, \lambda, t_{c}), \tag{82}$$

where $F_{+,\times}$ are the antenna pattern functions [177,178]. The strain in Eq. (82) can be expressed in terms of an effective polarization angle $\kappa(\theta,\phi,\psi)$ as

$$h(t) = \mathcal{A}(\theta, \phi)(h_{+} \cos \kappa + h_{\times} \sin \kappa), \tag{83}$$

where the dependences of κ , h_+ , and h_\times have been removed to ease the notation, and the definition of the coefficient $\mathcal{A}(\theta,\phi)$ can be found in Refs. [78,81].

To assess the agreement between two waveforms with higher-order multipoles [46,78,81], which we denote as the signal, h_s and the template, h_t , observed by a detector, we define the faithfulness function [78,81],

$$\mathcal{F}(M_{s}, \iota_{s}, \varphi_{0s}, \kappa_{s}) = \max_{\iota_{c}, \varphi_{0t}, \kappa_{t}} \left[\frac{\langle h_{s} | h_{t} \rangle}{\sqrt{\langle h_{s} | h_{s} \rangle \langle h_{t} | h_{t} \rangle}} \Big|_{\lambda_{s}(\iota_{s} = \iota_{0_{s}}) = \lambda_{t}(\iota_{t} = \iota_{0_{t}})} \right],$$
(84)

where the inner product is defined in Eq. (65). Typically, we set the inclination angle of the template and the signal to be the same, while the coalescence time, azimuthal, and effective polarization angles of the template, $(t_{0_t}, \varphi_{0_t}, \kappa_t)$, are adjusted to maximize the faithfulness of the template. The maximizations over the coalescence time t_c , and coalescence phase φ_{0t} are performed numerically, while

the optimization over the effective polarization angle κ_t is done analytically as described in Ref. [186].

To reduce the dimensionality of the faithfulness function it is useful to define the sky-and-polarization-averaged faithfulness [80,81] as

$$\bar{\mathcal{F}}(M_{\rm s}, \iota_{\rm s}) \equiv \frac{1}{8\pi^2} \int_0^{2\pi} d\kappa_{\rm s} \int_0^{2\pi} d\varphi_{0\rm s} \mathcal{F}(M_{\rm s}, \iota_{\rm s}, \varphi_{0\rm s}, \kappa_{\rm s}). \tag{85}$$

We also define the sky-and-polarization-averaged, signal-to-noise-ratio (SNR)-weighted faithfulness as [78,81]

$$\bar{\mathcal{F}}_{SNR}(M_{s}, \iota_{s}) \equiv \sqrt[3]{\frac{\int_{0}^{2\pi} d\kappa_{s} \int_{0}^{2\pi} d\varphi_{0s} \mathcal{F}^{3}(M_{s}, \iota_{s}, \varphi_{0s}, \kappa_{s}) SNR^{3}(\iota_{s}, \varphi_{0s}, \kappa_{s})}{\int_{0}^{2\pi} d\kappa_{s} \int_{0}^{2\pi} d\varphi_{0s} SNR^{3}(\iota_{s}, \varphi_{0s}, \kappa_{s})}},$$
(86)

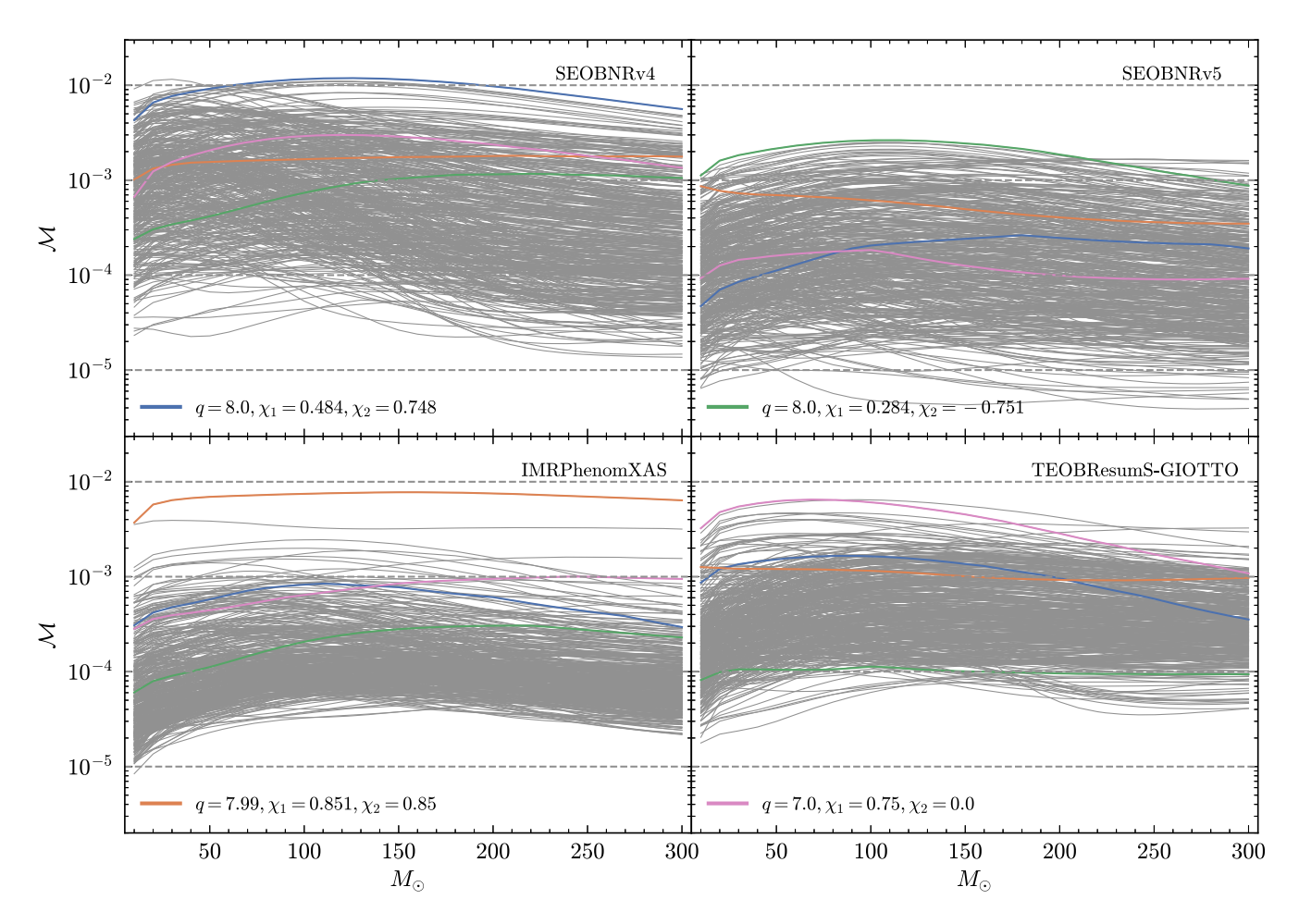


FIG. 5. (2,2)-mode mismatch over a range of total masses between 10 and $300M_{\odot}$, between different aligned-spin approximants and the 442 NR simulations used in this work. The colored lines highlight cases with the worst maximum mismatch for each model. Note that SEOBNRv5 has no outliers beyond 0.3% and many more cases at lower unfaithfulness, especially compared to SEOBNRv4 and TEOBResumS-GIOTTO.

where the $SNR(l_s, \varphi_{0_s}, \theta_s, \phi_s, \kappa_s, d_{Ls}, \lambda_s, t_{cs})$ is defined as

$$SNR(\iota_{\rm s}, \varphi_{0_{\rm s}}, \theta_{\rm s}, \phi_{\rm s}, \kappa_{\rm s}, d_{L{\rm s}}, \lambda_{\rm s}, t_{c{\rm s}}) \equiv \sqrt{(h_{\rm s}, h_{\rm s})}. \tag{87}$$

The weighting by the SNR in Eq. (87) takes into account the dependence on the phase and effective polarization of the signal at a fixed distance. Finally, we define the sky-and-polarization-averaged, SNR-weighted unfaithfulness (or mismatch) as

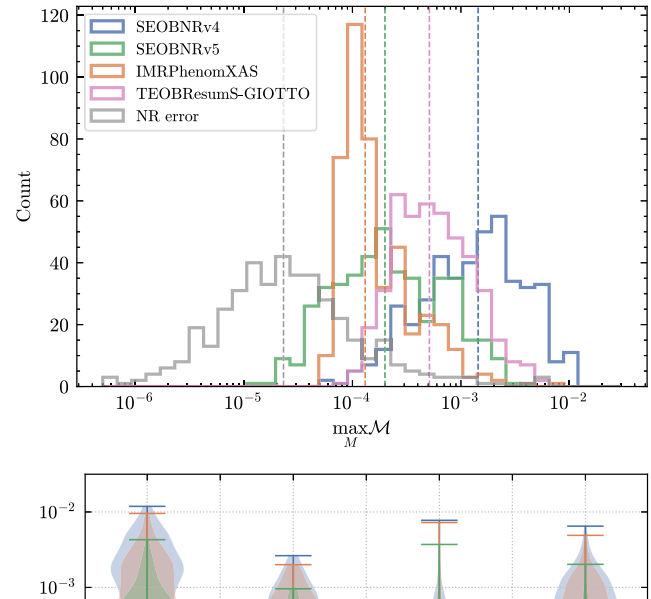
$$\overline{\mathcal{M}}_{SNR} = 1 - \bar{\mathcal{F}}_{SNR}.$$
 (88)

B. Accuracy of SEOBNRv5 (2,2) mode

We start by considering (2,2)-mode only mismatches. In this case, the result does not depend on the inclination, and the mismatch definition reduces to the one used in Sec. V. Figure 5 shows the (2,2)-mode mismatch over a range of total masses between 10 and $300M_{\odot}$ using the 442 NR simulations summarized in Sec. V for different state-of-the-art aligned-spin approximants: SEOBNRv5, its predecessor SEOBNRv4 [77], the aligned-spin model from the other EOB family TEOBResumS [64,83,113,114], and IMRPhenomXAS [44], from the fourth generation of Fourier-domain phenomenological waveform models. All approximants are called through LALSimulation, except for SEOBNRv5 and for TEOBResumS, for which we use the latest available public version TEOBResumSv4.1.4-GIOTTO.

The colored lines highlight cases with the worst maximum mismatch for each model: as expected, the most challenging cases have high mass ratio and high spins, as all models have been calibrated to few NR simulations in this region of parameter space. We note that SEOBNRv5 has no outliers beyond 0.3% and many more cases at lower unfaithfulness, especially compared to SEOBNRv4 and TEOBResumS-GIOTTO. Comparing the two upper panels of Fig. 5, we can see in particular that SEOBNRv5 yields unfaithfulnesses almost 1 order of magnitude smaller than those of its predecessor SEOBNRv4 model.

The top panel of Fig. 6 shows histograms of the maximum (2,2)-mode mismatch over the same range of total masses. We also show an estimate of the NR error computed as the mismatch between NR simulations with the highest and second-highest resolutions, if available. The mismatch between NR simulations of the highest resolution and different extrapolation order is typically 1 order of magnitude smaller than the one obtained comparing different resolutions; hence we do not show it in these comparisons. The vertical dashed lines correspond to the medians



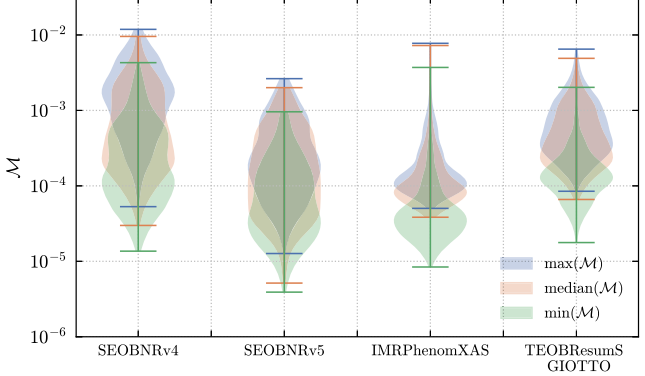


FIG. 6. Top panel: histogram of the maximum (2,2)-mode mismatch over a range of total masses between 10 and $300M_{\odot}$, between different aligned-spin approximants and the 442 NR simulations used in this work. The NR error is estimated by computing the mismatch between NR simulations with the highest and second-highest resolutions. The vertical dashed lines show the medians. Bottom panel: distribution of the maximum (blue), median (orange), and minimum (green) mismatch over the same range of total masses for the different models.

of the distributions. Overall IMRPhenomXAS achieves the lowest median unfaithfulness (1.31×10^{-4}), while still having two outliers above 0.3%, with SEOBNRv5 closely following with median mismatch 1.99×10^{-4} , but a larger tail of cases with low unfaithfulness approaching 10^{-5} . TEOBResumS-GIOTTO is slightly less accurate with median mismatch 5.12×10^{-4} , while SEOBNRv4 is the least faithful model with median value 1.44×10^{-3} , almost 1 order of magnitude larger than SEOBNRv5. These results are summarized in Table I, together with the fraction of cases falling below 10^{-3} and 10^{-4} for each approximant.

The NR error is about 1 order of magnitude smaller than the SEOBNRv5 modeling error, with median value $\sim 2 \times 10^{-5}$. Still, there are a few cases where the two are comparable, and improving the accuracy of the NR simulations used to calibrate the model would be critical to reducing the modeling errors by another order of magnitude. The bottom panel of Fig. 6 provides a complementary

⁶This corresponds to the commit fc4595df72b2eff4b36e563-f607eab5374e695fe of the public bitbucket repository https://bitbucket.org/eob_ihes/teobresums, and it is the latest tagged version at the time of this publication.

TABLE I. Summary of the (2,2)-mode mismatch over a range of total masses between 10 and $300M_{\odot}$, between different aligned-spin approximants and the 442 NR simulations used in this work. We display the median of the maximum mismatch across total mass, and the fraction of cases falling below 10^{-3} and 10^{-4} .

| Approximant | SEOBNRv4 | SEOBNRv5 | IMRPhenomXAS | TEOBResumS-GIOTTO |
|---|------------------------------------|-------------------------------------|-------------------------------------|--------------------------------------|
| Median $\max_{M} \mathcal{M}$ % $\max_{M} \mathcal{M} < 10^{-3}$ % $\max_{M} \mathcal{M} < 10^{-4}$ | 1.44×10^{-3} 38% 1% | 1.99×10^{-4} 90% 27% | 1.31×10^{-4} 97% 29% | 5.12 × 10 ⁻⁴ 76% 1% |

summary of the unfaithfulness calculation, by showing the distribution of the maximum (blue), median (orange), and minimum (green) mismatch over the same range of total masses for the different models.

We find that 10% of the cases are above 0.1% maximum mismatch for SEOBNRv5: most of those correspond, as expected, to high spins, both for large mass ratios and for $q \simeq 1$ where spin magnitudes can reach values up to 0.998. In a future update of the model, the description of these cases could be improved by suitably including the full 5PN spin contributions [next-to-next-to-next-to-leading order (NNNLO) SO and SS, NLO S³ and S⁴] to the conservative dynamics recently obtained in Refs. [154–157,187–192], by including all spin-contributions up to 3.5PN to the waveform modes, as derived in Refs. [127,164], or by additional spin-dependent calibration coefficients other than d_{SO} .

Other challenging cases for SEOBNRv5 are those with large mass ratio, small a_+ , but large secondary spin, for example SXS:BBH:1430, with parameters $(q, \chi_1, \chi_2) =$ (8.0, 0.284, -0.751). The calibration term, which has the form $\sim a_+ d_{SO}$, is suppressed, and deviations of the model from NR are only partially captured by having d_{SO} itself depending also on the spin difference a_{-} . To understand what could be the error when one has exactly $a_{+} = 0$, but a_{-} is large, we can compare the model to NRHybSur3dq8 waveforms: taking q = 8 and varying χ_2 , while fixing χ_1 so that $a_+ = 0$, we see at most mismatches around 0.004 for large negative secondary spin $\chi_2 < -0.9$, where NRHybSur3dq8 is also extrapolating from its training region ($\chi_i \leq 0.8$). While additional calibration terms with a different spin dependence could improve these cases, this shows that for the moment the analytical spin information captures the correct behavior at a level comparable to other modeling errors.

C. Accuracy of SEOBNRv5HM modes

We now turn to mismatches for the full polarizations, including higher multipoles. Figure 7 shows the sky-and-polarization averaged, SNR-weighted mismatch, for inclination $\iota=\pi/3$, over a range of total masses between 20 and $300M_{\odot}$ between the 441 SXS NR simulations used in this work and different multipolar aligned-spin approximants: SEOBNRv4HM [78], SEOBNRv5HM, TEOBResumS-GIOTTO [64,83,113,114],

and IMRPhenomXHM [46]. For each approximant we include all modes available, while for NR waveforms we use modes up to $\ell_{\max} = 5$. The modes included are specifically $(\ell, |m|) = (2, 2), (2, 1), (3, 3), (4, 4), (5, 5)$ for SEOBNRv4HM; $(\ell, |m|) = (2, 2), (2, 1), (3, 3), (3, 2), (4, 4), (4, 3), (5, 5)$ for SEOBNRv5HM; $(\ell, |m|) = (2, 2), (2, 1), (3, 3), (3, 2), (4, 4)$ for IMRPhenomXHM; and $(\ell, |m|) = (2, 2), (2, 1), (3, 3), (3, 2), (3, 1), (4, 4), (4, 3), (4, 2)$ for TEOBResumS-GIOTTO.

In this comparison we omit the Einstein Toolkit simulation, for which we only have the (2,2) mode. As in the previous results, we highlight with a different color cases with the worst maximum mismatch for each model: unsurprisingly the worst cases are at the corners of the NR parameter space, and correspond to configurations with very high q and nonzero spins, where the impact of higher multipoles is substantial, also due to the significant inclination $i = \pi/3$.

First of all, we note that all models perform worse compared to the (2,2)-mode only case, as expected due to the limited alignment freedom with a global phase and time shift, but also because the higher modes are available today at lower PN order than the dominant one, and their modeling close to merger is complicated by numerical noise in NR simulations.

Focusing on the upper panels, comparing SEOBNRv4HM and SEOBNRv5HM, we see an overall improvement, with many more cases between 10^{-4} and 10^{-3} for SEOBNRv5HM, and just a few outliers above 1% for large values of the total mass. The improvement for low total mass, where an accurate inspiral is primarily important, is particularly significant, and SEOBNRv5HM is always well below 1%, never exceeding 0.3%. On the other hand the increase of the mismatch with the total mass for SEOBNRv5HM, absent in the (2,2)-mode only comparison, points to limitations in the merger-ringdown modeling of the higher modes, as in other models. A related limitation is the absence of some of the higher modes in the waveform models, which contribute significantly to the ringdown signal for high mass-ratio systems at a high inclination, as we quantify below. Focusing on the bottom panels, we

⁷For TEOBResumS-GIOTTO we do not include the (5,5) mode, after finding that, in the version of the code used for these comparisons, it has an unphysically large amplitude close to merger in some corners of the parameter space (equal-mass, large opposite spins, as for example SXS:BBH:2132).

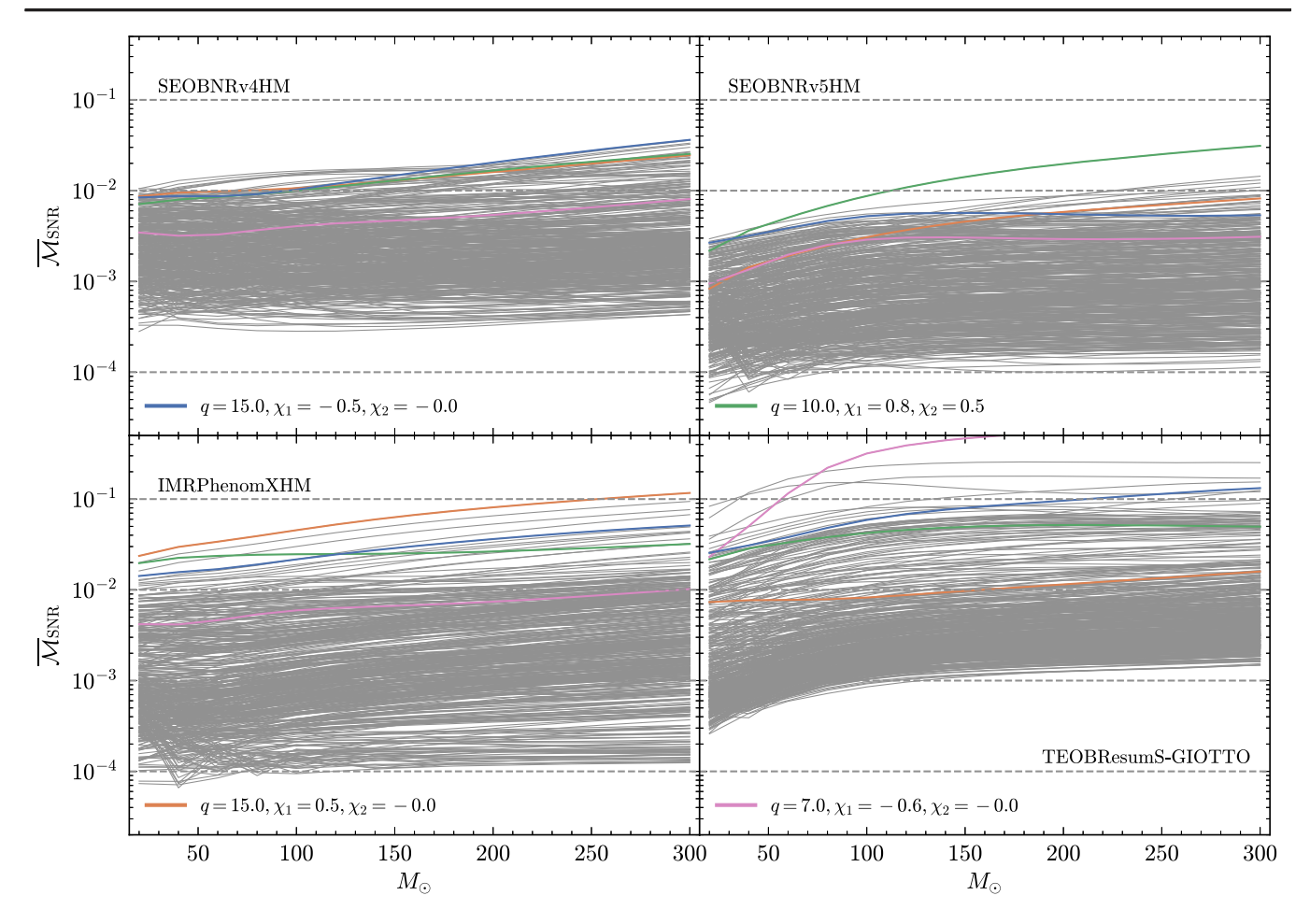


FIG. 7. The sky-and-polarization averaged, SNR-weighted mismatch, for inclination $\iota = \pi/3$, over a range of total masses between 20 and $300M_{\odot}$ between different aligned-spin multipolar approximants and the 441 SXS NR simulations used in this work. The colored lines highlight cases with the worst maximum mismatch for each model.

see that IMRPhenomXHM also has many cases between 10^{-4} and 10^{-3} , but reaches high values of the unfaithfulness when compared to high mass-ratio, spinning configurations, in which higher-mode content is more significant. Specifically, the unfaithfulness exceeds 10% for the most challenging configurations with q=15. We point out that IMRPhenomXHM has not been calibrated to q=15 SXS simulations, which became only recently available [30], but was calibrated to private q=18 BAM waveforms, with different spin values, which have not been used for SEOBNRv5HM. TEOBResumS-GIOTTO achieves unfaithfulness between 10^{-3} and 10^{-2} for most cases, but also has an appreciable number of outliers reaching mismatch 10%, possibly pointing to robustness issues in some of the higher modes close to merger.

In order to quantify how much the increase of the mismatch with the total mass is related to the missing modes, we show in Fig. 8 the sky-and-polarization averaged, SNR-weighted mismatch, for inclination $\iota=\pi/3$, over a range of total masses between 20 and $300M_{\odot}$ of NR waveforms with the same modes as SEOBNRV5HM

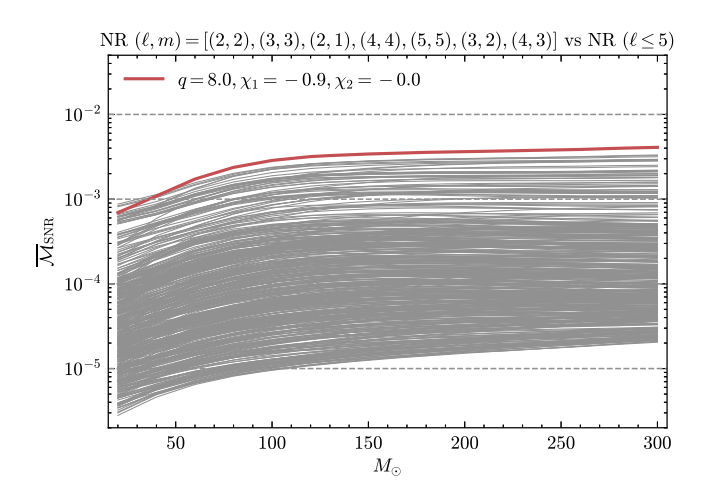
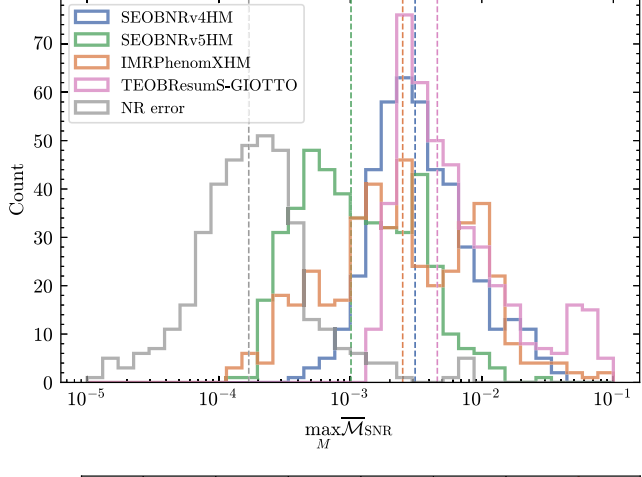


FIG. 8. The sky-and-polarization averaged, SNR-weighted mismatch, for inclination $\iota = \pi/3$, over a range of total masses between 20 and $300M_{\odot}$, of NR waveforms with the same modes as SEOBNRv5HM $(\ell, m) = (2, 2), (3, 3), (2, 1), (4, 4), (5, 5), (3, 2), (4, 3)$ against NR waveforms with all $(\ell \le 5)$ modes.



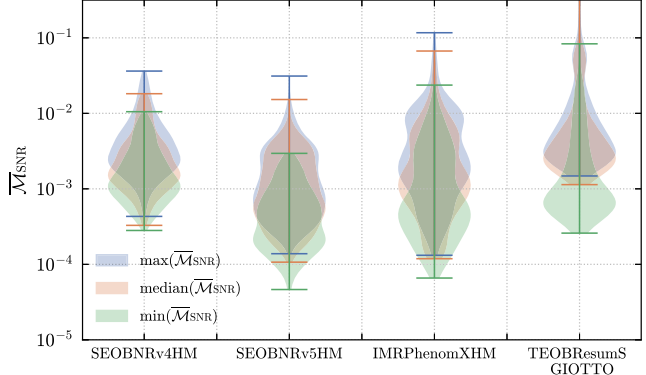


FIG. 9. Top panel: histogram of the maximum sky-and-polarization averaged, SNR-weighted mismatch, for inclination $\iota=\pi/3$, over a range of total masses between 20 and $300M_{\odot}$, between different aligned-spin multipolar approximants and the 441 SXS NR simulations used in this work. The NR error is estimated by computing the mismatch between NR simulations with the highest and second-highest resolutions. The vertical dashed lines show the medians. Bottom panel: distribution of the maximum (blue), median (orange), and minimum (green) mismatch over the same range of total masses for the different models.

 $(\ell, m) = (2, 2), (3, 3), (2, 1), (4, 4), (5, 5), (3, 2), (4, 3)$ against NR waveforms with all $(\ell \le 5)$ modes. As expected we see an increase of the mismatch with total mass, indicating that the error due to neglecting some higher modes is mostly important in the ringdown, and we see it

can reach more than 0.4% for high q and large spins. This tells us that to reach the same accuracy of just the (2,2) mode (<0.3%) for the full polarizations at high ι one would need to include additional modes in SEOBNRv5HM.

Figure 9 summarizes the comparison of Fig. 7: in the top panel we show histograms of the maximum unfaithfulness over the same range of total masses, with the vertical lines corresponding to the medians of the distributions, and an estimate of the NR error computed as the mismatch between NR simulations with different resolutions. As for the (2,2)-mode only case, the NR error is about 1 order of magnitude smaller than the SEOBNRv5HM modeling error, with median $\sim 1 \times 10^{-4}$. Overall SEOBNRv5HM achieves a lower unfaithfulness than SEOBNRv4HM. IMRPhenomXHM, and TEOBResumS-GIOTTO, with the median value 1.01×10^{-3} and only seven cases above 1%, as summarized in Table II. The violin plots in the bottom panel provide a further comparison by showing the distribution of the maximum (blue), median (orange), and minimum (green) mismatch for each model.

We note that in the unfaithfulness computation we include all modes up to $\ell_{max}=5$ in the NR waveforms, while the (5,5) mode is not included in IMRPhenomXHM and TEOBResumS-GIOTTO. To check the impact of neglecting the (5,5) mode in these two models, we also repeat the comparison presented in this section using only multipoles up to $\ell_{max}=4$, in both the models and the NR waveforms. We find a result very similar to what is shown above, with all models displaying a slightly better performance, due to fewer missing modes, and the same hierarchy for the accuracy of different approximants.

To validate SEOBNRv5HM, we compare it to the multipolar aligned-spin surrogate model NRHybSur3dq8 [24]. This model was built for binaries with mass ratios 1–8 and spin magnitudes up to 0.8, and provides waveforms with errors comparable to the NR accuracy in the region where the model was trained. NRHybSur3dq8 waveforms were not used in the construction of SEOBNRv5HM, so this is an important validation check of the NR calibration pipeline. We point out that NRHybSur3dq8 is trained on NR waveforms hybridized with PN and SEOBNRv4 waveforms in the early inspiral. In the following comparisons, we generate waveforms from an initial geometric frequency

TABLE II. Summary of the sky-and-polarization averaged, SNR-weighted mismatch, for inclination $\iota = \pi/3$, over a range of total masses between 20 and $300M_{\odot}$, between different aligned-spin multipolar approximants and the 441 SXS NR simulations used in this work. We display the median of the maximum mismatch across total mass, and the fraction of cases falling below 10^{-2} and 10^{-3} .

| Approximant | SEOBNRv4HM | SEOBNRv5HM | IMRPhenomXHM | TEOBResumS-GIOTTO |
|---|------------------------------------|-------------------------------------|-------------------------------------|--------------------------------------|
| Median $\max_{M} \bar{\mathcal{M}}_{SNR}$ % $\max_{M} \bar{\mathcal{M}}_{SNR} < 10^{-2}$ % $\max_{M} \bar{\mathcal{M}}_{SNR} < 10^{-3}$ | 3.11×10^{-3} 88% 5% | 1.01×10^{-3} 98% 49% | 2.50×10^{-3} 86% 23% | $4.59 \times 10^{-3} \\ 74\% \\ 0\%$ |

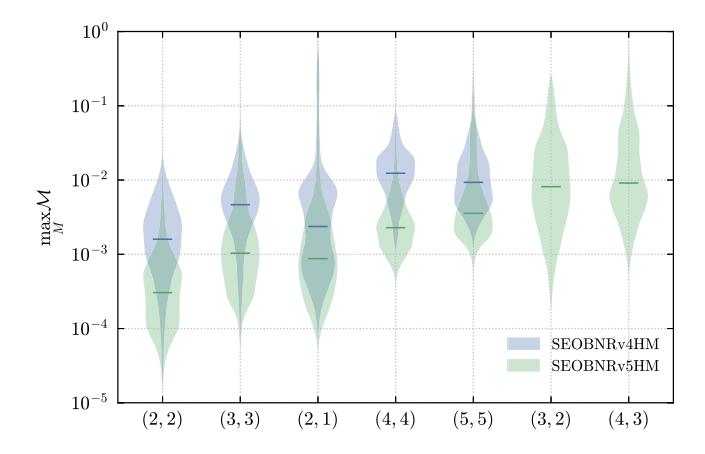


FIG. 10. Mode-by-mode mismatches between SEOBNRv4HM, SEOBNRv5HM, and NRHybSur3dq8, for 5000 random configurations with $q \in [1,8], |\chi_i| \le 0.9$. For each mode we show the maximum mismatch over a range of total masses between 10 and $300M_{\odot}$. The horizontal lines show the medians.

of 0.015, for which the impact of the hybridization should not be large.

Figure 10 compares SEOBNRv4HM and SEOBNRv5HM against NRHybSur3dq8, showing a kernel density estimation of the distribution of the maximum mode-by-mode mismatches between them. We use 5000 random configurations with $q \in [1,8], |\chi_i| \leq 0.9$, allowing some extrapolation outside of the surrogate's training region, as to also test the extrapolation of the SEOBNRv5HM calibration.

First, we notice that the (2,2)-mode median mismatch $\sim 3 \times 10^{-4}$ is comparable to the one against NR, only slightly higher because of the larger number of challenging cases with high q and high spin in this comparison. The maximum unfaithfulness for the (2,2) mode, which is reached, as expected, for large mass ratios and positive spins, remains below 0.01, if we limit the comparison to the region $q \in [1,8], |\chi_i| \le 0.8$ where the surrogate was trained, and can be only slightly above 0.01 if going up to $|\chi_i| = 0.9$ in the surrogate's extrapolation region. This confirms a good extrapolation of the SEOBNRv5HM fits. Comparing to SEOBNRv4HM, we have as expected fewer cases above 0.01, and much lower median unfaithfulness.

Going to the higher multipoles, we see larger errors for the smaller higher modes, as for most other state-of-the-art models. The subdominant higher modes in NR simulations are noisier, and more difficult to model (both for EOB models and for NRHybSur3dq8). Some of the higher modes also include considerably less analytical information compared to the (2,2) mode (see Appendix B), and adding the full 3.5PN contributions from Refs. [127,164] would likely bring a significant improvement to some of them. Nonetheless, we see a consistent improvement comparing SEOBNRv5HM to SEOBNRv4HM, mostly due to the enhanced calibration and merger-ringdown description.

The (2,1) mode shows a tail of cases with large mismatches for both SEOBNRv5HM and SEOBNRv4HM: as also discussed in Ref. [78] those are cases with a minimum in the amplitude close to merger, which can be especially difficult to model given that the current mergerringdown Ansatz assumes a monotonic postmerger amplitude evolution. Nonetheless, these are configurations where the (2,1) mode is highly suppressed, and would not impact significantly in the full polarizations. We also compare the (3,2) and (4,3) modes of SEOBNRv5HM against NRHybSur3dq8 (these modes are not included in SEOBNRv4HM). We see that these modes show the largest modeling errors, which is expected considering they are among the smallest modes for most configurations, and also keeping in mind that the mode-mixing modeling in the ringdown is approximated.

Figure 11 shows a similar comparison against NRHybSur2dq15 [30], limited to the modes modeled by the surrogate. This model was built for binaries with mass-ratios 1–15, primary spin up to 0.5 and no secondary spin. We consider 5000 random configurations with $q \in [1,15], |\chi_1| \leq 0.6, \chi_2 = 0$, allowing again some extrapolation outside of the surrogate's training region, as to also test the extrapolation of the SEOBNRv5HM calibration fits. We see a similarly large improvement for all the modes comparing SEOBNRv5HM to SEOBNRv4HM, and the (2,2) mode result, with maximum value 2.3×10^{-3} and median 1.5×10^{-4} , confirms the robustness of the calibration procedure.

In Fig. 12 we show the sky-and-polarization averaged, SNR-weighted mismatch, for inclination $\iota=\pi/3$, between SEOBNRv5HM and NRHybSur3dq8, for 2000 random configurations with $q \in [1,8], |\chi_i| \leq 0.8$. In particular, we plot the maximum mismatch as a function of the mass ratio q and the primary spin χ_1 . The unfaithfulness grows with

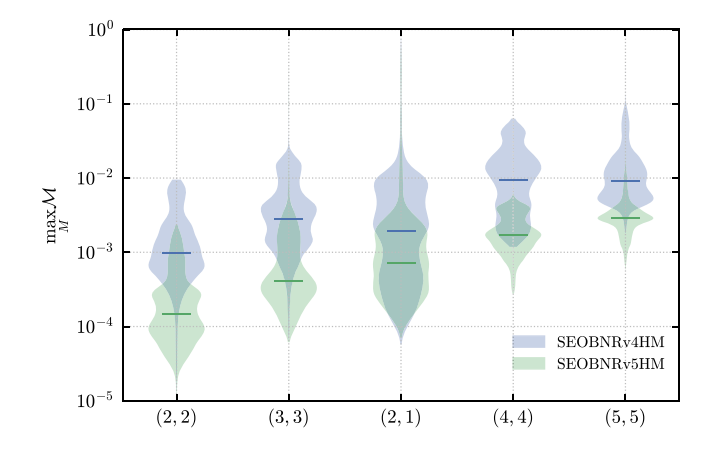


FIG. 11. Mode-by-mode mismatches between SEOBNRv4HM, SEOBNRv5HM, and NRHybSur2dq15, for 5000 random configurations with $q \in [1,15], |\chi_1| \le 0.6, \chi_2 = 0$. For each mode we show the maximum mismatch over a range of total masses between 10 and $300M_{\odot}$. The horizontal lines show the medians.

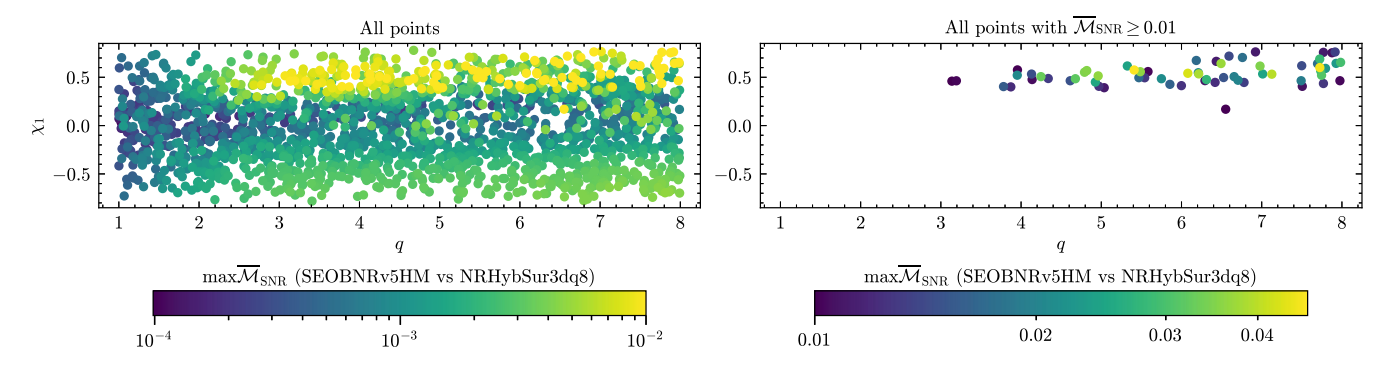


FIG. 12. Sky-and-polarization averaged, SNR-weighted mismatch, for inclination $i = \pi/3$, between SEOBNRv5HM and NRHyb-Sur3dq8, for 2000 random configurations with $q \in [1,8], |\chi_i| \le 0.8$. We show maximum mismatch over a range of total masses between 20 and $300M_{\odot}$ as a function of the mass-ratio q and the primary spin χ_1 .

mass ratio and spin, with the highest unfaithfulness reaching 0.04. This effect also is enhanced by the fact that we start all the waveforms at the same frequency, and for higher mass ratios, the number of cycles in band grows as $\sim 1/\nu$.

We plot in Fig. 13 a similar comparison between SEOBNRv5HM and IMRPhenomXHM, for 2000 random configurations with $q \in [1,20], |\chi_i| \le 0.99$ in order to examine the behavior of the models outside of the region in which they were calibrated to NR. As in the previous comparison, the unfaithfulness grows with mass ratio and spin, and can reach very large values for $q \simeq 20$ and high $\chi_{\rm eff}$. This confirms that waveform systematics are important, even for aligned-spin systems observed by current detectors, in the region where waveform models are not calibrated to NR simulations.

D. Accuracy of SEOBNRv5 angular-momentum flux and binding energy

The performance of waveform models is typically assessed by computing the unfaithfulness between the waveforms produced by the model and NR waveforms with corresponding parameters, as the waveform itself is the relevant quantity used in data analysis. In EOB models,

however, the knowledge of the binary's dynamics allows us to complement the waveform comparison with other dynamical quantities. Since the calibration of the model to NR is based on the waveforms, seeing an improvement in different dynamical quantities is a powerful check of the physical robustness of the model. In particular, we examine the angular-momentum flux radiated at infinity [193,194], and the binding energy [195–197].

We compute the NR angular-momentum flux at infinity from the waveform modes using

$$\dot{J} = -\frac{1}{8\pi} \sum_{\ell=2}^{\ell_{\text{max}}} \sum_{m=-\ell}^{\ell} m \Im(\dot{h}_{\ell m} h_{\ell m}^*), \tag{89}$$

where we assume $\ell_{\text{max}} = 8$. For clarity, we normalize the flux by the leading (Newtonian) one for circular orbits,

$$\dot{J}_N = \frac{32}{5} \nu^2 (M\Omega)^{7/3},\tag{90}$$

where we estimate the NR orbital frequency Ω_{NR} from the NR (2,2)-mode frequency as

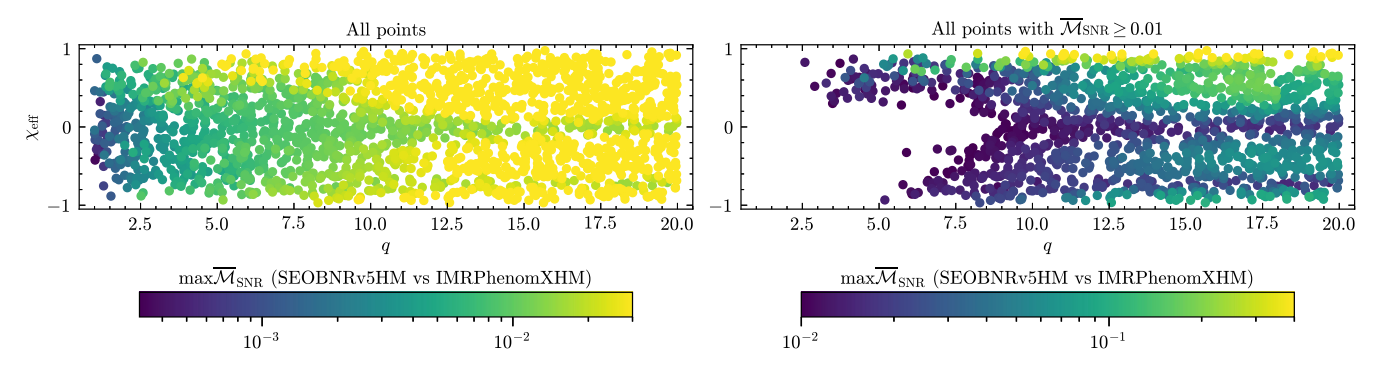


FIG. 13. Sky-and-polarization averaged, SNR-weighted mismatch, for inclination $i = \pi/3$, between SEOBNRv5HM and IMRPhenomXHM, for 2000 random configurations with $q \in [1, 20], |\chi_i| \le 0.99$. We show maximum mismatch over a range of total masses between 20 and $300M_{\odot}$ as a function of the mass ratio q and the effective spin $\chi_{\rm eff}$.

$$\Omega_{\rm NR} \equiv \frac{\omega_{22}^{\rm NR}}{2}.\tag{91}$$

We denote the normalized flux as

$$\dot{\hat{J}} = \frac{\dot{J}}{\dot{J}_N}.\tag{92}$$

We note again that the SEOBNRv5 flux does not include NQC corrections, and we practically compute it from the dynamics as $\dot{J}=\dot{p}_{\phi}$. In the following, we always consider it as a function of $\Omega_{\rm EOB}$, which is read from the orbital dynamics.

As an example, in Fig. 14 we compare the SEOBNRv4 and SEOBNRv5 angular-momentum fluxes against the one extracted from the NR simulation BFI:q2-3d-95:001 with parameters $(q,\chi_1,\chi_2)=(1.0,-0.95,-0.949)$. We plot the fluxes as a function of $v=(M\Omega)^{1/3}$, where it is intended that $v=(M\Omega_{\rm NR})^{1/3}$ for NR, and $v=(M\Omega_{\rm EOB})^{1/3}$ for the EOB models, and we highlight with the triangle, square, and diamond where 3, 1, and 0 GW cycles before merger (taken as the peak of $|h_{22}|$) are. The SEOBNRv5 flux shows a better agreement, thanks to the additional PN information summarized in Sec. IVA and the calibration to 2GSF. As highlighted in Ref. [125], the latter seems to be the most significant source of improvement.

To quantify the improvement of the SEOBNRv5 model with respect to SEOBNRv4 across parameter space, we show in Fig. 15 the fractional difference between the Newtonian-normalized angular-momentum flux \hat{J} of SEOBNRv4 and SEOBNRv5, and the one obtained from the NR simulations described in Sec. V, evaluated two cycles before merger. The median fractional difference goes from 4.83% to 1.15%, and while the difference can be as high as 18% for the SEOBNRv4 model, it is always below 9% for the SEOBNRv5 model.

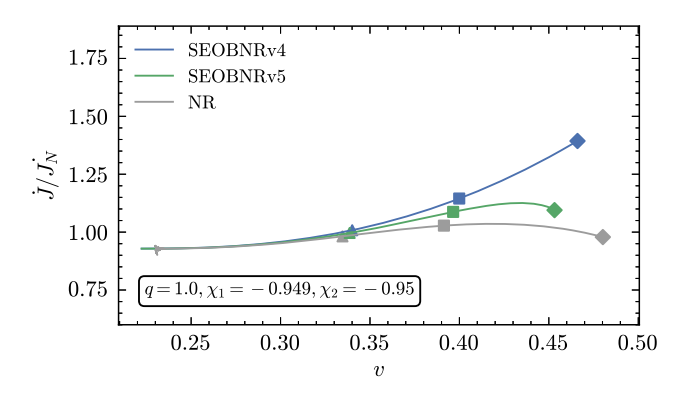


FIG. 14. Comparison of the Newtonian-normalized angular-momentum flux between SEOBNRv4, SEOBNRv5, and the NR simulation SXS:BBH:0156. The triangle, square, and diamond correspond, respectively, to 3, 1, and 0 GW cycles before merger, which is taken as the peak of the (2,2)-mode amplitude for each model.

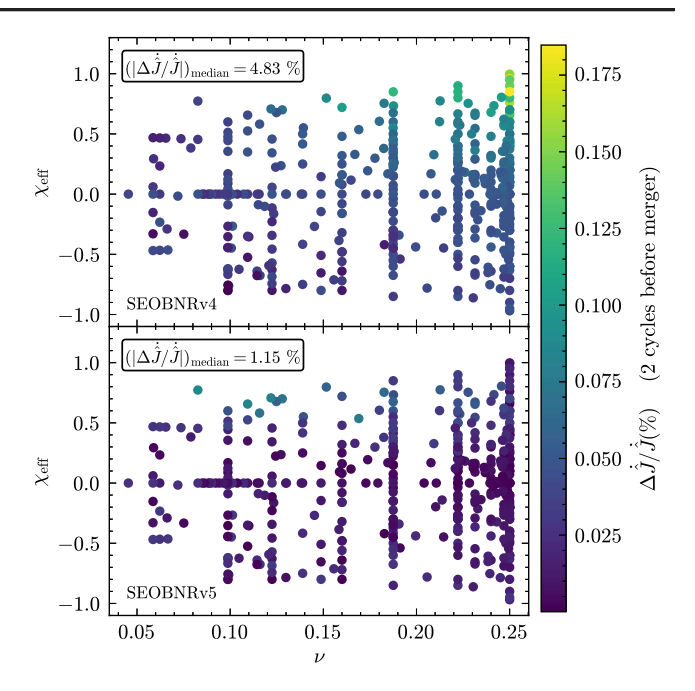


FIG. 15. Fractional difference between the Newtonian-normalized angular-momentum flux \hat{J} of SEOBNRv4 and SEOBNRv5, and the one obtained from the NR simulations used in this work, evaluated 2 cycles before merger.

The other comparison we consider is of the binding energy [195–197]. The NR binding energy data used here were obtained in Ref. [197], while the EOB binding energy is simply computed by evaluating

$$E_{\rm EOB}^{\rm bind} = H_{\rm EOB} - M,\tag{93}$$

along the EOB dynamics. Henceforth, to ease the notation, we will refer to $E_{\rm EOB}$ instead of $E_{\rm EOB}^{\rm bind}$. The EOB orbital frequency is obtained from $\Omega_{\rm EOB} = \partial H_{\rm EOB}/\partial p_{\phi}$, to be consistent with the gauge-invariant definition used for NR in Ref. [197].

In Fig. 16 we show the fractional difference between the NR binding energy for nonspinning configurations, and the one of SEOBNRv4 and SEOBNRv5, for different mass ratios. The gray region is an estimate of the NR error obtained from the q=1 data. Both EOB models show minor errors during most of the inspiral, and stay within the NR uncertainty until around 3 GW cycles before merger. The SEOBNRv5 model shows, however, a much better agreement in the late inspiral, between 3 and 1 cycles before merger, and remains within the error until $v \simeq 0.45$ for all mass ratios. As highlighted in Ref. [125], this improvement is mostly a consequence of the calibration to 2GSF results.

We now turn to aligned-spin cases, and as a starting point we compare different spin contributions to the binding energy, which can be extracted by combining results for various spin combinations as in Refs. [74,197,198]:

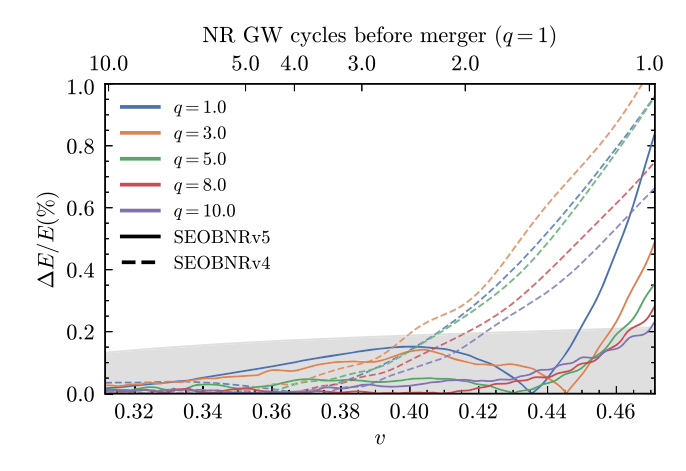


FIG. 16. Fractional difference between the EOB and NR nonspinning binding energy as a function of v, for SEOBNRv5 and SEOBNRv4. The gray region represents an estimate of the NR error. Notice the improvement in the agreement of SEOBNRv5 compared to SEOBNRv4, especially between 3 and 1 cycles before the merger.

$$E_{SO} = -\frac{1}{6}(-0.6, 0) + \frac{8}{3}(0.3, 0) - 2(0, 0) - \frac{1}{2}(0.6, 0), \quad (94a)$$

$$E_{S^2} = \frac{3}{2}(-0.6,0) - 2(0,0) + \frac{3}{2}(0.6,0) - (0.6,-0.6), \quad (94b)$$

$$E_{S^3} = -\frac{5}{6}(-0.6, 0) - \frac{8}{3}(0.3, 0) + 3(0, 0) - \frac{1}{2}(0.6, 0) + \frac{1}{2}(0.6, -0.6) + \frac{1}{2}(0.6, 0.6),$$
(94c)

where the numbers in brackets correspond to the dimensionless spins (χ_1,χ_2) of the BHs. The spin-squared contributions to the binding energy E_{S^2} refer to both S_i^2 and S_1S_2 interactions, and similarly the spin-cubic contributions E_{S^3} refer to both S_i^3 and $S_i^2S_j$. Among these contributions the spin-orbit term dominates throughout the inspiral, while the quadratic and cubic-in-spin terms have comparable magnitudes, with the quadratic terms growing larger close to the merger.

We begin by considering the spin-orbit effects. In Fig. 17 we compare the NR data to SEOBNRv4 and SEOBNRv5. In both cases, we consider calibrated and uncalibrated models, where by uncalibrated we mean that we set to zero all calibration parameters entering the Hamiltonian (the values of $\Delta t_{\rm ISCO}^{22}$ or $\Delta t_{\rm peak}^{22}$, on the other hand, do not affect these comparisons, as they only determine the time at which the merger-ringdown waveform modes are attached). SEOBNRv5 has a better agreement with NR compared to SEOBNRv4, and remains within the NR error almost until the merger. Moreover, the calibrated SEOBNRv5 model performs better than the uncalibrated model during the entire inspiral, whereas in SEOBNRv4 the calibration degrades the agreement after $v \simeq 0.45$.

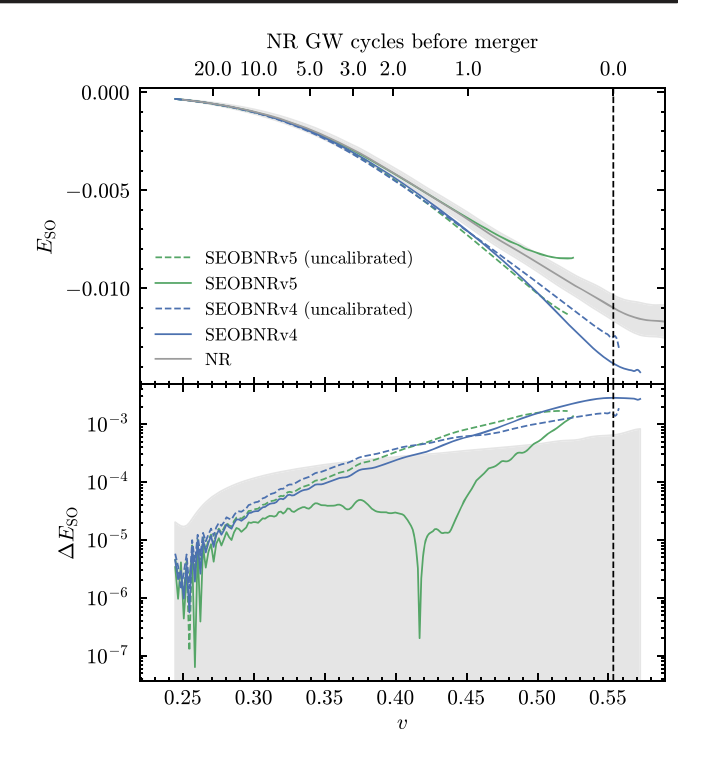


FIG. 17. Spin-orbit contribution to the binding energy as a function of v for SEOBNRv4 (blue), SEOBNRv5 (green), and NR (gray). The uncalibrated models are obtained by setting to zero the calibration parameters entering the Hamiltonian. The dashed vertical line represents the merger of the NR configuration in Eq. (94a) that merges at the lowest frequency, and the numbers of cycles also refer to the same simulation, while the EOB curves terminate at the EOB merger. The shaded regions represent the NR error. SEOBNRv5 has a better agreement with NR compared to SEOBNRv4, and remains within the NR error almost until the merger.

The results for the spin-spin term are shown in the left panel of Fig. 18: again, SEOBNRv5 clearly outperforms SEOBNRv4, and has differences compatible with the NR uncertainty almost up to the merger. An interesting difference is that, while uncalibrated SEOBNRv4 has a smaller difference with NR compared to the calibrated model, the same trend is not present in SEOBNRv5. This shows that the calibration of the model, which focuses on producing accurate waveforms, is not guaranteed to provide a better description of the conservative dynamics in the strong-field regime. A possible reason for this difference might be the additional presence of a spin-spin calibration parameter d_{SS} in SEOBNRv4, breaking the symmetry underlying the extraction of the terms used here. It is also possible that, due to degeneracies between changes in the dissipative and conservative dynamics, the less accurate flux of SEOBNRv4 is compensated for by the calibration of the Hamiltonian, and results in an overall worse agreement of the conservative dynamics with NR.

We consider cubic-in-spin contributions to the binding energy in the right panel of Fig. 18. These effects are minor,

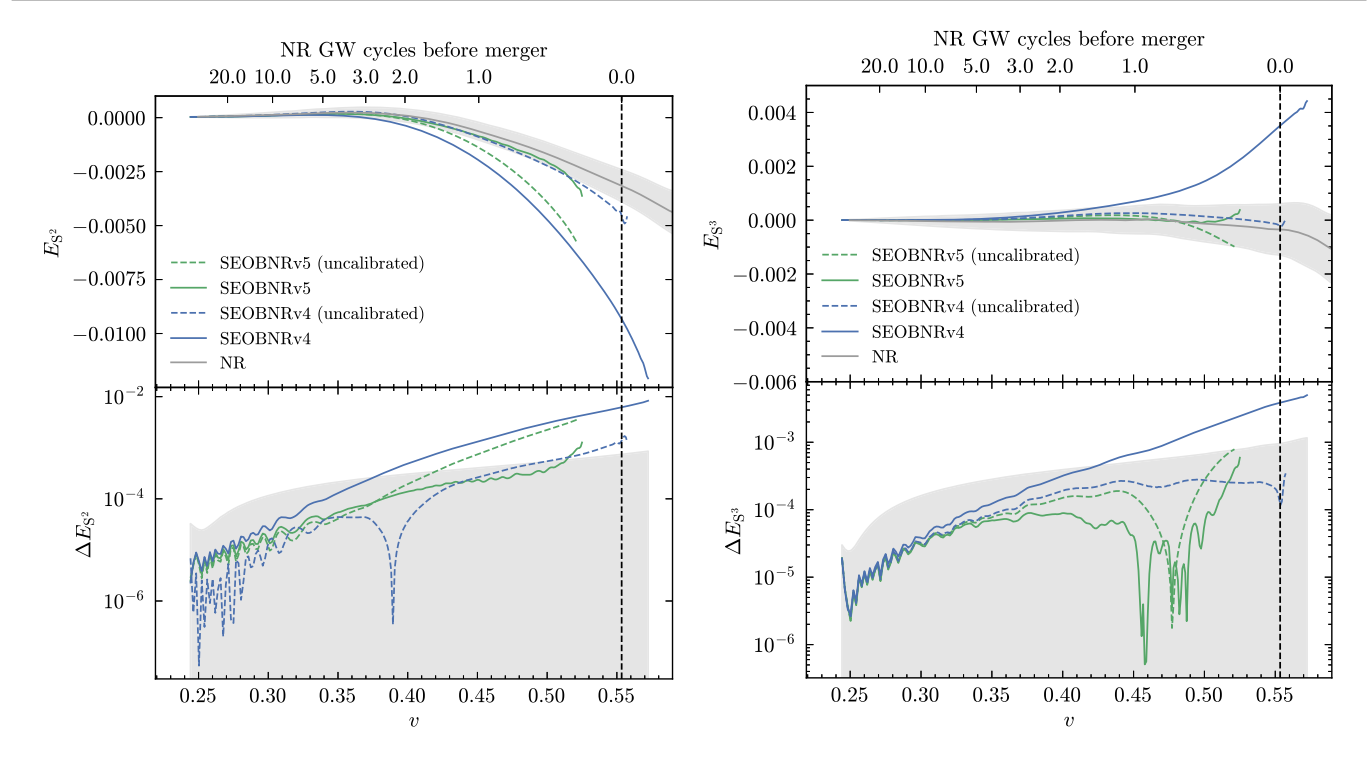


FIG. 18. Same as Fig 17, but for spin-spin contributions (left panel) and for cubic-in-spin contributions (right panel).

and contribute little to the overall disagreement; however one can see similarly to the spin-squared contributions that for SEOBNRv4 the calibration worsens the agreement with NR, making it the only model that does not stay within the NR error.

We finally quantify the improvement across parameter space by computing the fractional energy difference in the binding energy $|E_{EOB} - E_{NR}|/E_{NR}$ at a fixed frequency $v = \sqrt{0.2} \approx 0.45$ for several configurations. Constructing the binding energy curves is not a straightforward process, as one needs to take into account a shift of the curves due to the presence of junk radiation in NR waveforms; therefore we only focus on the simulations examined in Ref. [197]. In Fig. 19 we show such a comparison for the SEOBNRv4 and SEOBNRv5 models. In the first case the difference in the binding energy can reach more than 2.5%, especially for large values of the effective spin $\chi_{\rm eff}$, while for SEOBNRv5 we always find deviations from the NR binding energy at the subpercent level. The median relative difference is also considerably smaller, going from 1.15% for SEOBNRv4 to only 0.16% for the SEOBNRv5 model.

As highlighted in Ref. [125], an improved modeling of the binding energy and angular momentum flux does not necessarily correspond to a higher faithfulness of the waveforms in the regime where they are calibrated to NR, due to a significant degeneracy between the calibration terms in the EOB Hamiltonian and changes in the RR force. Nevertheless, achieving a more accurate representation of both the conservative and dissipative dynamics improves the overall consistency and naturalness of the model.

This reduces the model's reliance on NR calibration and provides greater confidence that SEOBNRv5 will maintain a certain faithfulness to NR when extrapolated beyond its calibration region, in particular for higher mass ratios.

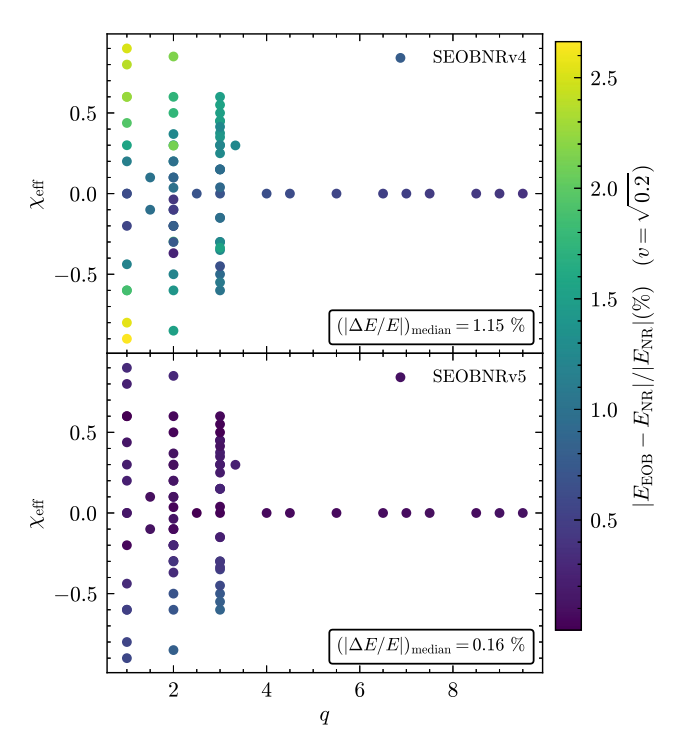


FIG. 19. Fractional difference between the EOB and NR binding energy, for SEOBNRv5 and SEOBNRv4, at $v = \sqrt{0.2} \approx 0.45$.

E. Computational performance

The fifth generation of SEOBNR models, starting from SEOBNRy5HM, is implemented in pySEOBNR, a Python package for developing and using waveform models within the SEOBNR framework. As described in Ref. [144], pySEOBNR offers a simple, object-oriented interface for building, calibrating, deploying, and profiling waveform models in both the time and frequency domain. The pySEOBNR package moves the development core of the SEOBNR framework from the previously used C-based LALSuite [199] to a much more flexible, modern and widely used Python infrastructure, setting a new standard for developing waveform models for current and future GW detectors. The user interface is implemented in pure Python, to facilitate ease of use and quick adoption by other researchers. The backend of the package relies on wellknown, regularly maintained packages under open-software licenses, including Cython [200] and NUMBA [201] for fast Hamiltonian evaluation and waveform generation, and NUMEXPR [202] for efficient NumPy [203] vectorized operations.

In this section we discuss the computational performance of the SEOBNRv5HM implementation in pySEOBNR, in terms of walltime for generating a waveform, and compare the model to other time-domain aligned-spin approximants that include higher modes, SEOBNRv4HM, with and without PA approximation, TEOBResumS-GIOTTO, which also employs the PA approximation, and IMRPhenomTHM.

Figure 20 shows the walltime for generating a waveform in the time domain, including interpolation on a constant time step, for total masses between 10 and $100M_{\odot}$, at starting frequency of 10 Hz, for three values of the mass ratio q=1, 3, 10 and spins $\chi_1=0.8, \chi_2=0.3$. For all approximants we include all modes up to $\ell=4$, and keep all other settings as default. We choose the sampling rate such that the Nyquist criterion is satisfied for the $\ell=4$ multipoles.⁸

Comparing the SEOBNRv5HM and SEOBNRv4HM models without the use of the PA approximation (dashed lines), we find a major performance improvement across all values of the total mass M. The speedup is most significant for lower total mass $(\sim50\times)$, and decreases for higher total mass to $\sim10\times$. The difference between SEOBNRv5HM and SEOBNRv4HM_PA, with the PA approximation being used in both cases (plotted in solid lines), is less drastic. Nonetheless, SEOBNRv5HM is consistently faster, despite including two additional modes. The speedup is up to $\sim70\%$ for low total-mass binaries. When using the PA approximation, a significant improvement in SEOBNRv5HM is the use of analytic

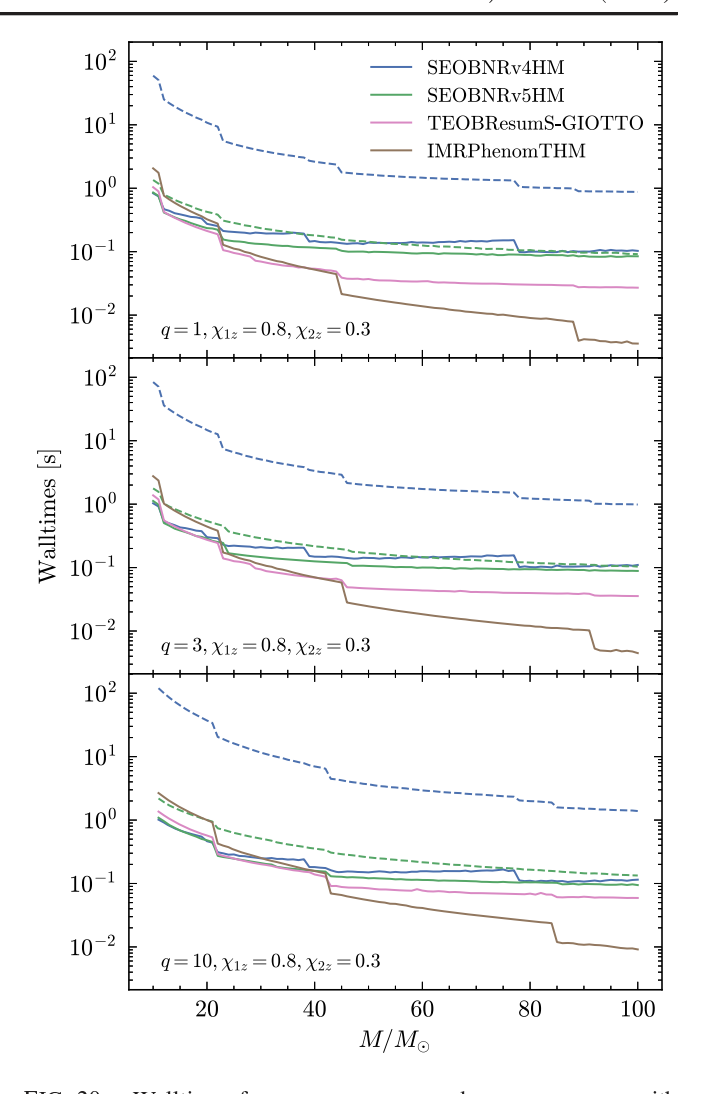


FIG. 20. Walltimes for SEOBNRv5HM and SEOBNRv4HM, with PA approximation (solid lines) and without (dashed lines), TEOBResumS-GIOTTO and IMRPhenomTHM, starting from $f_{\rm start}=10$ Hz, as a function of the total mass M. SEOBNRv5HM outperforms SEOBNRv4HM, particularly for low total mass systems, both with and without the PA approximation, and shows walltimes close to TEOBResumS-GIOTTO. IMRPhenomTHM is the fastest model for low total masses due to its use of closed-form expressions, with the gap narrowing for lower total masses. The analytic PA approximation and several optimizations, such as the use of analytic derivatives of the Hamiltonian, play a crucial role in the SEOBNRv5HM performance.

equations for the momenta [see Eqs. (19) and (20)], whereas these quantities are determined numerically in SEOBNRv4HM. We note that the difference between SEOBNRv4HM with and without the PA approximation is not limited to the use of the PA approximation, since SEOBNRv4HM_PA features several optimizations, such as the use of analytic derivatives of the Hamiltonian, which have also been implemented in the SEOBNRv5HM model independently of the use of the PA approximation. This is one of the reasons why the difference between

⁸All benchmarks were performed on the Hypatia computer cluster at the Max Planck Institute for Gravitational Physics in Potsdam, on a compute node equipped with a dual-socket 64-core AMD EPYC (Rome) 7742 CPU.

SEOBNRv5HM with and without PA is not as large as in the previous generation of SEOBNR models. It can reach up to \sim 2× for low total mass systems, while it is between 10% and 40% for $M \sim 100 M_{\odot}$, for cases where the cost of integrating the dynamics is less high. Comparing SEOBNRv5HM to a different EOB model, TEOBResumS-GIOTTO, employing in both cases the PA approximation, we see that TEOBResumS-GIOTTO is faster for high total-mass binaries, with a difference ranging from $\sim 3 \times$ for q = 1 to $\sim 1.5 \times$ for q = 10, while the two are comparable for low total masses. The time-domain phenomenological model IMRPhenomTHM outperforms all EOB models, for large total-mass systems, by over 1 order of magnitude. This is due to its use of fast closed-form expressions, rather than ordinary differential equation (ODE) integration. The gap between the models narrows as the total mass decreases, as the mode interpolation on a constant time step needed for the Fast-Fourier-Transform becomes a major cost for long inspirals (excluding SEOBNRv4HM without PA approximation, where ODE integration remains by far the main cost factor).

VII. PARAMETER-ESTIMATION STUDY

One of the most relevant applications of waveform models is to perform parameter inference for GW signals. Current parameter-estimation codes for inferring the properties of compact-binary coalescences are based on Bayesian inference, where the posterior probability distribution $P(\lambda|d|)$ for the parameters λ , given a signal d, is given by the Bayes theorem [204]

$$P(\lambda|d) = \frac{\pi(\lambda)\mathcal{L}(d|\lambda)}{Z},$$
(95)

where $\mathcal{L}(d|\lambda)$ is the likelihood of reproducing the data given a set of parameter values and a model for the signal, $\pi(\lambda)$ is the prior probability, and $Z = \int d\lambda \pi(\lambda) \mathcal{L}(d|\lambda)$ is the evidence of the model reproducing the data. The posterior distribution is stochastically sampled across the model parameter space, typically using nested sampling [182] or MCMC methods, which require from millions to hundreds of millions of waveform evaluations (see, e.g., Refs. [183,205,206]). Therefore, besides requiring that the waveform models accurately reproduce the data, it is also important that they are computationally efficient, to perform parameter estimation with reasonable resources and in a reasonable time. In this section we study the performance of SEOBNRv5HM for the recovery of parameters with a synthetic signal and three GW events observed during O1, O2, and O3.

A. Inference with a numerical-relativity synthetic signal

We begin by examining the parameter recovery on a synthetic signal injected in a network of three detectors, at the locations of LIGO Hanford, LIGO Livingston, and

TABLE III. Injected and median values of the posterior distributions for the synthetic NR injection, corresponding to the NR simulation SXS:BBH:q15Sur002 from the SXS Collaboration, recovered with IMRPhenomXHM and SEOBNRv5HM. The binary parameters correspond to the total mass M, chirp mass \mathcal{M} , individual masses $m_{1.2}$, inverse mass ratio 1/q, effective spin parameter $\chi_{\rm eff}$, individual spin components $\chi_{1z.2z}$, inclination angle ι , luminosity distance d_L , coalescence phase $\phi_{\rm ref}$, polarization angle ψ , right ascension α , declination δ , matched-filtered SNR for LIGO-Hanford/Livingston and Virgo detectors $\rho_{\rm mf}^{\rm H1,L1,V1}$, and signal-versus-noise log Bayes factor $\log \mathcal{BF}$.

| Parameter | Injected value | IMRPhenomXHM recovery | SEOBNRv5HM recovery |
|--------------------------|-------------------|--|------------------------------|
| $\overline{M/M_{\odot}}$ | 162.0 | 139.6 ^{+9.55} _{-10.93} | $160.58^{+11.57}_{-12.91}$ |
| \mathcal{M}/M_{\odot} | 29.53 | $29.65^{+1.46}_{-0.94}$ | $29.7^{+1.07}_{-0.9}$ |
| m_1/M_{\odot} | 151.88 | $128.09_{-11.81}^{+9.95}$ | $150.27^{+12.12}_{-13.64}$ |
| m_2/M_{\odot} | 10.13 | $11.54^{+1.26}_{-0.86}$ | $10.32^{+0.98}_{-0.78}$ |
| 1/q | 0.067 | $0.09^{+0.02}_{-0.01}$ | $0.07^{+0.01}_{-0.01}$ |
| $\chi_{ m eff}$ | 0.469 | $0.37^{+0.06}_{-0.07}$ | $0.47^{+0.05}_{-0.06}$ |
| χ_{1z} | 0.50 | $0.4^{+0.07}_{-0.07}$ | $0.5^{+0.05}_{-0.06}$ |
| χ_{2z} | 0.0 | $0.02^{+0.56}_{-0.49}$ | $0.03^{+0.59}_{-0.51}$ |
| ι/rad | 1.047 | $1.08^{+0.2}_{-0.23}$ | $0.98^{+0.2}_{-0.2}$ |
| $d_L/{ m Mpc}$ | 700.0 | $792.04^{+262.38}_{-222.3}$ | $798.97^{+198.04}_{-180.23}$ |
| $\phi_{ m ref}/{ m rad}$ | 0.80 | $3.57^{+1.98}_{-2.1}$ | $3.05^{+2.92}_{-2.73}$ |
| ψ /rad | 2.17 | $2.29^{+0.3}_{-0.28}$ | $2.33^{+0.22}_{-0.23}$ |
| α /rad | 3.81 | $3.84^{+0.09}_{-0.09}$ | $3.84^{+0.07}_{-0.07}$ |
| δ / rad | 0.63 | $0.6^{+0.09}_{-0.11}$ | $0.59^{+0.06}_{-0.09}$ |
| $ ho_{ m mf}^{ m H1}$ | 8.42 | $8.05^{+0.08}_{-0.15}$ | $8.26^{+0.07}_{-0.14}$ |
| $ ho_{ m mf}^{ m L1}$ | 9.98 | $9.54_{-0.17}^{+0.09}$ | $9.79^{+0.08}_{-0.17}$ |
| $ ho_{ m mf}^{ m V1}$ | 10.18 | $9.67^{+0.08}_{-0.16}$ | $9.98^{+0.08}_{-0.16}$ |
| $\log \mathcal{BF}$ | | 91.26 ± 0.20 | 97.53 ± 0.21 |

Virgo, with a zero-noise configuration, to decouple the impact of the model's accuracy from any particular noise realization. We inject the NR waveform SXS:BBH:2464 from the SXS Collaboration with intrinsic parameters $1/q = m_2/m_1 = 0.067$, $\chi_1 = 0.5$, and $\chi_2 = 0$, choosing a detector-frame total mass of $162M_{\odot}$, inclination $i = \pi/3$ in order to emphasize the higher harmonics of the signal, and a luminosity distance of 700 Mpc to give a network SNR of ~16.6. These and the selected injected values for the phase and the sky-location parameters are listed in the left column of Table III.

We employ the Bilby parameter-estimation code [184], with version 2.0.0 and the nested sampler DYNESTY [207] using the acceptance-walk method, which is well-suited for executing on a multicore machine; in particular, we run on 1 node of 64 CPUs. For the sampler settings for the recovery, we employ a number of accepted jumps during each MCMC chain naccept = 20 and a total number of live points nlive = 1000. We employ the sky parametrization option H1L1, which enables us to sample the sky position in azimuth and zenith, converted in

postprocessing to right ascension and declination, since this typically improves the convergence of the sampler, and we enable distance marginalization, to further improve convergence. We leave the rest of the sampler parameters with their default values.

The prior distributions are uniform for most of the parameters, except for the individual dimensionless spin values, which follow a distribution implied by the isotropic spin prior commonly employed in GW parameter estimation. Though a nonuniform prior could shift the posterior from the true values for moderate SNR in a zero-noise setup, we decide to employ this spin prior as it is commonly employed in actual analyses [2,4–6,208].

We perform two parameter estimation runs on this injected signal, one with the SEOBNRv5HM model presented in this paper, and a run with the state-of-the-art waveform model IMRPhenomXHM from the fourth generation of Fourier-domain phenomenological waveform models, to crosscheck the results. For SEOBNRv5HM, we employ the conditioning routine implemented in pySEOBNR, which closely mimics the procedure of LALSimulation [199].

The median recovered values for both models, and the 90% confidence intervals, are listed in Table III, and some relevant 2D contours are highlighted in Fig. 21. The results show that the SEOBNRv5HM model is able to recover better the synthetic signal, especially for the intrinsic parameters, with the injected value of all the parameters inside the 90% confidence intervals and very small deviations between the median values of the posterior distributions and the actual injected values (the main deviation is in the reference phase parameter, whose recovered distribution is prior dominated). On the contrary, the results inferred by the IMRPhenomXHM model contain important biases in most of the intrinsic parameters, with the injected values outside the 90% confidence intervals for the component masses, the total mass, the mass ratio, and the effective-spin parameter $\chi_{\rm eff}$. For the extrinsic parameters, both models recover the injected values within the 90% confidence intervals, with small but similar deviations in the median values for the distance and the inclination. The improved accuracy of SEOBNRv5HM in this challenging region of parameter space (high asymmetric masses and spinning primary black hole) is also reflected in the recovered matched-filter SNR in the three detectors and the Bayes factor of the inference run, which are consistently higher than the corresponding values for IMRPhenomXHM. These results are consistent with the fact that SEOBNRv5HM has lower unfaithfulness than IMRPhenomXHM against this NR simulation, 0.5% and 6.7% respectively, for the injected value of the total mass.

B. Inference of real gravitational-wave events

We then perform parameter estimation on three real GW events: GW150914 [1], the first detection which has become a benchmark for testing new waveform models;

GW170729 [209], an interesting event from O2, which has been analyzed with multimode waveform models; and GW190412 [210], the first confident mass-asymmetric binary reported during O2. For each event, we employ the strain data, detector calibration uncertainties, and PSD provided by the Gravitational Wave Open Science Center [211]. We perform the runs using Bilby [184] version 2.0.0 with the nested sampler DYNESTY [207], and we employ the same settings as in the previous section, except for the number of accepted jumps during each MCMC chain that we set to naccept = 60. For each GW signal, we perform a run with SEOBNRv5HM, employing the PA approximation, and a cross checking run with the IMRPhenomXHM waveform model.

In Fig. 22 we show some relevant 2D posterior distributions for the parameters, and observe good agreement between waveform models. These results are also consistent with the published results for the events, taking into account that LVK catalog results employ precessing-spin waveform models, and therefore minor differences are expected. The good agreement between the SEOBNRv5HM and IMRPhenomXHM posteriors is consistent with the fact that, for the events considered here, the recovered parameters are within the NR calibration region of both models. As in the case of the NR-injected signal, we observe a slight improvement in the matched-filter SNR and Bayes factor for SEOBNRv5HM with respect to IMRPhenomXHM, more pronounced for the two more massive events, as seen in Fig. 23. Although the improvement is not drastic, these results suggest that SEOBNRv5HM describes the data more accurately, which is consistent with the unfaithfulness results discussed in Sec. VI A.

In Table IV we report the real time spent on the inference for the parameters of these events for the waveform model SEOBNRv5HM. Employing Bilby on a single computing node (of 64 cores) requires less than a day for GW150914 and GW170729, and less than two days for GW190412, with a moderately low chirp mass. Therefore, the model is sufficiently efficient to be employed with the preferred parameter estimation pipeline by the LVK Collaboration.

VIII. FREQUENCY DOMAIN REDUCED-ORDER MODEL

The requirement of integrating a system of ODEs to solve for the dynamics of the binary in EOB models increases the time needed for generating a waveform. Surrogate or reduced-order modeling (ROM) techniques [21–25,100–102,104–106,109,212,213] have been applied in several contexts to accelerate slow waveform computation, in both EOB and NR models. These techniques involve decomposing the waveforms from a training set in orthonormal bases on sparse grids in time or frequency and then interpolating or fitting the resulting waveform data pieces over the binary parameter space. The result is a highly accurate, yet fast, method for generating waveforms for data analysis applications, which can

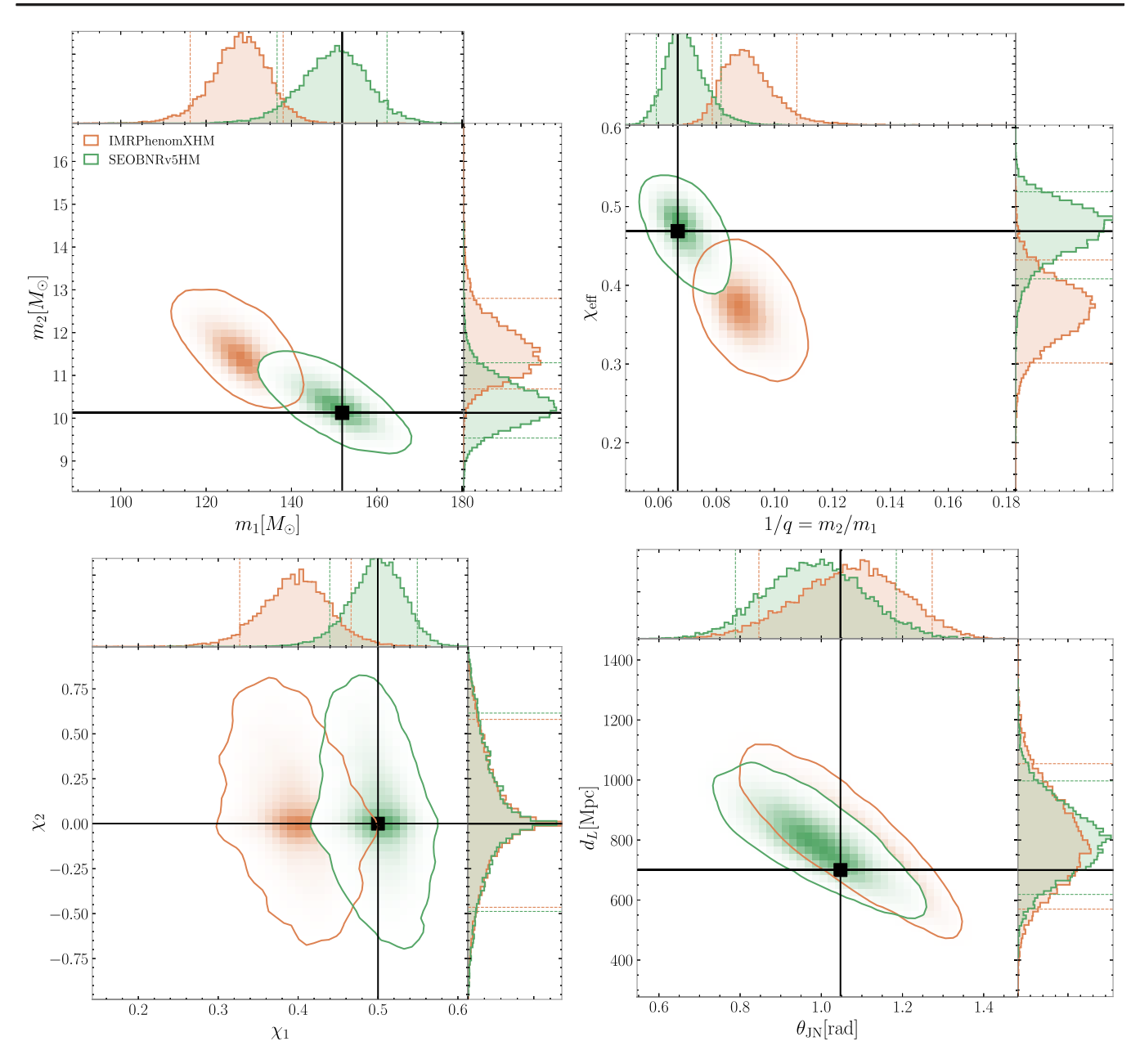


FIG. 21. 2D and 1D posterior distributions for some relevant parameters measured from the synthetic BBH signal with mass ratio q=15, total source-frame mass of $162M_{\odot}$, dimensionless spins $\chi_{1z}=0.5$, and $\chi_{2z}=0.0$. The inclination with respect to the line of sight of the binary is $\iota=\pi/3$ rad. The other parameters are specified in the text and in Table III. The injected signal is the SXS NR waveform SXS:BBH:2464. In the 2D posteriors the solid contours represent the 90% credible intervals and black dots show the values of the parameters of the injected signal. In the 1D posteriors they are represented by dashed and solid vertical lines, respectively. The parameter estimation is performed with the SEOBNRv5HM model (green) and the IMRPhenomXHM model (orange).

reduce computational time by orders of magnitude compared to ODE-based waveform models.

A frequency domain (FD) ROM of SEOBNRv4HM was built in Ref. [105], with modeling error introduced in building the ROM below the unfaithfulness of SEOBNRv4HM against NR simulations used to calibrate the model, and waveform evaluation times reduced by 2 orders of magnitude. In this section we show the performance of SEOBNRv5_ROM, a FD ROM of SEOBNRv5,

built following the same techniques of SEOBNRv4HM_ROM [101,102,105]. These mostly involve modeling in FD the phase of a carrier signal, based on the time-domain orbital phase, and the "co-orbital modes" obtained after extracting the carrier phasing from each FD mode. The co-orbital modes have an almost constant phase in the inspiral, and allow us to avoid zero crossings in the subdominant harmonics which would complicate the interpolation of the training data. As for SEOBNRv4HM_ROM, the

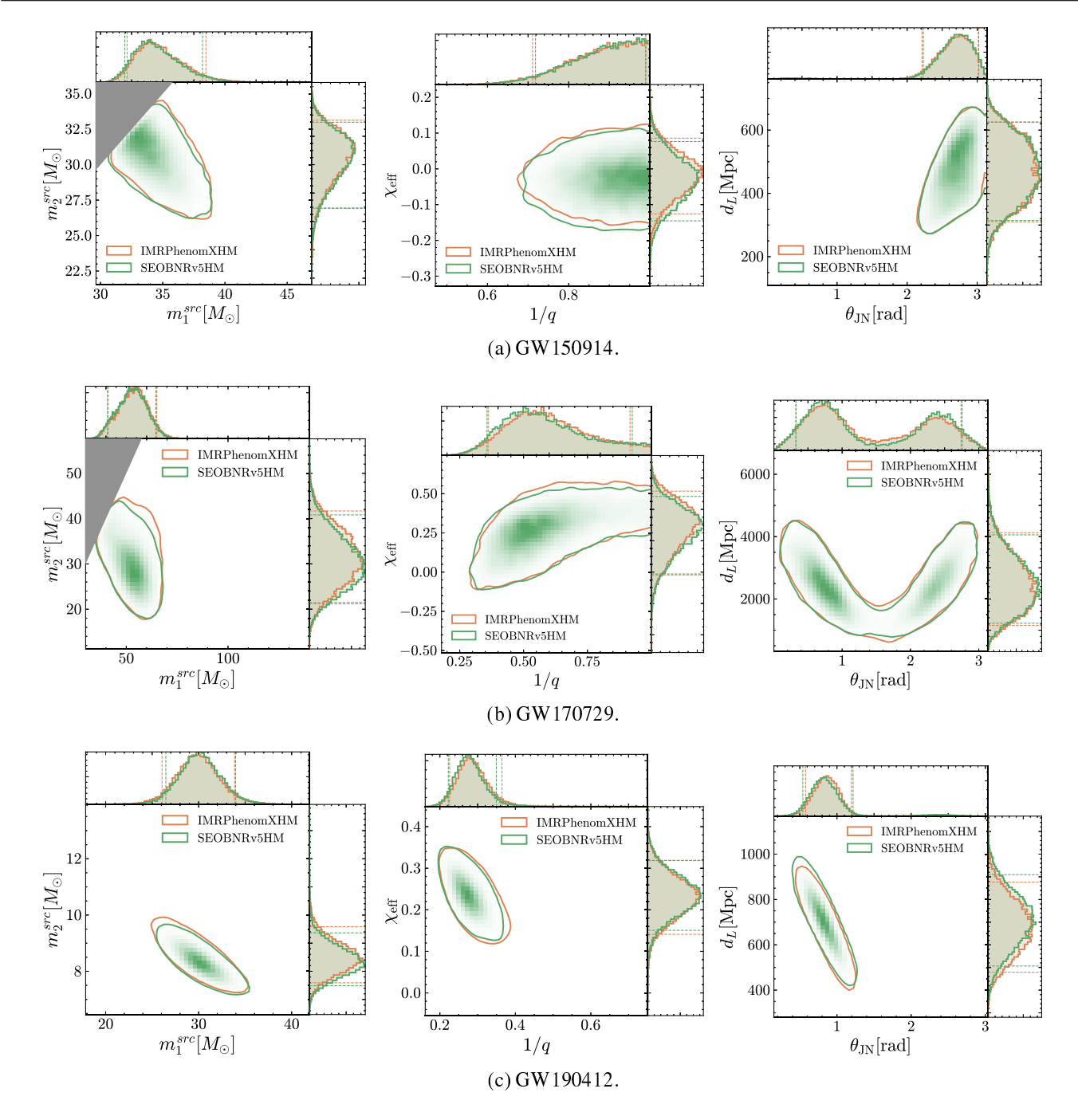


FIG. 22. 1D and 2D posterior distributions for several parameters for the GW events GW150914, GW170729, and GW190412.

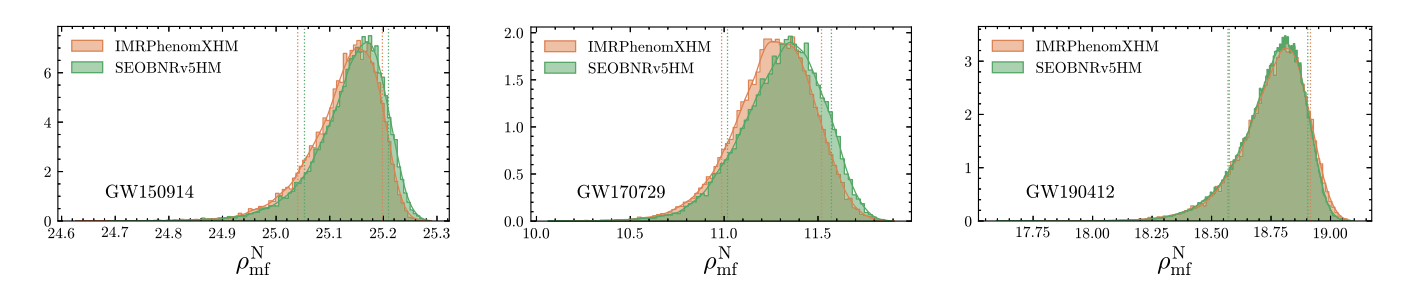


FIG. 23. Network matched-filter SNR recovered by IMRPhenomXHM and SEOBNRv5HM for the three analyzed GW events.

TABLE IV. Evaluation time for the different parameter estimation runs on real GW events with the SEOBNRv5HM model. The time reported is actual real time, while the total computational cost in CPU hours can be obtained by multiplying this time by the reported number of CPU cores employed.

| Run/event | GW150914 | GW170729 | GW190412 |
|-----------------------------|----------|----------|----------|
| SEOBNRv5HM Bilby (64 cores) | 23 h | 20 h | 1 d 18 h |

SEOBNRv5 ROM model combines a higher resolution high-frequency ROM, starting from 20 Hz for binaries with total mass of $50M_{\odot}$, and a lower resolution lowfrequency ROM, starting from 20 Hz for binaries with total mass of $5M_{\odot}$, and can be extended to arbitrarily low frequencies by hybridizing it with multipolar PN waveforms. SEOBNRv5 ROM can be generated for mass ratios between 1 and 100, dimensionless spins between [-0.998, 0.998], and includes only the dominant $(\ell, |m|) =$ (2, 2) mode. A multipolar reduced-order model of SEOBNRv5HM (SEOBNRv5HM ROM), including the $(\mathcal{E}, |m|) = (2, 2), (3, 3), (2, 1), (4, 4), (5, 5), (3, 2), (4, 3)$ modes, is also under development, and will be presented in near future work. Despite the speed of SEOBNRv5HM being sufficient for many GW data analysis applications, using a ROM can still lead to a significant increase in efficiency. Additionally, there are several applications for which it is desirable to be able to generate clean FD waveforms of any length.

In Fig. 24 we show a histogram of the unfaithfulness between SEOBNRv5_ROM and SEOBNRv5, for different values of the total mass, for 10^5 configurations with mass ratios between 1 and 100 and dimensionless spins between [-0.998, 0.998]. We observe an excellent agreement, with median values $\lesssim 10^{-5}$. The unfaithfulness increases with the total mass of the system, as in previous ROM

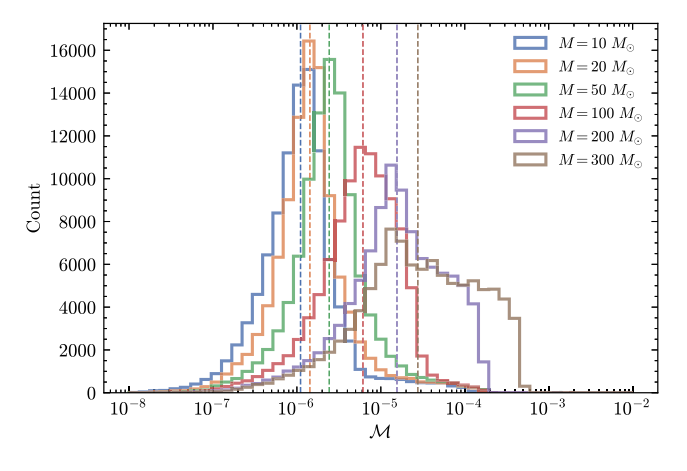


FIG. 24. Mismatch of SEOBNRv5_ROM against SEOBNRv5 for different values of the total mass, for 10^5 random configurations. The dashed vertical lines show the medians.

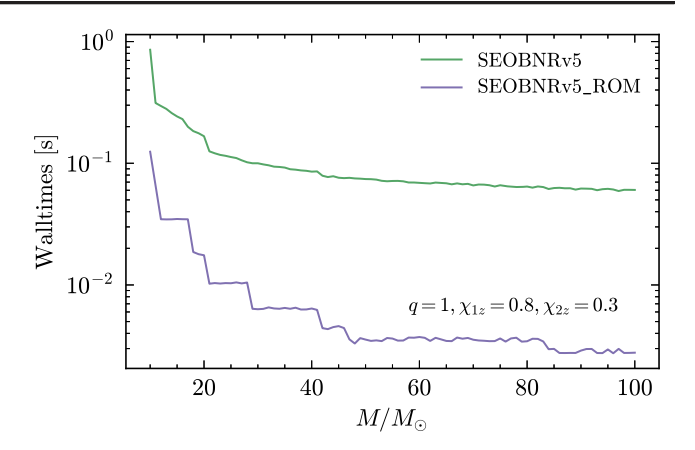


FIG. 25. Walltime comparison between SEOBNRv5 and SEOBNRv5_ROM, using a starting frequency $f_{\rm start} = 10$ Hz, as a function of the total mass M. For the time domain SEOBNRv5 model this also includes the conversion in the Fourier domain.

models [77,105], because the ROM modes are generated up to a maximum frequency that scales with the inverse of the total mass. In particular, the mismatch is larger for cases with high mass ratio and negative spins, as the maximum frequency of each mode is proportional to its least damped QNM frequency [105], which decreases in this region of the parameter space. Nonetheless, the modeling error introduced in the construction of the ROM is negligible compared to the inaccuracy of the SEOBNRv5 waveforms with respect to the NR simulations.

Figure 25 highlights the speedup of the ROM with respect to SEOBNRv5, by comparing walltimes of the two models for generating a FD waveform with the same parameters ($q=1,\chi_1=0.8,\chi_2=0.3$), as a function of the total mass M. For SEOBNRv5 we also employ the PA approximation. As for Fig. 20, we use a starting frequency $f_{\text{start}}=10$ Hz, and we choose the sampling rate for the time domain model such that the Nyquist criterion is satisfied for the $\ell=2$ multipoles. The FD SEOBNRv5_ROM model is instead generated up to a maximum frequency equal to the corresponding Nyquist frequency. Notably, we obtain an improvement from a factor ~ 7 for low total-mass binaries, to more than ~ 20 for $M \sim 100 M_{\odot}$. Overall, we can appreciate that SEOBNRv5_ROM can be generated in less than 10 ms for $M \gtrsim 20 M_{\odot}$.

IX. CONCLUSIONS

In this paper we have presented SEOBNRv5HM, a new EOBNR waveform model for quasicircular, spinning, non-precessing BBHs, which improves the previous generation, SEOBNRv4HM [78], on both speed and accuracy against NR simulations. The waveform model includes the modes $(\ell, |m|) = (2, 2), (3, 3), (2, 1), (4, 4), (5, 5), (3, 2), (4, 3),$ and models the mode mixing in the merger ringdown for the modes (3,2),(4,3), which were not included in SEOBNRv4HM.

Sections III and IV have outlined the building blocks of the waveform model. The aligned-spin SEOBNRv5 Hamiltonian is based on a deformation of the equatorial Kerr Hamiltonian, and includes most of the known 5PN nonspinning and full 4PN information for spinning binaries, with improved resummations [126]. The factorized waveform modes and RR force of SEOBNRv4HM have been enhanced by additional PN information (as well as corrections to some of the terms) from Ref. [127], and have been calibrated to 2GSF fluxes in the nonspinning limit in Ref. [125]. To improve the accuracy of the model in the inspiral, we have refined the calibration pipeline employed by Ref. [77], and largely upgraded its efficiency, in order to be able to tune the model to a large catalog of 442 NR simulations as shown in Sec. V. We have also improved the modeling of the merger and ringdown using the full NR dataset at our disposal, as well as 13 waveforms from BH perturbation theory.

In Sec. VI we compared SEOBNRv5HM and other stateof-the-art waveform approximants to NR simulations, using mismatch calculations. The results showed that the dominant (2,2) mode of SEOBNRv5 is, on average, more accurate than SEOBNRv4 [77] by 1 order of magnitude; it is more accurate than the other state-of-the-art EOB model, TEOBResumS-GIOTTO [64,83,113,114], by more than a factor of 2 and is overall comparable to the Fourierdomain phenomenological model IMRPhenomXAS [44]. By computing mismatches of the full polarizations at inclination $i = \pi/3$, we noted that all models become less accurate; nonetheless SEOBNRv5HM outperforms both SEOBNRv4HM [78] and TEOBResumS-GIOTTO, as well as the phenomenological model IMRPhenomXHM [46], both considering average values and the number of cases above 0.01. We have validated the model against the NR surrogate models NRHybSur3dq8 [24] and NRHybSur2dq15 [30] and found results consistent with the NR comparison, demonstrating the robustness of our calibration procedure. Further tests of the calibration pipeline are described in Appendix E. In particular, we show that the accuracy of the model against the entire NR dataset of 442 waveforms does not change appreciably when using only 137 to calibrate the model. This confirms that the significant improvement over SEOBNRv4 is largely due to the improved analytical prescriptions, particularly for the EOB Hamiltonian, but even if not all NR data are used directly, they remain extremely valuable for a detailed assessment of the effectiveness of different analytical choices. Direct use of the new NR data is particularly useful when considering high mass ratio, high spin configurations in the region of parameter space previously uncovered by simulations, and in modeling higher modes in the merger-ringdown phase, which benefits greatly from simulations with higher resolution. We also show that our calibration pipeline is robust with respect to changes in the shape of the PSD used, as the unfaithfulness of the model against NR remains very similar when using a white noise curve, the Einsten Telescope [214], and Cosmic Explorer [16] PSDs. Nonetheless, such a comparison is limited by the length of the available NR simulations, which do not cover the entire bandwidth of next-generation GW detectors, and more detailed studies will be needed to assess the accuracy of SEOBNRv5HM in such a context. Comparing SEOBNRv5HM and IMRPhenomXHM against each other in a larger parameter space, we have seen instead that the mismatches can become very large in the region where both models are not calibrated to NR waveforms, in particular for both high mass ratio, say ≥ 5 , and high positive spin, say ≥ 0.8 , configurations. Thus, producing new NR simulations for these parameters would be critical to reduce modeling systematics. Comparing the angularmomentum flux and binding energy of SEOBNRv5 and SEOBNRv4 against NR, we have highlighted a similar improvement, also thanks to the 2GSF information [125], despite the fact that these quantities do not directly enter the calibration. This is a powerful check of the physical robustness of the model, and provides confidence in its reliability when extrapolating outside of the NR calibration region. We have implemented SEOBNRv5HM in a flexible, high-performance, Python package pySEOBNR, and we have shown that the model is fast enough for typical GW data-analysis applications: it is more than 10 times faster than SEOBNRv4HM without using the PA approximation, up to 2 times faster than SEOBNRv4HM PA when using it, and overall close to TEOBResumS-GIOTTO.

In Sec. VII we have demonstrated that the model can be reliably used for GW parameter estimation, by performing a recovery on a NR injection, and by analyzing three events observed by LIGO and Virgo, GW150914, GW170729, and GW190412. For the three events, we have found consistent results when comparing the parameters recovered by SEOBNRv5HM and by IMRPhenomXHM, while still observing a slight improvement in matched-filter SNR and Bayes factor for SEOBNRv5HM with respect to IMRPhenomXHM. On the other hand, the NR injection in a challenging region of parameter space (high asymmetric masses and spinning primary black hole) shows more significant differences. SEOBNRv5HM accurately recovers all the binary parameters, while the results inferred by the IMRPhenomXHM model contain biases in most of the intrinsic parameters due to larger modeling errors. The use of waveform models that include both higher modes and spin-precession is now the standard in GW parameter estimation [4-6]. SEOBNRv5HM would still be useful, for example, to study evidence for spin precession, by analyzing the data including or not this effect in the model, and in tests of general relativity (GR), in which the additional computational cost of accounting for beyond-GR parameters often makes it convenient to employ a simpler and more efficient aligned-spin model [215-219].

In Sec. VIII we have finally shown the performance of a FD ROM model (SEOBNRv5_ROM) developed following the techniques used in Ref. [105], which allows for a significant speedup in evaluation time, while retaining identical accuracy against NR. Matched filter GW searches often use FD aligned-spin models such as SEOBNRv4_ROM [2,4–6], and SEOBNRv5_ROM could be a valuable replacement for such applications.

The pySEOBNR code infrastructure [144] is a framework developed with the goal of facilitating the development of future SEOBNR waveform models, and upcoming work would naturally revolve around adding more physical effects to the SEOBNRv5 family, as well as improving its efficiency and accuracy by including ever more information from both NR simulations and different analytical frameworks. The first extension of SEOBNRv5HM, as far as additional physical effects are concerned, involves modeling spin precession, and such a model (SEOBNRv5PHM) has been developed in parallel to this work in Ref. [145].

An upcoming extension would also involve eccentric and hyperbolic orbits (SEOBNRv5EHM), following similar strategies adopted in the SEOBNRv4EHM model of Ref. [91]. The more efficient, flexible, and parallelized calibration pipeline described in this work would allow for having a more accurate eccentric model, with a consistent treatment of eccentric corrections in the waveform modes and RR force, after appropriately recalibrating the quasicircular limit of the model. Moreover, the efficiency of SEOBNRv5HM compared to SEOBNRv4HM without PA approximation, which is slow to use when adding eccentricity, means that one could expect a significant speedup of SEOBNRv5EHM compared to SEOBNRv4EHM. Further ongoing developments in the SEOBNRv5 family involve the modeling of tidal effects, already incorporated in SEOBNRv4 models [94,95,98,104], and the addition of parametrized GR deviations to perform theory agnostic tests of GR [217-219].

Another direction for improvements revolves around pushing the accuracy of the model against NR even further. Exploring different ways to incorporate and resum information from the PN, Post-Minkowskian, and 2GSF approximations, while still retaining flexibility in the calibration, would be crucial, and an efficient calibration code (pySEOBNR [144]) is essential to understand the impact of different modeling and resummation choices. At the same time, more and better NR simulations, especially in currently unexplored regions of the binary parameter space, are also critical to reach the accuracy requirements of nextgeneration detectors [181,220]. A limitation of all state-ofthe-art approximants is the modeling of the higher modes, and a straightforward improvement to be done in future work would be to add all terms through 3.5PN to the waveform modes and RR force from Refs. [127,164]. Further work should also go into improving the modeling of the higher modes through the merger and ringdown, as well as including additional modes. Finally, a calibration pipeline similar to the one developed here could be used to calibrate SEOBNRv5PHM [145] to spin-precessing NR simulations.

SEOBNRv5_ROM is publicly available through LALSuite [199].

ACKNOWLEDGMENTS

It is our pleasure to thank Geraint Pratten, Stanislav Babak, Alice Bonino, Eleanor Hamilton, N. V. Krishnendu, Piero Rettegno, Riccardo Sturani, and Jooheon Yoo for performing the LIGO-Virgo-KAGRA review of the SEOBNRv5 models. Part of M. K.'s work on this paper is supported by the Perimeter Institute for Theoretical Physics. Research at Perimeter Institute is supported in part by the Government of Canada through the Department of Innovation, Science and Economic Development and by the Province of Ontario through the Ministry of Colleges and Universities. M. v. d. M. is supported by VILLUM FONDEN (Grant No. 37766), and the Danish Research Foundation. R. C. is supported by NSF Grants No. AST-2006538, No. PHY-2207502, No. PHY-090003, and No. PHY-20043, and NASA Grants No. 19-ATP19-0051, No. 20-LPS20-0011, and No. 21-ATP21-0010. H. R. is supported by the Fundação para a Ciência e Tecnologia (FCT) within the Projects No. UID/04564/2021, No. UIDB/ 04564/2020, No. UIDP/04564/2020, and No. EXPL/FIS-AST/0735/2021. This work was supported in part by the Sherman Fairchild Foundation, by NSF Grants No. PHY-2011961, No. PHY-2011968, and No. OAC-1931266 at Caltech; by NSF Grants No. PHY-1912081, No. PHY-2207342, No. OAC-1931280, and No. OAC-2209655 at Cornell; by NSF Awards No. AST-1559694 and No. PHY-1654359; by Nicholas and Lee Begovich; and by the Dan Black Family Trust. The computational work for this manuscript was carried out on the Hypatia computer cluster at the Max Planck Institute for Gravitational Physics in Potsdam. SEOBNRv5HM is publicly available through the Python package pySEOBNR [221]. Stable versions of pySEOBNR are published through the Python Package Index (PyPI), and can be installed via pip install pyseobnr. This research has made use of data or software obtained from the Gravitational Wave Open Science Center ([222]), a service of LIGO Laboratory, the LIGO Scientific Collaboration, the Virgo Collaboration, and KAGRA. LIGO Laboratory and Advanced LIGO are funded by the United States National Science Foundation (NSF) as well as the Science and Technology Facilities Council (STFC) of the United Kingdom, the Max-Planck-Society (MPS), and the State of Niedersachsen/Germany for support of the construction of Advanced LIGO and construction and operation of the GEO600 detector. Additional support for Advanced LIGO was provided by the Australian Research Council. Virgo is funded, through the European Gravitational Observatory (EGO), by the French Centre National de Recherche Scientifique (CNRS), the Italian Istituto Nazionale di Fisica Nucleare (INFN) and the Dutch Nikhef, with contributions by institutions from Belgium, Germany, Greece, Hungary, Ireland, Japan, Monaco, Poland, Portugal, and Spain. KAGRA. is supported by the Ministry of Education, Culture, Sports, Science and Technology (MEXT), Japan Society for the Promotion of Science (JSPS) in Japan; the National Research Foundation (NRF) and Ministry of Science and ICT (MSIT) in Korea; and Academia Sinica (AS) and the National Science and Technology Council (NSTC) in Taiwan.

APPENDIX A: HAMILTONIAN COEFFICIENTS

We summarize here results that were derived in Ref. [126]. In the nonspinning limit, the Hamiltonian is given by Eq. (6). The 5PN-expanded \bar{D}_{noS} , which enters the Hamiltonian through Eq. (8), is given by [149,150]

$$\begin{split} \bar{D}_{\text{noS}}^{\text{Tay}}(u) &= 1 + 6\nu u^2 + (52\nu - 6\nu^2)u^3 + \left[\nu\left(-\frac{533}{45} - \frac{23761\pi^2}{1536} + \frac{1184\gamma_E}{15} - \frac{6496\ln 2}{15} + \frac{2916\ln 3}{5}\right) \right. \\ &\quad + \left(\frac{123\pi^2}{16} - 260\right)\nu^2 + \frac{592\nu}{15}\ln u\right]u^4 + \left(-\frac{3392\nu^2}{15} - \frac{1420\nu}{7}\right)u^5\ln u \\ &\quad + \left[\nu\left(\frac{294464}{175} - \frac{2840\gamma_E}{7} - \frac{63707\pi^2}{512} + \frac{120648\ln 2}{35} - \frac{19683\ln 3}{7}\right) + \left(\frac{1069}{3} - \frac{205\pi^2}{16}\right)\nu^3 \right. \\ &\quad + \left(d_5^{\nu^2} - \frac{6784\gamma_E}{15} + \frac{67736}{105} + \frac{58320\ln 3}{7} - \frac{326656\ln 2}{21}\right)\nu^2\right]u^5, \end{split} \tag{A1}$$

where we set the remaining unknown coefficient $d_5^{\nu^2}$ to zero. To improve agreement with NR, we perform a (2,3) Padé resummation of $\bar{D}_{\rm noS}^{\rm Tay}(u)$.

For Q_{noS} , we use the full 5.5PN expansion derived in Refs. [150,223], which is expanded in eccentricity to $\mathcal{O}(p_r^8)$. Instead of using p_r , we write Q_{noS} in terms of p_{r_*} using Eq. (8), then PN expand to 5.5PN order, leading to

$$\begin{split} Q_{\text{noS}} &= \frac{p_{r_*}^4}{\mu^2} \left\{ 2(4-3\nu)\nu u^2 + u^3 \left[10\nu^3 - 131\nu^2 + \nu \left(-\frac{4348}{15} + \frac{496256\ln 2}{45} - \frac{33048\ln 3}{5} \right) \right] + u^4 \left[\left(792 - \frac{615\pi^2}{32} \right) \nu^3 \right. \\ &\quad + \nu^2 \left(-\frac{592\ln u}{5} + \frac{31633\pi^2}{512} - \frac{1184\gamma_E}{512} + \frac{45683}{105} + \frac{33693536\ln 2}{105} - \frac{6396489\ln 3}{70} - \frac{9765625\ln 5}{126} \right) \\ &\quad + \nu \left(\frac{5428\ln u}{105} + \frac{1249177}{1050} - \frac{93031\pi^2}{1536} + \frac{10856\gamma_E}{105} - \frac{4396376}{105} \ln 2 + \frac{9765625\ln 5}{504} - \frac{601911\ln 3}{280} \right) \right] + \frac{88703\pi\nu u^{9/2}}{1890} \right\} \\ &\quad + \frac{p_{r_*}^6}{\mu^4} \left\{ u^2 \left[6\nu^3 - \frac{27\nu^2}{5} + \nu \left(-\frac{827}{3} - \frac{1}{25}2358912\ln 2 + \frac{1399437\ln 3}{50} + \frac{390625\ln 5}{18} \right) \right] \right. \\ &\quad + u^3 \left[-14\nu^4 + 188\nu^3 + \nu^2 \left(\frac{154229}{75} - \frac{4998308864\ln 2}{1575} + \frac{26171875\ln 5}{18} - \frac{45409167\ln 3}{350} \right) \right. \\ &\quad + \nu \left(-\frac{860317}{1050} + \frac{305146624\ln 2}{945} + \frac{35643726\ln 3}{175} - \frac{52468750\ln 5}{189} \right) \right] - \frac{2723471\pi\nu u^{7/2}}{756000} \right\} \\ &\quad + \frac{p_{r_*}^8}{\mu^6} \left\{ u\nu \left[-\frac{35772}{175} + \frac{21668992\ln 2}{45} + \frac{6591861\ln 3}{350} - \frac{27734375\ln 5}{126} \right] + \frac{5994461\pi\nu u^{5/2}}{12700800} + u^2 \left[-6\nu^4 + \frac{24\nu^3}{7} + \nu^2 \left(\frac{870976}{525} + \frac{703189497728\ln 2}{33075} + \frac{332067403089\ln 3}{39200} - \frac{13841287201\ln 7}{4320} - \frac{468490234375\ln 5}{42336} \right) \right. \\ &\quad + \nu \left(-\frac{2222547}{2450} - \frac{1347019456}{525} \ln 2 + \frac{278690984375\ln 5}{169344} + \frac{13841287201\ln 7}{17280} - \frac{346536085761\ln 3}{156800} \right) \right] \right\}. \tag{A2}$$

In the aligned-spin Hamiltonian, the 3.5PN SO gyrogravitomagnetic factors in Eq. (12) are given by

$$g_{a_{+}}^{3.5\text{PN}} = \frac{7}{4} + \left[\tilde{L}^{2} u^{2} \left(-\frac{45\nu}{32} - \frac{15}{32} \right) + u \left(\frac{23\nu}{32} - \frac{3}{32} \right) \right] + \left[\tilde{L}^{4} u^{4} \left(\frac{345\nu^{2}}{256} + \frac{75\nu}{128} + \frac{105}{256} \right) + \tilde{L}^{2} u^{3} \left(-\frac{1591\nu^{2}}{768} - \frac{267\nu}{128} + \frac{59}{256} \right) + u^{2} \left(\frac{109\nu^{2}}{192} - \frac{177\nu}{32} - \frac{5}{64} \right) \right], \tag{A3a}$$

$$g_{a_{-}}^{3.5\text{PN}} = \frac{1}{4} + \left[\tilde{L}^{2} u^{2} \left(\frac{15}{32} - \frac{9\nu}{32} \right) + u \left(\frac{11\nu}{32} + \frac{3}{32} \right) \right] + \left[\tilde{L}^{4} u^{4} \left(\frac{75\nu^{2}}{256} - \frac{45\nu}{128} - \frac{105}{256} \right) + \tilde{L}^{2} u^{3} \left(-\frac{613\nu^{2}}{768} - \frac{35\nu}{128} - \frac{59}{256} \right) + u^{2} \left(\frac{103\nu^{2}}{192} - \frac{\nu}{32} + \frac{5}{64} \right) \right], \tag{A3b}$$

where the square brackets collect different PN orders, and we defined $\tilde{L} \equiv L/(M\mu) \equiv p_{\phi}/(M\mu)$. The cubic-in-spin term G_{σ^3} reads as

$$G_{a^3}^{\text{align}} = \frac{Mp_{\phi}}{4r^2} (\delta a_- a_+^2 - a_+^3). \tag{A4}$$

The potentials in the even-in-spin part of the effective Hamiltonian in Eq. (12) include the 4PN SS information, and are given by

$$A^{\text{align}} = \frac{a_+^2/r^2 + A_{\text{noS}} + A_{\text{SS}}^{\text{align}}}{1 + (1 + 2M/r)a_+^2/r^2},$$
(A5a)

$$B_{np}^{\text{align}} = -1 + \frac{a_+^2}{r^2} + A_{\text{noS}} \bar{D}_{\text{noS}} + B_{np,SS}^{\text{align}},$$
 (A5b)

$$B_{npa}^{\text{Kerr eq}} = -\frac{1 + 2M/r}{r^2 + a^2(1 + 2M/r)},$$
 (A5c)

$$Q^{\text{align}} = Q_{\text{noS}} + Q_{\text{SS}}^{\text{align}},\tag{A5d}$$

where

$$A_{\rm SS}^{\rm ali\,gn} = \frac{M^2}{r^4} \left[\frac{9a_+^2}{8} - \frac{5}{4} \delta a_- a_+ + a_-^2 \left(\frac{\nu}{2} + \frac{1}{8} \right) \right] + \frac{M^3}{r^5} \left[a_+^2 \left(-\frac{175\nu}{64} - \frac{225}{64} \right) + \delta a_- a_+ \left(\frac{117}{32} - \frac{39\nu}{16} \right) \right] + a_-^2 \left(\frac{21\nu^2}{16} - \frac{81\nu}{64} - \frac{9}{64} \right) \right], \tag{A6a}$$

$$B_{np,SS}^{\text{align}} = \frac{M}{r^3} \left[a_+^2 \left(3\nu + \frac{45}{16} \right) - \frac{21}{8} \delta a_- a_+ + a_-^2 \left(\frac{3\nu}{4} - \frac{3}{16} \right) \right] + \frac{M^2}{r^4} \left[a_+^2 \left(-\frac{1171\nu}{64} - \frac{861}{64} \right) + \delta a_- a_+ \left(\frac{13\nu}{16} + \frac{449}{32} \right) + a_-^2 \left(\frac{\nu^2}{16} + \frac{115\nu}{64} - \frac{37}{64} \right) \right], \tag{A6b}$$

$$Q_{\text{SS}}^{\text{align}} = \frac{Mp_r^4}{\mu^2 r^3} \left[a_+^2 \left(\frac{25}{32} - 5\nu^2 + \frac{165\nu}{32} \right) + \delta a_- a_+ \left(\frac{45\nu}{8} - \frac{5}{16} \right) + a_-^2 \left(-\frac{15\nu^2}{8} + \frac{75\nu}{32} - \frac{15}{32} \right) \right]. \tag{A6c}$$

APPENDIX B: EXPRESSIONS FOR THE FACTORIZED WAVEFORM MODES

In this appendix, we list the expressions for $\rho_{\ell m}$, $f_{\ell m}$, and $\delta_{\ell m}$, which are used in the factorized modes [see Eqs. (25) and (34)].

In the (2,2) mode, ρ_{22} and δ_{22} are given by

$$\begin{split} \rho_{22} &= 1 + v_{\Omega}^2 \left(\frac{55}{84} \nu - \frac{43}{42} \right) + v_{\Omega}^3 \left[\left(\frac{2}{3} \nu - \frac{2}{3} \right) \chi_S - \frac{2}{3} \delta \chi_A \right] + v_{\Omega}^4 \left[\frac{19583}{42336} \nu^2 - \frac{33025}{10584} \nu - \frac{20555}{10584} + \left(\frac{1}{2} - 2 \nu \right) \chi_A^2 + \delta \chi_A \chi_S + \frac{1}{2} \chi_S^2 \right] \\ &+ v_{\Omega}^5 \left[\delta \left(-\frac{19}{42} \nu - \frac{34}{21} \right) \chi_A + \left(\frac{209}{126} \nu^2 + \frac{49}{18} \nu - \frac{34}{21} \right) \chi_S \right] + v_{\Omega}^6 \left[\frac{10620745 \nu^3}{39118464} - \frac{6292061 \nu^2}{3259872} + \frac{41 \pi^2 \nu}{192} - \frac{48993925 \nu}{9779616} \right] \\ &- \frac{428}{105} \, \text{eulerlog}(2, v_{\Omega}) + \frac{1556919113}{122245200} + \delta \left(\frac{89}{126} - \frac{781}{252} \nu \right) \chi_A \chi_S + \left(-\frac{27}{14} \nu^2 - \frac{457}{504} \nu + \frac{89}{252} \right) \chi_A^2 \\ &+ \left(\frac{10}{9} \nu^2 - \frac{1817}{504} \nu + \frac{89}{252} \right) \chi_S^2 \right] + v_{\Omega}^7 \left[\delta \left(\frac{97865}{63504} \nu^2 + \frac{50140}{3969} \nu + \frac{18733}{15876} \right) \chi_A \\ &+ \left(\frac{50803}{63504} \nu^3 - \frac{245717}{63504} \nu^2 + \frac{74749}{5292} \nu + \frac{18733}{15876} \right) \chi_S + \delta \chi_A^3 \left(\frac{1}{3} - \frac{4}{3} \nu \right) + \delta (2\nu + 1) \chi_A \chi_S^2 \\ &+ (-4\nu^2 - 3\nu + 1) \chi_A^2 \chi_S + \left(\nu + \frac{1}{3} \right) \chi_S^3 \right] + v_{\Omega}^8 \left[\frac{9202}{2205} \, \text{eulerlog}(2, v_{\Omega}) - \frac{387216563023}{160190110080} \right] \\ &+ v_{\Omega}^{10} \left[\frac{439877}{55566} \, \text{eulerlog}(2, v_{\Omega}) - \frac{16094530514677}{533967033600} \right], \end{split}$$

$$\delta_{22} = \frac{7}{3}\Omega H_{EOB} + (\Omega H_{EOB})^2 \left[\left(\frac{8}{3}\nu - \frac{4}{3} \right) \chi_S - \frac{4}{3}\delta \chi_A + \frac{428}{105}\pi \right] + (\Omega H_{EOB})^3 \left[\frac{1712}{315}\pi^2 - \frac{2203}{81} \right] - 24\nu v_{\Omega}^5, \tag{B1b}$$

where eulerlog (m, v_{Ω}) is defined by Eq. (47). The coefficient 19/42 of $\mathcal{O}(v_{\Omega}^5 \delta \chi_A \nu)$ in ρ_{22} corrects a typo in the SEOBNRv4 code, and we added in ρ_{22} the NLO spin-squared and LO spin-cubed contributions, which are given by Eq. (4.11a) of Ref. [127].

The (2,1) mode reads as

$$\begin{split} \rho_{21}^{\text{NS}} &= 1 + v_{\Omega}^2 \left(\frac{23}{84} \nu - \frac{59}{56} \right) + v_{\Omega}^4 \left(\frac{617}{4704} \nu^2 - \frac{10993}{14112} \nu - \frac{47009}{56448} \right) + v_{\Omega}^6 \left[\frac{7613184941}{2607897600} - \frac{107}{105} \text{eulerlog}(1, v_{\Omega}) \right] \\ &+ v_{\Omega}^8 \left[-\frac{1168617463883}{911303737344} + \frac{6313}{5880} \text{eulerlog}(1, v_{\Omega}) \right] + v_{\Omega}^{10} \left[-\frac{63735873771463}{16569158860800} + \frac{5029963}{5927040} \text{eulerlog}(1, v_{\Omega}) \right], \end{split} \tag{B2a}$$

$$\begin{split} f_{21}^{\mathrm{S}} &= -\frac{3}{2} v_{\Omega} \left(\frac{\chi_{A}}{\delta} + \chi_{S} \right) + v_{\Omega}^{3} \left[\left(\frac{131}{84} \nu + \frac{61}{12} \right) \frac{\chi_{A}}{\delta} + \left(\frac{79}{84} \nu + \frac{61}{12} \right) \chi_{S} \right] + v_{\Omega}^{4} \left[(-2\nu - 3)\chi_{A}^{2} + \left(\frac{21}{2} \nu - 6 \right) \frac{\chi_{A}\chi_{S}}{\delta} + \left(\frac{1}{2} \nu - 3 \right) \chi_{S}^{2} \right] \\ &+ v_{\Omega}^{5} \left[\left(-\frac{703}{112} \nu^{2} + \frac{8797}{1008} \nu - \frac{81}{16} \right) \frac{\chi_{A}}{\delta} + \left(\frac{613}{1008} \nu^{2} + \frac{1709}{1008} \nu - \frac{81}{16} \right) \chi_{S} + \left(\frac{3}{4} - 3\nu \right) \frac{\chi_{A}^{3}}{\delta} + \left(\frac{9}{4} - 6\nu \right) \frac{\chi_{A}\chi_{S}^{2}}{\delta} \right. \\ &+ \left. \left(\frac{9}{4} - 3\nu \right) \chi_{A}^{2}\chi_{S} + \frac{3}{4}\chi_{S}^{3} \right] + v_{\Omega}^{6} \left[\left(\frac{5}{7} \nu^{2} - \frac{9287}{1008} \nu + \frac{4163}{252} \right) \chi_{A}^{2} + \left(\frac{139}{72} \nu^{2} - \frac{2633}{1008} \nu + \frac{4163}{252} \right) \chi_{S}^{2} \right. \\ &+ \left. \left(\frac{9487}{504} \nu^{2} - \frac{1636}{21} \nu + \frac{4163}{126} \right) \frac{\chi_{A}\chi_{S}}{\delta} \right], \end{split} \tag{B2b}$$

$$\delta_{21} = \frac{2}{3}\Omega H_{\text{EOB}} + \frac{107}{105}\pi(\Omega H_{\text{EOB}})^2 + \left(\frac{214}{315}\pi^2 - \frac{272}{81}\right)(\Omega H_{\text{EOB}})^3 - \frac{25}{2}\nu v_{\Omega}^5,\tag{B2c}$$

where the $\mathcal{O}(v_{\Omega}^6\chi^2\nu^2)$ terms in $f_{21}^{\rm S}$ correct those used in the SEOBNRv4HM model [78]. We also fixed the coefficient -25/2 of $\mathcal{O}(\nu v_{\Omega}^5)$ in δ_{21} , which was the result of an error in Ref. [163], which was later corrected in an erratum, as noted in Ref. [127].

The (3,3) mode is given by

$$\rho_{33}^{NS} = 1 + v_{\Omega}^{2} \left(\frac{2}{3} \nu - \frac{7}{6} \right) + v_{\Omega}^{4} \left(-\frac{6719}{3960} - \frac{1861}{990} \nu + \frac{149}{330} \nu^{2} \right)$$

$$+ v_{\Omega}^{6} \left[\frac{3203101567}{227026800} + \left(-\frac{129509}{25740} + \frac{41\pi^{2}}{192} \right) \nu - \frac{274621}{154440} \nu^{2} + \frac{12011}{46332} \nu^{3} - \frac{26}{7} \text{ eulerlog}(3, v_{\Omega}) \right]$$

$$+ v_{\Omega}^{8} \left[-\frac{57566572157}{8562153600} + \frac{13}{3} \text{ eulerlog}(3, v_{\Omega}) \right] + v_{\Omega}^{10} \left[-\frac{903823148417327}{30566888352000} + \frac{87347}{13860} \text{ eulerlog}(3, v_{\Omega}) \right], \qquad (B3a)$$

$$f_{33}^{S} = v_{\Omega}^{3} \left[\left(\frac{19}{2} \nu - 2 \right) \frac{\chi_{A}}{\delta} + \left(\frac{5}{2} \nu - 2 \right) \chi_{S} \right] + v_{\Omega}^{4} \left[\left(\frac{3}{2} - 6\nu \right) \chi_{A}^{2} + (3 - 12\nu) \frac{\chi_{A}\chi_{S}}{\delta} + \frac{3}{2}\chi_{S}^{2} \right]$$

$$+ v_{\Omega}^{5} \left[\left(\frac{407}{30} \nu^{2} - \frac{593}{60} \nu + \frac{2}{3} \right) \frac{\chi_{A}}{\delta} + \left(\frac{241}{30} \nu^{2} + \frac{11}{20} \nu + \frac{2}{3} \right) \chi_{S} \right]$$

$$+ v_{\Omega}^{6} \left[\left(-12\nu^{2} + \frac{11}{2} \nu - \frac{7}{4} \right) \chi_{A}^{2} + \left(44\nu^{2} - \nu - \frac{7}{2} \right) \frac{\chi_{A}\chi_{S}}{\delta} + \left(6\nu^{2} - \frac{27}{2} \nu - \frac{7}{4} \right) \chi_{S}^{2} \right]$$

$$+ i(\Omega H_{EOB})^{2} \left[\left(\frac{7339}{540} \nu - \frac{81}{20} \right) \frac{\chi_{A}}{\delta} + \left(\frac{593}{108} \nu - \frac{81}{20} \right) \chi_{S} \right], \qquad (B3b)$$

$$\delta_{33} = \frac{13}{10} \left(H_{EOB} \Omega \right) + \frac{39\pi}{7} \left(H_{EOB} \Omega \right)^{2} + \left(-\frac{227827}{3000} + \frac{78\pi^{2}}{7} \right) \left(H_{EOB} \Omega \right)^{3} - \frac{80897}{2430} \nu v_{\Omega}^{5}, \qquad (B3c)$$

where the imaginary part of f_{33}^S is included in δ_{33} in Ref. [127], but we moved it to f_{33}^S to facilitate the implementation in the equal-mass limit, for which we pull the factor δ from the leading order h_{33}^N into $f_{\ell m}$ to cancel the divergent $1/\delta$. For the (4,4) mode, we use

$$\begin{split} \rho_{44} &= 1 + v_{\Omega}^2 \left[\frac{1614 - 5870\nu + 2625\nu^2}{1320(-1+3\nu)} \right] + v_{\Omega}^3 \left[\left(\frac{2}{3} - \frac{41\nu}{15} + \frac{14\nu^2}{5} \right) \frac{1}{(-1+3\nu)} \chi_S + \delta \left(\frac{2}{3} - \frac{13\nu}{5} \right) \frac{1}{(-1+3\nu)} \chi_A \right] \\ &+ v_{\Omega}^4 \left[- \frac{14210377}{8808800(1-3\nu)^2} + \frac{32485357\nu}{4404400(1-3\nu)^2} - \frac{1401149\nu^2}{1415700(1-3\nu)^2} - \frac{801565\nu^3}{37752(1-3\nu)^2} + \frac{3976393\nu^4}{1006720(1-3\nu)^2} \right. \\ &+ \frac{1}{2} \chi_A^2 - 2\nu \chi_A^2 + \delta \chi_A \chi_S + \frac{1}{2} \chi_S^2 \right] + v_{\Omega}^5 \left[\left(-\frac{69}{55} + \frac{16571\nu}{1650} - \frac{2673\nu^2}{100} + \frac{8539\nu^3}{440} + \frac{591\nu^4}{44} \right) \frac{1}{(1-3\nu)^2} \chi_S \right. \\ &+ \delta \left(-\frac{69}{55} + \frac{10679\nu}{1650} - \frac{1933\nu^2}{220} + \frac{597\nu^3}{440} \right) \frac{1}{(1-3\nu)^2} \chi_A \right] + v_{\Omega}^6 \left[\frac{16600939332793}{1098809712000} - \frac{12568}{3465} \text{ eulerlog}(4, \nu_{\Omega}) \right] \\ &+ v_{\Omega}^8 \left[-\frac{172066910136202271}{19426955708160000} + \frac{845198}{190575} \text{ eulerlog}(4, \nu_{\Omega}) \right] + v_{\Omega}^{10} \left[-\frac{17154485653213713419357}{568432724020761600000} \right] \\ &+ \frac{22324502267}{3815311500} \text{ eulerlog}(4, \nu_{\Omega}) \right], \end{split}$$

$$\delta_{44} = \frac{(112 + 219\nu)}{120(1 - 3\nu)} (\Omega H_{EOB}) + \frac{25136\pi}{3465} (\Omega H_{EOB})^2 + \left(\frac{201088}{10395}\pi^2 - \frac{55144}{375}\right) (\Omega H_{EOB})^3, \tag{B4b}$$

and for the (5,5) mode,

$$\begin{split} \rho_{55}^{\rm NS} &= 1 + v_{\Omega}^2 \left[\frac{487}{390(-1+2\nu)} - \frac{649\nu}{195(-1+2\nu)} + \frac{256\nu^2}{195(-1+2\nu)} \right] - \frac{3353747}{2129400} v_{\Omega}^4 \\ &+ v_{\Omega}^6 \left[\frac{190606537999247}{11957879934000} - \frac{1546}{429} \mathrm{eulerlog}(5, v_{\Omega}) \right] + v_{\Omega}^8 \left[-\frac{1213641959949291437}{118143853747920000} + \frac{376451}{83655} \mathrm{eulerlog}(5, v_{\Omega}) \right] \\ &+ v_{\Omega}^{10} \left[-\frac{150082616449726042201261}{4837990810977324000000} + \frac{2592446431}{456756300} \mathrm{eulerlog}(5, v_{\Omega}) \right], \end{split} \tag{B5a}$$

$$f_{55}^{S} = v_{\Omega}^{3} \left[\left(-\frac{70\nu}{3(-1+2\nu)} + \frac{110\nu^{2}}{3(-1+2\nu)} + \frac{10}{3(-1+2\nu)} \right) \frac{\chi_{A}}{\delta} + \left(\frac{10}{3(-1+2\nu)} - \frac{10\nu}{-1+2\nu} + \frac{10\nu^{2}}{-1+2\nu} \right) \chi_{S} \right] + v_{\Omega}^{4} \left[\left(-\frac{5}{2} + 5\nu \right) \frac{1}{(-1+2\nu)} \chi_{S}^{2} + (-5+30\nu-40\nu^{2}) \frac{1}{(-1+2\nu)} \frac{\chi_{S}\chi_{A}}{\delta} + \left(-\frac{5}{2} + 15\nu - 20\nu^{2} \right) \frac{1}{(-1+2\nu)} \chi_{A}^{2} \right], \quad (B5b)$$

$$\delta_{55} = \frac{(96875 + 857528\nu)}{131250(1 - 2\nu)} (\Omega H_{EOB}) + \frac{3865\pi}{429} (\Omega H_{EOB})^2 + \frac{-7686949127 + 954500400\pi^2}{31783752} (\Omega H_{EOB})^3, \tag{B5c}$$

which are both the same as in SEOBNRv4HM [78].

The (3,2) mode is given by

$$\begin{split} \rho_{32} &= 1 + v_{\Omega} \frac{4\nu\chi_{S}}{3(1-3\nu)} + v_{\Omega}^{2} \left[\frac{\frac{32}{7}\nu^{2} + \frac{223}{58}\nu - \frac{164}{135}}{1-3\nu} - \frac{16\nu^{2}\chi_{S}^{2}}{9(1-3\nu)^{2}} \right] + v_{\Omega}^{3} \left[\left(\frac{13}{9}\nu + \frac{2}{9} \right) \frac{\delta\chi_{A}}{1-3\nu} \right. \\ &\quad + \left(\frac{607}{81}\nu^{3} + \frac{503}{81}\nu^{2} - \frac{1478}{405}\nu + \frac{2}{9} \right) \frac{\chi_{S}}{(1-3\nu)^{2}} + \frac{320\nu^{3}\chi_{S}^{3}}{81(1-3\nu)^{3}} \right] + v_{\Omega}^{4} \left[\frac{77141}{40095}\nu^{4} - \frac{508474}{40095}\nu^{3} - \frac{945121}{320760}\nu^{2} + \frac{1610009\nu}{320760}\nu - \frac{180566}{200475} \right. \\ &\quad + \left(4\nu^{2} - 3\nu + \frac{1}{3} \right) \frac{\chi_{A}^{2}}{1-3\nu} + \left(-\frac{50}{27}\nu^{2} - \frac{88}{27}\nu + \frac{2}{3} \right) \frac{\delta\chi_{A}\chi_{S}}{(1-3\nu)^{2}} + \left(-\frac{2452}{243}\nu^{4} - \frac{1997}{243}\nu^{3} + \frac{1435}{243}\nu^{2} - \frac{43}{27}\nu + \frac{1}{3} \right) \frac{\chi_{S}^{2}}{(1-3\nu)^{3}} \right] \\ &\quad + v_{\Omega}^{5} \left[\left(-\frac{1184225}{96228}\nu^{5} - \frac{40204523}{962280}\nu^{4} + \frac{101706029}{962280}\nu^{3} - \frac{14103833}{192456}\nu^{2} + \frac{20471053}{962280}\nu - \frac{2788}{1215} \right) \frac{\chi_{S}}{(1-3\nu)^{3}} \right. \\ &\quad + \left(\frac{608}{81}\nu^{3} + \frac{736}{81}\nu^{2} - \frac{16}{9}\nu \right) \frac{\delta\chi_{A}\chi_{S}^{2}}{(1-3\nu)^{3}} + \left(\frac{889673}{106920}\nu^{3} - \frac{75737}{5346}\nu^{2} + \frac{376177}{35640}\nu - \frac{2788}{1215} \right) \frac{\delta\chi_{A}}{(1-3\nu)^{2}} \\ &\quad + \left(\frac{96176}{2187}\nu^{5} + \frac{43528}{2187}\nu^{4} - \frac{40232}{2187}\nu^{3} + \frac{376}{81}\nu^{2} - \frac{8\nu}{9} \right) \frac{\chi_{S}^{3}}{(1-3\nu)^{4}} + \left(-\frac{32}{3}\nu^{3} + 8\nu^{2} - \frac{8}{9}\nu \right) \frac{\chi_{A}^{2}\chi_{S}}{(1-3\nu)^{2}} \right] \\ &\quad + v_{\Omega}^{6} \left[\frac{5849948554}{940355325} - \frac{104 \text{ eulerlog}(2, v_{\Omega})}{63} \right] + v_{\Omega}^{8} \left[\frac{17056 \text{ eulerlog}(2, v_{\Omega})}{8505} - \frac{10607269449358}{3072140846775} \right] \\ &\quad + v_{\Omega}^{10} \left[-\frac{1312549797426453052}{176264081083715625} + \frac{18778864 \text{ eulerlog}(2, v_{\Omega})}{12629925} \right], \end{split}$$

$$\delta_{32} = \left(\frac{11}{5}\nu + \frac{2}{3}\right) \frac{\Omega H_{\text{EOB}}}{1 - 3\nu} + \frac{52}{21}\pi (\Omega H_{\text{EOB}})^2 + \left(\frac{208}{63}\pi^2 - \frac{9112}{405}\right) (\Omega H_{\text{EOB}})^3, \tag{B6b}$$

where we added all spin contributions beyond the LO spin orbit in ρ_{32} , as well as the test-mass limit terms given in Eq. (46a).

The (4,3) mode is given by

$$\begin{split} \rho_{43}^{\rm NS} &= 1 + \frac{v_{\Omega}^2}{1-2\nu} \left(-\frac{10}{11} \nu^2 + \frac{547}{176} \nu - \frac{111}{88} \right) - \frac{6894273}{7047040} v_{\Omega}^4 + v_{\Omega}^6 \left[\frac{1664224207351}{195343948800} - \frac{1571}{770} \, \text{eulerlog}(3, v_{\Omega}) \right] \\ &+ v_{\Omega}^8 \left[-\frac{2465107182496333}{460490801971200} + \frac{174381}{67760} \, \text{eulerlog}(3, v_{\Omega}) \right] \end{split} \tag{B7a}$$

$$f_{43}^{S} = \frac{v_{\Omega}}{1 - 2\nu} \left(\frac{5}{2} \nu \chi_{S} - \frac{5}{2} \nu \frac{\chi_{A}}{\delta} \right) + \frac{v_{\Omega}^{3}}{1 - 2\nu} \left[\left(\frac{887}{44} \nu - \frac{3143}{132} \nu^{2} \right) \frac{\chi_{A}}{\delta} + \left(-\frac{529}{132} \nu^{2} - \frac{667}{44} \nu \right) \chi_{S} \right] + \frac{v_{\Omega}^{4}}{1 - 2\nu} \left[\left(12\nu^{2} - \frac{37}{3}\nu + \frac{3}{2} \right) \chi_{A}^{2} + \left(\frac{137}{6} \nu^{2} - 18\nu + 3 \right) \frac{\chi_{A}\chi_{S}}{\delta} + \left(\frac{35}{6} \nu^{2} + \frac{1}{3}\nu + \frac{3}{2} \right) \chi_{S}^{2} \right],$$
 (B7b)

$$\delta_{43} = \left(\frac{4961}{810}\nu + \frac{3}{5}\right) \frac{\Omega H_{\text{EOB}}}{1 - 2\nu} + \frac{1571}{385}\pi (\Omega H_{\text{EOB}})^2,\tag{B7c}$$

where we added all spin contributions beyond the LO spin orbit in $f_{43}^{\rm S}$, and the test-mass limit terms of Eq. (46b) in $\rho_{43}^{\rm NS}$.

(B25)

All other modes, which are used in the RR force in Eq. (16), are the same as in SEOBNRv4HM. They are written in Refs. [75,159], but we also list them here for completeness:

$$\begin{split} \rho_{31}^{\rm NS} &= 1 - v_{\Omega}^2 \left[\frac{2}{9} \nu + \frac{13}{18} \right] + v_{\Omega}^4 \left[-\frac{829}{1782} \nu^2 - \frac{1685}{1782} \nu + \frac{101}{7128} \right] + v_{\Omega}^6 \left[\frac{11706720301}{6129723600} - \frac{26}{63} \, \text{eulerlog}(1, v_{\Omega}) \right] \\ &+ v_{\Omega}^8 \left[\frac{169}{567} \, \text{eulerlog}(1, v_{\Omega}) + \frac{2606097992581}{4854741091200} \right], \end{split} \tag{B8}$$

$$f_{31}^{S} = v_{\Omega}^{3} \left[\left(\frac{11}{2} \nu - 2 \right) \frac{\chi_{A}}{\delta} + \left(\frac{13}{2} \nu - 2 \right) \chi_{S} \right], \tag{B9}$$

$$\delta_{31} = \frac{13}{30} \Omega H_{\text{EOB}} + \frac{13}{21} \pi (\Omega H_{\text{EOB}})^2 + \left(\frac{26}{63} \pi^2 - \frac{227827}{81000}\right) (\Omega H_{\text{EOB}})^3, \tag{B10}$$

$$\rho_{42} = 1 + \frac{285\nu^2 - 3530\nu + 1146}{1320(3\nu - 1)} v_{\Omega}^2 - \frac{v_{\Omega}^3}{15(1 - 3\nu)} [(78\nu^2 - 59\nu + 10)\chi_S + (10 - 21\nu)\delta\chi_A]$$

$$+ \frac{-379526805\nu^4 - 3047981160\nu^3 + 1204388696\nu^2 + 295834536\nu - 114859044}{317116800(1 - 3\nu)^2} v_{\Omega}^4$$

$$+ \left[\frac{848238724511}{219761942400} - \frac{3142}{3465} \text{eulerlog}(2, v_{\Omega}) \right] v_{\Omega}^6,$$
(B11)

$$\delta_{42} = \left(\frac{7}{15} + \frac{14}{5}\nu\right) \frac{\Omega H_{\text{EOB}}}{1 - 3\nu} + \frac{6284}{3465}\pi (\Omega H_{\text{EOB}})^2,\tag{B12}$$

$$\rho_{41}^{\rm NS} = 1 + \frac{288\nu^2 - 1385\nu + 602}{528(2\nu - 1)}v_{\Omega}^2 - \frac{7775491}{21141120}v_{\Omega}^4 + \left[\frac{1227423222031}{1758095539200} - \frac{1571}{6930} {\rm eulerlog}(1, v_{\Omega})\right]v_{\Omega}^6, \tag{B13}$$

$$f_{41}^{\rm S} = \frac{5}{2} \nu \frac{v_{\Omega}}{1 - 2\nu} \left(\chi_{\rm S} - \frac{\chi_{\rm A}}{\delta} \right), \tag{B14} \qquad \delta_{52} = \frac{4}{15} \Omega H_{\rm EOB},$$

$$\delta_{41} = \left(\frac{1}{5} + \frac{507}{10}\nu\right) \frac{\Omega H_{\rm EOB}}{1 - 2\nu} + \frac{1571}{3465}\pi(\Omega H_{\rm EOB})^2, \qquad (B15) \qquad \rho_{51} = 1 + \frac{8\nu^2 - 626\nu + 319}{390(2\nu - 1)}v_{\Omega}^2 - \frac{31877}{304200}v_{\Omega}^4, \qquad (B22)$$

$$\rho_{54} = 1 + \frac{33320\nu^{3} - 127610\nu^{2} + 96019\nu - 17448}{13650(5\nu^{2} - 5\nu + 1)} v_{\Omega}^{2}$$

$$-\frac{16213384}{15526875} v_{\Omega}^{4}, \qquad (B16)$$

$$(B23)$$

$$\delta_{54} = \frac{8}{15} \Omega H_{EOB}, \qquad (B17) \qquad \rho_{66} = 1 + \frac{273\nu^3 - 861\nu^2 + 602\nu - 106}{84(5\nu^2 - 5\nu + 1)} v_{\Omega}^2 - \frac{1025435}{659736} v_{\Omega}^4, \qquad (B24)$$

$$\rho_{53} = 1 + \frac{176\nu^2 - 850\nu + 375}{390(2\nu - 1)} v_{\Omega}^2 - \frac{410833}{709800} v_{\Omega}^4, \quad (B18)$$

$$\delta_{53} = \frac{31}{70} \Omega H_{\text{EOB}}, \tag{B19}$$

$$\rho_{52} = 1 + \frac{21980\nu^3 - 104930\nu^2 + 84679\nu - 15828}{13650(5\nu^2 - 5\nu + 1)}v_{\Omega}^2 \qquad \rho_{65} = 1 + \frac{220\nu^3 - 910\nu^2 + 838\nu - 185}{144(3\nu^2 - 4\nu + 1)}v_{\Omega}^2, \tag{B26}$$

$$-\frac{7187914}{15526875}v_{\Omega}^{4}, \qquad (B20) \qquad \delta_{65} = \frac{10}{21}\Omega H_{EOB}, \qquad (B27)$$

 $\delta_{66} = \frac{43}{70} \Omega H_{EOB},$

(B35)

(B37)

$$\rho_{64} = 1 + \frac{133\nu^3 - 581\nu^2 + 462\nu - 86}{84(5\nu^2 - 5\nu + 1)}v_{\Omega}^2 - \frac{476887}{659736}v_{\Omega}^4, \qquad \rho_{61} = 1 + \frac{124\nu^3 - 670\nu^2 + 694\nu - 161}{144(3\nu^2 - 4\nu + 1)}v_{\Omega}^2, \tag{B34}$$

(B28) $\delta_{61} = \frac{2}{21} \Omega H_{EOB},$

$$\delta_{64} = \frac{43}{105} \Omega H_{\rm EOB}, \tag{B29}$$

$$\rho_{77} = 1 + \frac{1380\nu^3 - 4963\nu^2 + 4246\nu - 906}{714(3\nu^2 - 4\nu + 1)}v_{\Omega}^2,$$
 (B36)

$$\rho_{63} = 1 + \frac{156\nu^3 - 750\nu^2 + 742\nu - 169}{144(3\nu^2 - 4\nu + 1)} v_{\Omega}^2,$$
(B30)
$$\delta_{77} = \frac{19}{26} \Omega H_{EOB},$$

$$\delta_{63} = \frac{2}{7} \Omega H_{\text{EOB}}, \tag{B31} \qquad \rho_{76} = 1 + \frac{6104 \nu^4 - 29351 \nu^3 + 37828 \nu^2 - 16185 \nu + 2144}{1666 (7 \nu^3 - 14 \nu^2 + 7 \nu - 1)} v_{\Omega}^2, \tag{B31}$$

$$\rho_{62} = 1 + \frac{49\nu^3 - 413\nu^2 + 378\nu - 74}{84(5\nu^2 - 5\nu + 1)}v_{\Omega}^2 - \frac{817991}{3298680}v_{\Omega}^4,$$

$$(B32) \qquad \rho_{75} = 1 + \frac{804\nu^3 - 3523\nu^2 + 3382\nu - 762}{714(3\nu^2 - 4\nu + 1)}v_{\Omega}^2,$$

$$(B39)$$

$$\delta_{62} = \frac{43}{210} \Omega H_{EOB}, \qquad (B33) \qquad \delta_{75} = \frac{95}{252} \Omega H_{EOB}, \qquad (B40)$$

 $\rho_{74} = 1 + \frac{41076\nu^4 - 217959\nu^3 + 298872\nu^2 - 131805\nu + 17756}{14994(7\nu^3 - 14\nu^2 + 7\nu - 1)}v_{\Omega}^2, \tag{B41}$

$$\rho_{73} = 1 + \frac{420\nu^3 - 2563\nu^2 + 2806\nu - 666}{714(3\nu^2 - 4\nu + 1)}v_{\Omega}^2, \tag{B42}$$

$$\delta_{73} = \frac{19}{84} \Omega H_{\text{EOB}},\tag{B43}$$

$$\rho_{72} = 1 + \frac{32760\nu^4 - 190239\nu^3 + 273924\nu^2 - 123489\nu + 16832}{14994(7\nu^3 - 14\nu^2 + 7\nu - 1)}v_{\Omega}^2, \tag{B44}$$

$$\rho_{71} = 1 + \frac{228\nu^3 - 2083\nu^2 + 2518\nu - 618}{714(3\nu^2 - 4\nu + 1)} v_{\Omega}^2, \tag{B45}$$

$$\delta_{71} = \frac{19}{252} \Omega H_{EOB}, \tag{B46}$$

$$\rho_{88} = 1 + \frac{3482 - 26778\nu + 64659\nu^2 - 53445\nu^3 + 12243\nu^4}{2736(-1 + 7\nu - 14\nu^2 + 7\nu^3)}v_{\Omega}^2, \tag{B47}$$

$$\rho_{87} = 1 + \frac{23478 - 154099\nu + 309498\nu^2 - 207550\nu^3 + 38920\nu^4}{18240(-1 + 6\nu - 10\nu^2 + 4\nu^3)}v_{\Omega}^2,$$
(B48)

$$\rho_{86} = 1 + \frac{1002 - 7498\nu + 17269\nu^2 - 13055\nu^3 + 2653\nu^4}{912(-1 + 7\nu - 14\nu^2 + 7\nu^3)}v_{\Omega}^2, \tag{B49}$$

$$\rho_{85} = 1 + \frac{4350 - 28055\nu + 54642\nu^2 - 34598\nu^3 + 6056\nu^4}{3648(-1 + 6\nu - 10\nu^2 + 4\nu^3)}v_{\Omega}^2, \tag{B50}$$

$$\rho_{84} = 1 + \frac{2666 - 19434\nu + 42627\nu^2 - 28965\nu^3 + 4899\nu^4}{2736(-1 + 7\nu - 14\nu^2 + 7\nu^3)}v_{\Omega}^2, \tag{B51}$$

$$\rho_{83} = 1 + \frac{20598 - 131059\nu + 249018\nu^2 - 149950\nu^3 + 24520\nu^4}{18240(-1 + 6\nu - 10\nu^2 + 4\nu^3)}v_{\Omega}^2, \tag{B52}$$

$$\rho_{82} = 1 + \frac{2462 - 17598\nu + 37119\nu^2 - 22845\nu^3 + 3063\nu^4}{2736(-1 + 7\nu - 14\nu^2 + 7\nu^3)}v_{\Omega}^2, \tag{B53}$$

$$\rho_{81} = 1 + \frac{20022 - 126451\nu + 236922\nu^2 - 138430\nu^3 + 21640\nu^4}{18240(-1 + 6\nu - 10\nu^2 + 4\nu^3)}v_{\Omega}^2.$$
(B54)

APPENDIX C: FITS OF NONQUASICIRCULAR INPUT VALUES

In this appendix we provide fits for the NQC input values, $|h_{\ell m}(t_{\mathrm{match}}^{\ell m})|$, $\partial_t |h_{\ell m}(t_{\mathrm{match}}^{\ell m})|$, $\partial_t^2 |h_{\ell m}(t_{\mathrm{match}}^{\ell m})|$, $\omega_{\ell m}(t_{\mathrm{match}}^{\ell m})$, $\partial_t \omega_{\ell m}(t_{\mathrm{match}}^{\ell m})|$. To produce the fits we used NR simulations with the highest level of resolution available and extrapolation order N=2. Depending on the mode, we excluded a different number of NR waveforms from the fits, where numerical errors prevented us from fitting them accurately. As in Ref. [78] we define the following combinations of m_1 , m_2 , χ_1 , χ_2 to be used in the fits:

$$\delta = \frac{(m_1 - m_2)}{(m_1 + m_2)},\tag{C1}$$

$$\chi_{33} = \chi_S \delta + \chi_A \tag{C2}$$

$$\chi_{21A} = \frac{\chi_S}{1 - 1.3\nu} \delta + \chi_A \tag{C3}$$

$$\chi_{44A} = (1 - 5\nu)\chi_S + \chi_A \delta \tag{C4}$$

$$\chi_{21D} = \frac{\chi_S}{1 - 2\nu} \delta + \chi_A \tag{C5}$$

$$\chi_{44D} = (1 - 7\nu)\chi_S + \chi_A \delta \tag{C6}$$

$$\chi = \chi_S + \chi_A \frac{\delta}{1 - 2\nu}.$$
 (C7)

The variables χ_{33} , χ_{21A} , χ_{21D} vanish by construction for equal-mass equal-spin configurations, and are used to enforce that the odd-m modes also vanish in the same limit as required by symmetry.

1. Amplitude's fits

$$\frac{|h_{22}^{\text{NR}}(t_{22}^{\text{match}})|}{\nu} = |0.430147\chi^{3}\nu - 0.084939\chi^{3} + 0.619889\chi^{2}\nu^{2} - 0.020826\chi^{2} - 13.357614\chi\nu^{3} + 7.194264\chi\nu^{2} - 1.743135\chi\nu + 0.18694\chi + 71.979698\nu^{4} - 46.87586\nu^{3} + 12.440405\nu^{2} - 0.868289\nu + 1.467097| (C8)$$

$$\frac{|h_{33}^{\text{NR}}(t_{33}^{\text{match}})|}{\nu} = |-0.088371\chi_{33}^2\delta\nu + 0.036258\chi_{33}^2\delta + 1.057731\chi_{33}\nu^2 - 0.466709\chi_{33}\nu + 0.099543\chi_{33} + 1.96267\delta\nu^2 + 0.027833\delta\nu + 0.558808\delta|$$
(C9)

$$\frac{|h_{21}^{NR}(t_{21}^{match})|}{\nu} = |-0.033175\chi_{21A}^{3}\delta + 0.086356\chi_{21A}^{2}\delta\nu - 0.049897\chi_{21A}^{2}\delta + 0.012706\chi_{21A}\delta + 0.168668\chi_{21A}\nu - 0.285597\chi_{21A} + 1.067921\delta\nu^{2} - 0.189346\delta\nu + 0.431426\delta|$$
(C10)

$$\frac{|h_{44}^{\text{NR}}(t_{44}^{\text{match}})|}{\nu} = |0.031483\chi_{44A}^2 - 0.180165\chi_{44A}\nu + 0.063931\chi_{44A} + 6.239418\nu^3 - 1.947473\nu^2 - 0.615307\nu + 0.262533|$$
(C11)

$$\frac{|h_{55}^{\text{NR}}(t_{55}^{\text{match}})|}{\nu} = |-7.402839\chi_{33}\nu^3 + 3.965852\chi_{33}\nu^2 - 0.762776\chi_{33}\nu + 0.062757\chi_{33} + 1.093812\delta\nu^2 - 0.462142\delta\nu + 0.125468\delta|$$
(C12)

$$\frac{|h_{32}^{\text{NR}}(t_{32}^{\text{match}})|}{\nu} = |0.022598\chi^2 + 0.307803\chi\nu - 0.020771\chi + 8.917771\nu^3 - 2.194506\nu^2 - 0.387911\nu + 0.155446| \quad \text{(C13)}$$

$$\frac{|h_{43}^{\text{NR}}(t_{43}^{\text{match}})|}{\nu} = |-0.071554\chi_{33}^2\delta\nu + 0.021932\chi_{33}^2\delta - 1.738079\chi_{33}\nu^2 + 0.436576\chi_{33}\nu - 0.020081\chi_{33} + 0.809615\delta\nu^2 - 0.273364\delta\nu + 0.07442\delta|$$
(C14)

2. Amplitude-first-derivative's fits

$$\frac{1}{\nu} \frac{d|h_{22}^{\text{NR}}(t)|}{dt} \bigg|_{t=t_{22}^{\text{match}}} \equiv 0 \tag{C15}$$

$$\frac{1}{\nu} \frac{d|h_{33}^{NR}(t)|}{dt}\Big|_{t=t_{33}^{\text{match}}} = \chi_{33}^2 \delta(0.004941\nu - 0.002094)
+ 0.001781|\chi_{33}^2 + \chi_{33}\delta(39.247538\nu - 2.986889) + \delta^2(85.173306\nu + 4.637906)|^{1/2}$$
(C16)

$$\frac{1}{\nu} \frac{d|h_{21}^{NR}(t)|}{dt} \Big|_{t=t_{21}^{\text{match}}} = \chi_{21D} \delta(0.023534\nu - 0.008064) + \delta(0.006743 - 0.0297\nu)
+ 0.008256|\chi_{21D} - \delta(5.471011\nu^2 + 1.235589\nu + 0.815482)|$$
(C17)

$$\frac{1}{\nu} \frac{d|h_{44}^{\text{NR}}(t)|}{dt} \Big|_{t=t_{44}^{\text{match}}} = -0.001251\chi_{44D}^3 + 0.006387\chi_{44D}^2\nu - 0.001223\chi_{44D}^2 - 0.034308\chi_{44D}\nu^2
+ 0.014373\chi_{44D}\nu - 0.000681\chi_{44D} + 1.134679\nu^3 - 0.417056\nu^2 + 0.024004\nu + 0.003498 \quad (C18)$$

$$\frac{1}{\nu} \frac{d|h_{55}^{NR}(t)|}{dt}\Big|_{t=t_{55}^{\text{match}}} = \chi_{33}^2 \delta(0.008568\nu - 0.00155) + \chi_{33} \delta(0.002705\nu - 0.001015)
+ \delta(0.002563 - 0.010891\nu) + 0.000284|\chi_{33} + \delta(32.459725\nu + 0.165336)|$$
(C19)

$$\frac{1}{\nu} \frac{d|h_{32}^{NR}(t)|}{dt} \bigg|_{t=t_{32}^{\text{match}}} = -0.000806\chi^3 - 0.011027\chi^2\nu + 0.002999\chi^2 - 0.14087\chi\nu^2 + 0.063211\chi\nu
- 0.006783\chi + 1.693423\nu^3 - 0.510999\nu^2 + 0.020607\nu + 0.003674$$
(C20)

$$\frac{1}{\nu} \frac{d|h_{43}^{\text{NR}}(t)|}{dt}\Big|_{t=t_{43}^{\text{match}}} = \chi_{33}^2 \delta(0.001773 - 0.012159\nu) + \chi_{33} \delta(0.022249\nu - 0.004295)
+ \delta(0.012043\nu - 0.001067) + 0.00082|\chi_{33} + \delta(3.880171 - 20.015436\nu)|$$
(C21)

3. Amplitude-second-derivative's fits

$$\frac{1}{\nu} \frac{d^2 |h_{22}^{\text{NR}}(t)|}{dt^2} \bigg|_{t=t_{\text{match}}^{\text{match}}} = 0.000386 \chi^2 + 0.003589 \chi \nu + 0.001326 \chi - 0.003353 \nu^2 - 0.005615 \nu - 0.002457$$
 (C22)

$$\frac{1}{\nu} \frac{d^{2} |h_{33}^{NR}(t)|}{dt^{2}} \bigg|_{t=t_{33}^{\text{match}}} = \chi_{33} \delta(0.000552\nu + 0.001029) - 0.000218$$

$$\cdot |\chi_{33} + \delta(-2188.340923\nu^{4} + 1331.981345\nu^{3} - 289.772357\nu^{2} + 32.212775\nu + 3.396168)| \quad (C23)$$

$$\frac{1}{\nu} \frac{d^2 |h_{21}^{NR}(t)|}{dt^2} \bigg|_{t=t_{21}^{\text{match}}} = 0.00015\delta - |0.000316\chi_{21D}^3 - \chi_{21D}^2 \delta(-0.043291\nu^2 + 0.005682\nu + 0.000502)
+0.000372\chi_{21D}\delta - \delta(0.003643\nu + 2.8 \times 10^{-5})|$$
(C24)

$$\frac{1}{\nu} \frac{d^2 |h_{44}^{NR}(t)|}{dt^2} \bigg|_{t=t_{44}^{\text{match}}} = -0.000591 \chi^2 \nu + 0.000174 \chi^2 - 0.000501 \chi \nu + 0.000318 \chi + 0.138496 \nu^3
- 0.047008 \nu^2 + 0.003899 \nu - 0.000451$$
(C25)

$$\frac{1}{\nu} \frac{d^2 |h_{55}^{\rm NR}(t)|}{dt^2} \bigg|_{t=t_{55}^{\rm match}} = \chi_{33}^2 \cdot (0.000278\nu - 5.6 \times 10^{-5}) + \chi_{33} \delta(0.000246\nu - 6.8 \times 10^{-5}) + \delta(0.000118 - 5.9 \times 10^{-5}\nu) \tag{C26}$$

$$\frac{1}{\nu} \frac{d^2 |h_{32}^{NR}(t)|}{dt^2} \bigg|_{t=t_{32}^{\text{match}}} = -0.002882 \chi^2 \nu + 0.000707 \chi^2 - 0.027461 \chi \nu^2 + 0.008481 \chi \nu - 0.000691 \chi
+ 0.20836 \nu^3 - 0.053191 \nu^2 + 0.001604 \nu - 5.6 \times 10^{-5}$$
(C27)

$$\frac{1}{\nu} \frac{d^2 |h_{43}^{\rm NR}(t)|}{dt^2} \bigg|_{t=t_{43}^{\rm match}} = \chi_{33} \delta(0.00291\nu - 0.000348) - 5.0 \times 10^{-6} \\ \cdot |\chi_{33} + \delta(-25646.358742\nu^4 + 12647.805787\nu^3 + 291.751053\nu^2 - 531.965263\nu + 23.849357)|$$
 (C28)

4. Frequency and frequency-derivative fits

$$\omega_{22}^{NR}(t_{22}^{\text{match}}) = -0.015259\chi^4 + 0.241948\chi^3\nu - 0.066927\chi^3 - 0.971409\chi^2\nu^2 + 0.518014\chi^2\nu - 0.087152\chi^2 + 3.751456\chi\nu^3 - 1.697343\chi\nu^2 + 0.250965\chi\nu - 0.091339\chi + 5.893523\nu^4 - 3.349305\nu^3 + 0.285392\nu^2 - 0.317096\nu - 0.268541$$
 (C29)

$$\omega_{33}^{\text{NR}}(t_{33}^{\text{match}}) = -0.045141\chi^{3} + 0.346675\chi^{2}\nu - 0.119419\chi^{2} - 0.745924\chi\nu^{2} + 0.478915\chi\nu - 0.17467\chi + 8.887163\nu^{3} - 4.226831\nu^{2} - 0.427167$$
(C30)

$$\omega_{21}^{\text{NR}}(t_{21}^{\text{match}}) = -0.01009\chi^{3} + 0.077343\chi^{2}\nu - 0.02411\chi^{2} - 0.168854\chi\nu^{2} + 0.159382\chi\nu - 0.047635\chi - 1.965157\nu^{3} + 0.53085\nu^{2} - 0.237904\nu - 0.176526$$
(C31)

$$\omega_{44}^{\text{NR}}(t_{44}^{\text{match}}) = -0.042529\chi^3 + 0.415864\chi^2\nu - 0.155222\chi^2 - 0.768712\chi\nu^2 + 0.592568\chi\nu - 0.244508\chi + 13.651335\nu^3 - 5.490329\nu^2 - 0.574041$$
(C32)

$$\omega_{55}^{NR}(t_{55}^{\text{match}}) = -0.091629\chi^3 + 0.802759\chi^2\nu - 0.246646\chi^2 - 3.04576\chi\nu^2 + 1.43471\chi\nu - 0.329591\chi + 13.81386\nu^3 - 6.61611\nu^2 + 0.472474\nu - 0.589341$$
 (C33)

$$\omega_{32}^{NR}(t_{32}^{\text{match}}) = -0.045647\chi^2 - 2.758635\chi\nu^2 + 0.811353\chi\nu - 0.112477\chi - 2.346024\nu^3 + 1.57986\nu^2 - 0.317756\nu - 0.331141$$
 (C34)

$$\omega_{43}^{NR}(t_{43}^{\text{match}}) = -0.037919\chi^3 + 0.226903\chi^2\nu - 0.087288\chi^2 - 0.905919\chi\nu^2 + 0.291092\chi\nu - 0.1198\chi - 55.534105\nu^3 + 23.913277\nu^2 - 3.487986\nu - 0.34306$$
 (C35)

$$\dot{\omega}_{22}^{\text{NR}}(t_{22}^{\text{match}}) = 0.000614\chi^3 - 0.008393\chi^2\nu + 0.001948\chi^2 + 0.07799\chi\nu^2 - 0.028772\chi\nu + 0.001705\chi - 0.237126\nu^3 + 0.092215\nu^2 - 0.03104\nu - 0.005484$$
 (C36)

$$\dot{\omega}_{33}^{NR}(t_{33}^{\text{match}}) = 0.001697\chi^3 - 0.016231\chi^2\nu + 0.003985\chi^2 + 0.154378\chi\nu^2 - 0.050618\chi\nu + 0.002721\chi + 0.255402\nu^3 - 0.08663\nu^2 - 0.027405\nu - 0.009736$$
(C37)

$$\dot{\omega}_{21}^{NR}(t_{21}^{\text{match}}) = 0.00149\chi^3 - 0.008965\chi^2\nu + 0.002739\chi^2 + 0.033831\chi\nu^2 - 0.005752\chi\nu + 0.002003\chi - 0.204368\nu^3 + 0.120705\nu^2 - 0.035144\nu - 0.006579$$
 (C38)

$$\dot{\omega}_{44}^{\text{NR}}(t_{44}^{\text{match}}) = 0.001812\chi^{3} - 0.024687\chi^{2}\nu + 0.00568\chi^{2} + 0.162693\chi\nu^{2} - 0.061205\chi\nu + 0.003623\chi + 0.536664\nu^{3} - 0.094797\nu^{2} - 0.045406\nu - 0.013038$$
(C39)

$$\dot{\omega}_{55}^{NR}(t_{55}^{\text{match}}) = 0.001509\chi^{3} - 0.01547\chi^{2}\nu + 0.002802\chi^{2} + 0.164011\chi\nu^{2} - 0.056516\chi\nu + 0.002072\chi + 0.043963\nu^{3} + 0.048045\nu^{2} - 0.045197\nu - 0.008688$$
(C40)

$$\dot{\omega}_{32}^{NR}(t_{32}^{\text{match}}) = -0.036711\chi^{2}\nu + 0.005532\chi^{2} + 0.09192\chi\nu^{2} - 0.030713\chi\nu + 0.005927\chi - 2.494788\nu^{3} + 0.995116\nu^{2} - 0.10163\nu - 0.010763$$
(C41)

$$\dot{\omega}_{43}^{\text{NR}}(t_{43}^{\text{match}}) = 0.000537\chi^3 - 0.009876\chi^2\nu + 0.003279\chi^2 + 0.13296\chi\nu^2 - 0.060884\chi\nu + 0.008513\chi - 5.160613\nu^3 + 2.180781\nu^2 - 0.292607\nu - 0.005308$$
(C42)

APPENDIX D: FITS FOR AMPLITUDE AND PHASE OF MERGER-RINGDOWN MODEL

In this appendix we provide fits across parameter space for the free coefficients in the merger-ringdown Ansatz given by Eqs. (49) and (50). To produce the fits we use NR simulations with the highest level of resolution available and extrapolation order N = 2. They read as

$$c_{1,f}^{22} = -0.001777\chi^4 + 0.062842\chi^3\nu - 0.018908\chi^3 + 0.013161\chi^2\nu^2 + 0.049388\chi^2\nu - 0.019314\chi^2 + 1.867978\chi\nu^3 - 0.702488\chi\nu^2 + 0.033885\chi\nu - 0.011612\chi - 4.238246\nu^4 + 2.043712\nu^3 - 0.406992\nu^2 + 0.053589\nu + 0.086254$$
 (D1)

$$c_{2,f}^{22} = 1.021875\chi^{3}\nu - 0.20348\chi^{3} - 3.556173\chi^{2}\nu^{2} + 1.970082\chi^{2}\nu - 0.264297\chi^{2}$$

$$+ 2.002947\chi\nu^{3} - 5.585851\chi\nu^{2} + 1.837724\chi\nu - 0.27076\chi - 63.286459\nu^{4}$$

$$+ 44.331389\nu^{3} - 9.529573\nu^{2} + 1.155695\nu - 0.528763$$
(D2)

$$d_{1,f}^{22} = -0.013321\chi^4 + 0.047305\chi^3\nu - 0.024203\chi^3 + 1.033352\chi^2\nu^2 - 0.254351\chi^2\nu - 0.007847\chi^2 + 4.113463\chi\nu^3 - 1.652924\chi\nu^2 + 0.090834\chi\nu - 28.423701\nu^4 + 20.719874\nu^3 - 6.075679\nu^2 + 0.780093\nu + 0.135758$$
(D3)

$$d_{2.f}^{22} = \exp(-0.163113\chi^4 - 3.398858\chi^3\nu + 0.728816\chi^3 + 23.975132\chi^2\nu^2 - 10.064954\chi^2\nu + 1.2115\chi^2 + 9.057306\chi\nu^3 - 5.268296\chi\nu^2 + 0.464553\chi\nu + 0.56269\chi - 352.249383\nu^4 + 275.843499\nu^3 - 81.483314\nu^2 + 11.184576\nu + 0.03571)$$
(D4)

$$c_{1,f}^{33} = -0.00956\chi^3 + 0.029459\chi^2\nu - 0.020264\chi^2 - 0.494524\chi\nu^2 + 0.169463\chi\nu - 0.026285\chi - 5.847417\nu^3 + 1.957462\nu^2 - 0.171682\nu + 0.093539$$
 (D5)

$$c_{2,f}^{33} = -0.057346\chi^3 + 0.237107\chi^2\nu - 0.094285\chi^2 - 4.250609\chi\nu^2 + 1.763105\chi\nu - 0.315826\chi + 14.801916\nu^3 - 7.060581\nu^2 + 1.158627\nu - 0.646888$$
 (D6)

$$d_{1,f}^{33} = -0.016524\chi^3 + 0.221466\chi^2\nu - 0.066323\chi^2 + 0.678442\chi\nu^2 - 0.261264\chi\nu + 0.006664\chi + 2.316434\nu^3 - 2.192227\nu^2 + 0.424582\nu + 0.161577$$
(D7)

$$d_{2,f}^{33} = \exp(0.275999\chi^3 - 1.830695\chi^2\nu + 0.512734\chi^2 + 29.072515\chi\nu^2 - 10.581319\chi\nu + 1.310643\chi + 324.310223\nu^3 - 124.681881\nu^2 + 13.200426\nu + 0.410855)$$
(D8)

$$c_{1,f}^{21} = 0.173462\chi^{2}\nu - 0.028873\chi^{2} + 0.197467\chi\nu^{2} - 0.026139\chi - 2.934735\nu^{3} + 1.009106\nu^{2} - 0.112721\nu + 0.099889$$
(D9)

$$c_{2,f}^{21} = 0.183489\chi^{3} + 0.10573\chi^{2} - 20.792825\chi\nu^{2} + 6.867746\chi\nu - 0.484948\chi - 54.917585\nu^{3} + 16.466312\nu^{2} + 0.426316\nu - 0.92208$$
(D10)

$$d_{1,f}^{21} = 0.018467\chi^{4} + 0.398621\chi^{3}\nu - 0.050499\chi^{3} - 0.877201\chi^{2}\nu^{2} + 0.414553\chi^{2}\nu$$
$$-0.068277\chi^{2} - 10.648526\chi\nu^{3} + 4.104918\chi\nu^{2} - 0.723576\chi\nu + 0.039227\chi$$
$$+42.715534\nu^{4} - 18.280603\nu^{3} + 2.236592\nu^{2} - 0.048094\nu + 0.16335$$
(D11)

$$d_{2,f}^{21} = \exp(0.814085\chi^3 - 1.197363\chi^2\nu + 0.560622\chi^2 + 6.44667\chi\nu^2 - 5.630563\chi\nu + 0.949586\chi + 91.269183\nu^3 - 27.329751\nu^2 + 1.101262\nu + 1.040761)$$
(D12)

$$c_{1,f}^{44} = 4.519504\chi\nu^2 - 1.489036\chi\nu + 0.068403\chi - 1656.065439\nu^4 + 817.835726\nu^3 - 127.055379\nu^2 + 6.921968\nu + 0.009386$$
 (D13)

$$c_{2,f}^{44} = 0.964861\chi^{3}\nu - 0.185226\chi^{3} - 12.647814\chi^{2}\nu^{2} + 5.264969\chi^{2}\nu - 0.539721\chi^{2}$$
$$-254.719552\chi\nu^{3} + 105.698791\chi\nu^{2} - 12.107281\chi\nu + 0.2244\chi - 393.727702\nu^{4}$$
$$+145.32788\nu^{3} - 15.556222\nu^{2} + 1.592449\nu - 0.677664$$
(D14)

$$d_{1,f}^{44} = -0.020644\chi^{3} + 0.494221\chi^{2}\nu - 0.127074\chi^{2} + 4.297985\chi\nu^{2} - 1.284386\chi\nu + 0.062684\chi - 44.280815\nu^{3} + 11.021482\nu^{2} - 0.162943\nu + 0.166018$$
(D15)

$$d_{2,f}^{44} = \exp(37.735116\chi\nu^2 - 12.516669\chi\nu + 1.309868\chi - 528.368915\nu^3 + 155.115196\nu^2 - 6.612448\nu + 0.787726)$$
(D16)

$$c_{1,f}^{55} = -0.009957\chi^3 + 0.059748\chi^2\nu - 0.02146\chi^2 - 0.206811\chi\nu^2 + 0.055078\chi\nu - 0.014528\chi - 5.966891\nu^3 + 1.76928\nu^2 - 0.055272\nu + 0.080368$$
(D17)

$$c_{2,f}^{55} = 0.119703\chi^4 + 1.638345\chi^2\nu^2 - 0.064725\chi^2 - 28.499278\chi\nu^3 + 3.73034\chi\nu^2 + 1.853723\chi\nu - 0.225283\chi - 1887.591102\nu^4 + 794.134711\nu^3 - 107.010824\nu^2 + 6.32117\nu - 1.507483$$
 (D18)

$$d_{1,f}^{55} = -0.021537\chi^3 + 0.168071\chi^2\nu - 0.050263\chi^2 + 0.871799\chi\nu^2 - 0.230057\chi\nu + 9.018546\nu^3 - 5.009488\nu^2 + 0.606313\nu + 0.150622$$
 (D19)

$$d_{2,f}^{55} = \exp(28.839035\chi\nu^2 - 9.726025\chi\nu + 0.901423\chi + 143.745208\nu^3 - 64.478227\nu^2 + 6.223833\nu + 2.058139)$$
(D20)

$$c_{1,f}^{32} = -0.133035\chi^3 + 0.641681\chi^2\nu - 0.111865\chi^2 + 8.987763\chi\nu^2 - 1.582259\chi\nu + 0.095604\chi - 26.991806\nu^3 + 13.716801\nu^2 - 1.63083\nu + 0.157543$$
 (D21)

$$c_{2,f}^{32} = 0.121608\chi^3 - 1.590623\chi^2\nu + 0.167231\chi^2 - 25.544931\chi\nu^2 + 10.127968\chi\nu - 0.999062\chi - 51.469773\nu^3 + 46.209833\nu^2 - 6.484571\nu - 0.716883$$
 (D22)

$$d_{1,f}^{32} = \exp(-0.764015\chi^3 - 8.684722\chi^2\nu + 0.691946\chi^2 - 0.518291\chi\nu^2 - 1.407934\chi\nu + 0.236427\chi + 81.222175\nu^3 - 18.040529\nu^2 + 2.216406\nu - 1.879455)$$
(D23)

$$d_{2,f}^{32} = \exp(-1.819822\chi^3 - 24.501503\chi^2\nu + 3.287882\chi^2 - 39.324579\chi\nu^2 + 14.379901\chi\nu - 215.372399\nu^3 + 136.20936\nu^2 - 16.842816\nu + 1.463485)$$
(D24)

$$c_{1,f}^{43} = 0.041585\chi^3 + 4.188908\chi\nu^2 - 1.365732\chi\nu + 0.058908\chi + 44.311948\nu^3 - 22.114177\nu^2 + 3.386082\nu - 0.035315$$
 (D25)

$$c_{2,f}^{43} = 0.125764\chi^3 + 0.337235\chi^2\nu + 0.146202\chi^2 - 9.803187\chi\nu^2 + 3.995199\chi\nu - 0.240976\chi - 57.968821\nu^3 + 7.820929\nu^2 + 3.364741\nu - 1.121716$$
(D26)

$$d_{1,f}^{43} = \exp(-0.888286\chi^3 + 3.97869\chi^2\nu - 1.047181\chi^2 - 14.823391\chi\nu^2 + 6.940856\chi\nu - 0.367801\chi + 366.645645\nu^3 - 161.732513\nu^2 + 19.564699\nu - 2.29578)$$
(D27)

$$d_{2,f}^{43} = \exp(-0.950676\chi^3 - 0.31428\chi^2 + 39.21796\chi\nu^2 - 10.651167\chi\nu + 1.339732\chi + 730.42296\nu^3 - 312.960598\nu^2 + 37.402567\nu - 0.061894).$$
(D28)

APPENDIX E: ROBUSTNESS OF THE CALIBRATION PIPELINE

In this appendix we demonstrate that the calibration pipeline described in Sec. V is robust with regard to the number of NR waveforms and the PSD used in the calibration likelihood.

For the first point, we repeat the procedure for the aligned-spin calibration parameters $\theta_{\rm S} \equiv \{d_{\rm SO}, \Delta t_{\rm ISCO,S}^{22}\}$, by using a representative subset of 119 aligned-spin NR simulations, selected with a greedy algorithm following Ref. [100]. We do not change the nonspinning fits for $\theta_{\rm noS} \equiv \{a_6, \Delta t_{\rm ISCO,noS}^{22}\}$ (which already used a subset of 18 simulations out of 39), and the fits for the merger-ringdown and NQC corrections. This brings the total number of waveforms used to 137, which is comparable to the 141 used in the calibration of SEOBNRv4. As in Sec. VI, we

compute the (2,2)-mode mismatch of this model against the entire set of 442 cases summarized in Sec. V. Figure 26 shows the maximum mismatch across a range of total masses between $[10,300]M_{\odot}$ for SEOBNRv5 calibrated to 442 simulations, SEOBNRv5 calibrated to 137 simulations, and SEOBNRv4. The median (dashed vertical line) goes only from 1.99×10^{-4} for SEOBNRv5 calibrated to 442 simulations, to 2.74×10^{-4} for SEOBNRv5 calibrated to 137 simulations, which is more than 5 times smaller than SEOBNRv4 (1.44 \times 10⁻³). Moreover for SEOBNRv5 calibrated to 137 simulations there is only a single case with mismatch just above 0.003 (BFI:q8-7d:0080, with parameters $(q, \chi_1, \chi_2) = (8.0, 0.0, -0.8)$. As already pointed out in Sec. VI, even the default SEOBNRv5 model can have mismatches slightly above 10⁻³ against similar cases, with high mass ratio, small a_{+} , but large individual

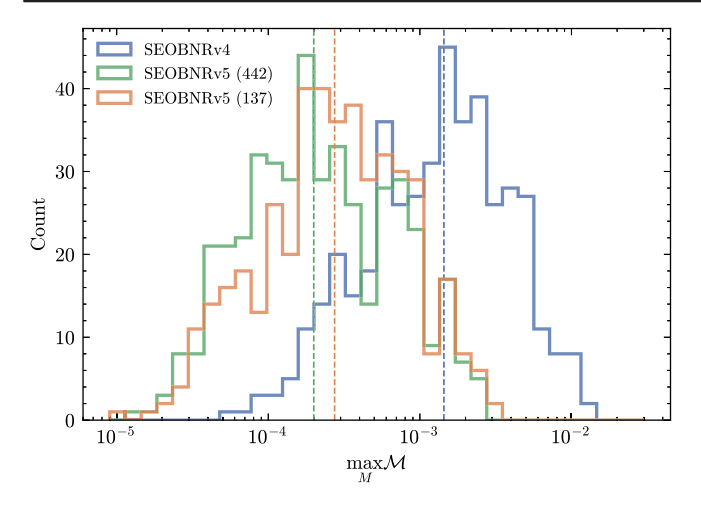


FIG. 26. Histogram of the maximum (2,2)-mode mismatch over a range of total masses between 10 and $300M_{\odot}$, between the 442 NR simulations used in this work and SEOBNRv4 (blue), SEOBNRv5 calibrated to 442 NR simulations (green), and SEOBNRv5 calibrated to 137 NR simulations (orange). The vertical dashed lines show the medians.

spins, as the calibration term $\propto a_+ d_{\rm SO}$ does not tend to be very effective. This shows that the calibration pipeline does not rely on using the entire NR dataset described in Sec. V. Although we added some critical new NR simulations, especially for high mass ratios, the improvement with respect to SEOBNRv4 is also largely due to the improved analytical prescriptions, for the waveform modes, RR force, and Hamiltonian, and the more effective calibration procedure.

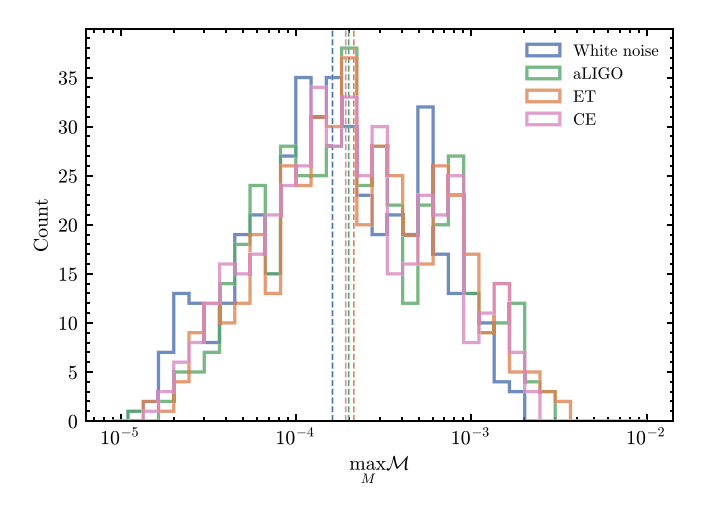


FIG. 27. Histogram of the maximum (2,2)-mode mismatch over a range of total masses between 10 and $300M_{\odot}$, between the 442 NR simulations used in this work and SEOBNRv5, using a white noise curve and the PSDs of Advanced LIGO, Einstein Telescope and Cosmic Explorer. The vertical dashed lines show the medians. The (2,2) mode of SEOBNRv5 is calibrated using the Advanced LIGO PSD, but performs as well using different noise curves.

The calibration likelihood of Eq. (70) also depends on the Advanced LIGO [179] PSD. To show that our calibration pipeline is robust with respect to changes in the shape of the PSD used, we compute again (2,2)-mode mismatches against NR simulations (as this is the metric used in the likelihood) using a white noise curve, the Einsten Telescope [214], and Cosmic Explorer [16] PSDs. For this purpose we use the original fits of $\{d_{SO}, \Delta t_{ISCO,S}^{22}\}$ given in Eqs. (80) and (81). Figure 27 shows again the maximum mismatch, across a range of total masses between $[10,300]M_{\odot}$, of SEOBNRv5 against the 442 NR simulations used in this work, using a white noise curve and the PSDs of Advanced LIGO, Einstein Telescope, and Cosmic Explorer. We see that the result is very similar for all the cases and, despite SEOBNRv5 being calibrated using the Advanced LIGO PSD, it performs equally well using different noise curves.

APPENDIX F: IMPACT OF NQC CORRECTIONS IN THE RADIATION-REACTION FORCE

In Sec. IVA we pointed out that we do not include the NQC corrections in the SEOBNRv5 RR force. Recently, Refs. [114,194] implemented a fast prescription in TEOBResumS to include fits of NOC corrections in both the waveform and RR force, without requiring an iterative procedure. A similar prescription could also be used in SEOBNRv5HM. Reference [125] tested it in the nonspinning limit, finding that the inclusion of NQCs corrections has a smaller effect than the calibration to 2GSF data in bringing the angular-momentum flux closer to the NR's one, except in the last fraction of a GW cycle before the merger. Moreover, Ref. [125] found that the inclusion of the nonspinning NQC corrections has a negligible effect on the waveform after recalibrating the conservative dynamics to NR, as the degeneracy between changes in the flux and in the Hamiltonian reabsorbs any imperfection in the flux with the calibration. The nonspinning limit of the model is however already very close to the NR error, and the effect on more challenging aligned-spin cases could be larger.

While for the current work we did not do a systematic study in the entire aligned-spin parameter space to include the NQC corrections in the RR force, in this appendix we try to understand the potential improvement for one binary configuration and compare the results with SXS:BBH:1432, having parameters $(q,\chi_1,\chi_2) = (5.839,0.658,0.793)$. Thus, we iteratively include the NQCs in the RR force and repeat the nested sampling procedure detailed in Sec. VB to find new values for the aligned-spin calibration parameters $\{\Delta t_{\rm ISCO,S}^{22}, d_{\rm SO}\}$, which are going to slightly change compared to the default ones, given the different dissipative dynamics. To do a comparison without performing fits of the NQCs and of the calibration parameters across parameter space, we directly compare the maximum likelihood points of the

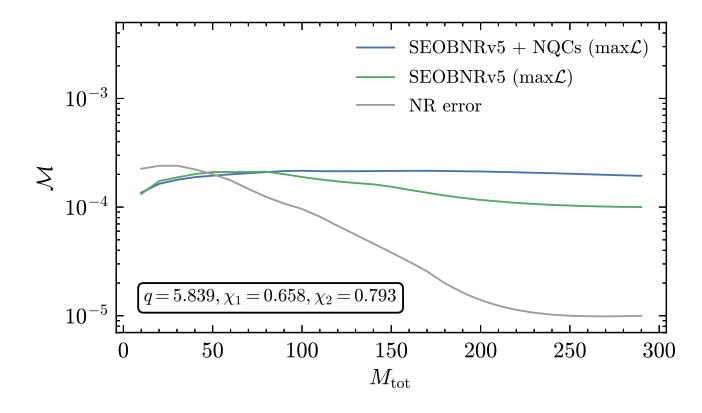


FIG. 28. (2,2)-mode mode mismatch against the NR simulation SXS:BBH:1432 for the maximum likelihood points of the SEOBNRv5 calibration posteriors, with and without NQCs in the RR force. The unfaithfulness is very similar, as the calibration of the Hamiltonian reabsorbs any difference in the dissipative dynamics. We also show an estimate of the NR error obtained by comparing simulations of different resolutions.

calibration posteriors, corresponding to the values of the parameters giving the best unfaithfulness and time to the merger.

Figure 28 shows the (2,2)-mode mismatch against NR for the maximum likelihood points of the SEOBNRv5 calibration posteriors with and without NQCs in the RR force, together with an estimate of the NR error obtained by comparing different resolutions. The unfaithfulness is very similar, as the calibration of the Hamiltonian reabsorbs any difference in the dissipative dynamics. Moreover, in Fig. 29 we compare to NR the Newtonian normalized angularmomentum flux between SEOBNRv5 with and without NQCs in the RR force. The triangle, square, and diamond correspond respectively to 3, 1, and 0 cycles before the merger, which for each model is taken as the peak of the (2,2)-mode amplitude. SEOBNRv5 with NQCs matches NR at the merger at expected, but does not agree with NR as well as SEOBNRv5 without NQCs at low frequencies, showing that the addition of the NQCs does not necessarily improve the flux.

This behavior could be potentially improved by doing more iterations, finding new values for the NQCs given the corrected calibration parameters, and repeating the calibration, but would be time-consuming and not necessarily bring a significant improvement in the waveforms. Nonetheless, a consistent treatment of the NQCs both in the waveform and the RR force would most likely provide more faithful representations of the angular-momentum and energy fluxes, and a more systematic study across parameter space will be done in a future update of the model, together with a recalibration of the conservative dynamics. Alternative ways to improve the waveform close to merger, and reduce the impact of the NQC corrections, should be also investigated, especially in light of the upcoming eccentric generalization of this model SEOBNRv5EHM,

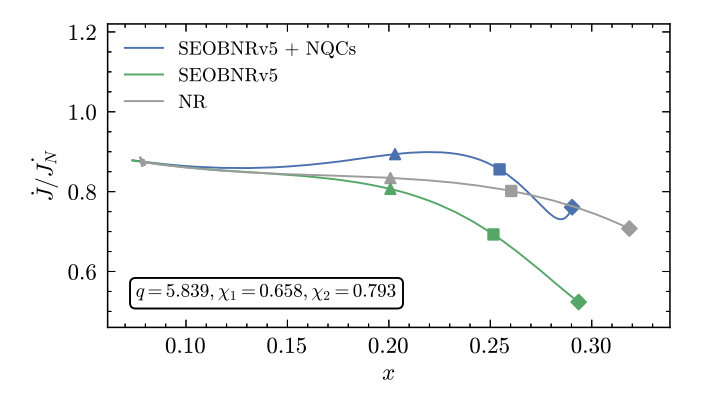


FIG. 29. Comparison of the Newtonian normalized angular-momentum flux between SEOBNRv5 with and without NQCs in the radiation reaction, and the NR simulation SXS:BBH:1432. The triangle, square, and diamond correspond respectively to 3, 1, and 0 cycles before the merger, which for each model is taken as the peak of the (2,2)-mode amplitude. SEOBNRv5 with NQCs matches NR at the merger as expected, but does not agree with NR as well as SEOBNRv5 without NQCs at low frequencies.

as past experience in developing SEOBNRv4EHM has demonstarted [91].

APPENDIX G: COMPARISON AGAINST TIME-DOMAIN NONPRECESSING PHENOMENOLOGICAL MODELS

In this appendix we compare the performance of SEOBNRv5HM and the Fourier domain IMRPhenomXHM [44] against the time-domain nonprecessing phenomenological model IMRPhenomTHM [47,48], which includes the $(\ell,|m|)=(2,2),(3,3),(2,1),(4,4),(5,5)$ modes. In particular, we repeat the mismatch calculation against the NR catalog detailed in Sec. VI, both for the dominant mode only (Figs. 30 and 31) and for the full polarizations, at inclination $\iota=\pi/3$ (Figs. 32 and 33).

Considering the dominant mode mismatches, we see that IMRPhenomT performs slightly worse than SEOBNRv5, considering both the median mismatch and the fraction of cases below 10^{-4} , while IMRPhenomXAS achieves on average slightly lower values of the maximum unfaithfulness, as already noted in Sec. VI. More quantitatively, IMRPhenomT features 91% of cases with maximum unfaithfulness below 10^{-3} , 5% of cases below 10^{-4} , and a median of 2.31×10^{-4} (see also Table I).

Considering the mismatches of the full polarizations at inclination $\iota=\pi/3$ we note instead that IMRPhenomTHM is slightly more accurate than SEOBNRv5HM, and both models are appreciably more accurate than IMRPhenomXHM. More specifically, IMRPhenomTHM shows maximum unfaithfulness below 10^{-2} for 99% of cases, below 10^{-3} for 57% of cases, and a median of 7.49×10^{-4} (see also Table II). The NR simulation BFI:ExtremeAligned:0003, with $q=10.0, \chi_1=0.8, \chi_2=0.5$, is the only outlier reaching

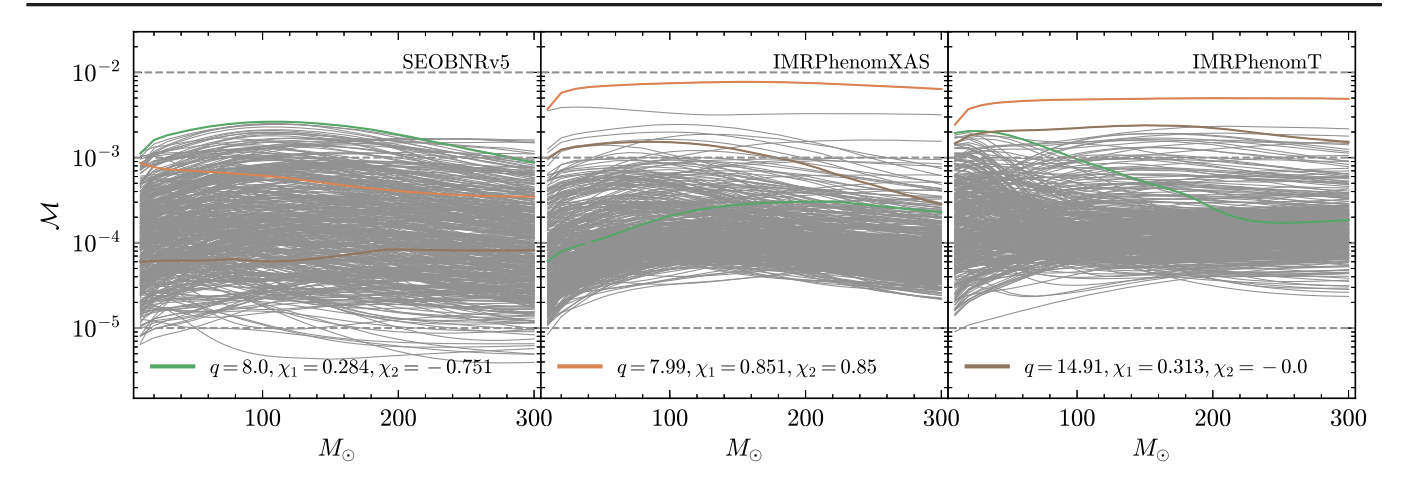


FIG. 30. (2,2)-mode mismatch over a range of total masses between 10 and $300M_{\odot}$, between SEOBNRv5, IMRPhenomXAS, IMRPhenomT, and the 442 NR simulations used in this work. The colored lines highlight cases with the worst maximum mismatch for each model.

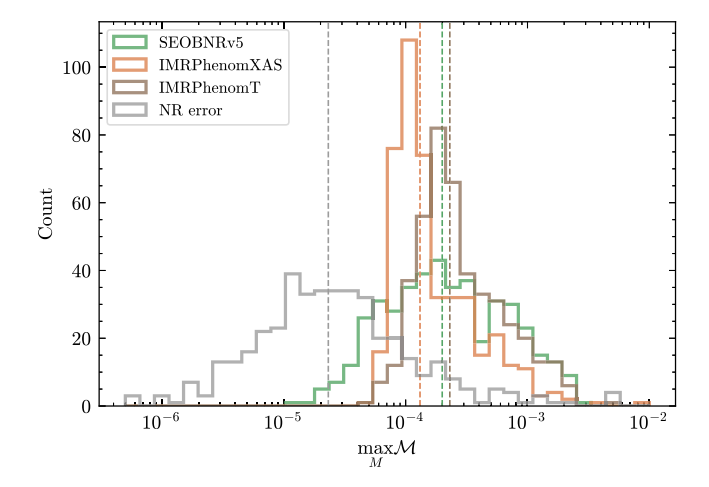


FIG. 31. Histogram of the maximum (2,2)-mode mismatch over a range of total masses between 10 and $300M_{\odot}$, between SEOBNRv5, IMRPhenomXAS, IMRPhenomT, and the 442 NR simulations used in this work. The NR error is estimated by computing the mismatch between NR simulations with the highest and second-highest resolutions. The vertical dashed lines show the medians.

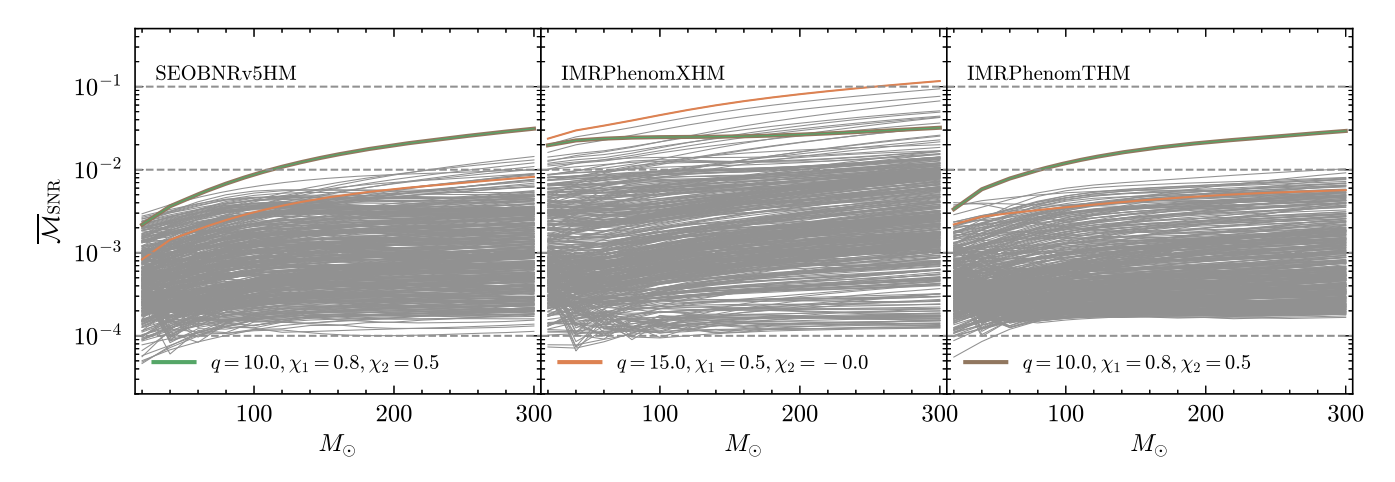


FIG. 32. The sky-and-polarization averaged, SNR-weighted mismatch, for inclination $\iota = \pi/3$, over a range of total masses between 20 and $300 M_{\odot}$ between SEOBNRv5HM, IMRPhenomXHM, IMRPhenomTHM and the 441 SXS NR simulations used in this work. The colored lines highlight cases with the worst maximum mismatch for each model. This comparison highlights the similarity in performance of the time-domain models SEOBNRv5HM and IMRPhenomTHM.

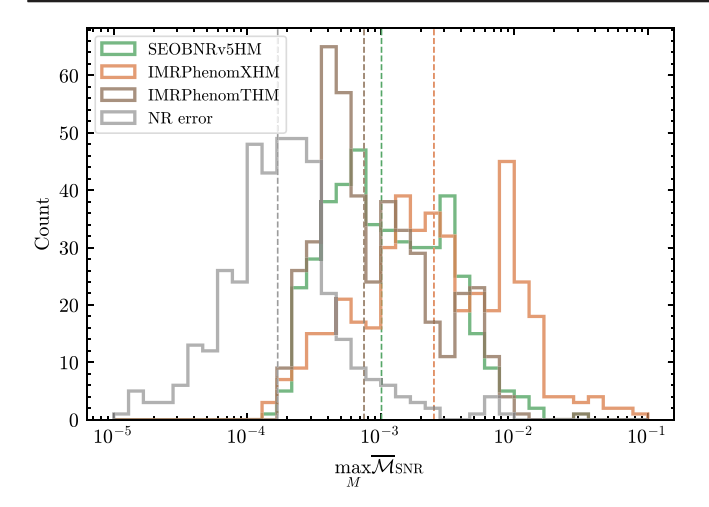


FIG. 33. Histogram of the maximum sky-and-polarization averaged, SNR-weighted mismatch, for inclination $\iota=\pi/3$, over a range of total masses between 20 and $300M_{\odot}$, between SEOBNRv5HM, IMRPhenomXMH, IMRPhenomTHM and the 441 SXS NR simulations used in this work. The NR error is estimated by computing the mismatch between NR simulations with the highest and second-highest resolutions. The vertical dashed lines show the medians.

3% mismatch at high total mass, for both IMRPhenomTHM and SEOBNRv5HM, while being at the level of 0.1% when considering only the (2,2) mode. This suggests common limitations in the modeling of the higher modes for such extreme configurations. In Fig. 34 we show the unfaithfulness between SEOBNRv5HM, IMRPhenomTHM and BFI: ExtremeAligned: 0003, using multipoles up to $\ell_{\rm max}=5$ and $\ell_{\rm max}=4$, in both the models and the NR waveform.

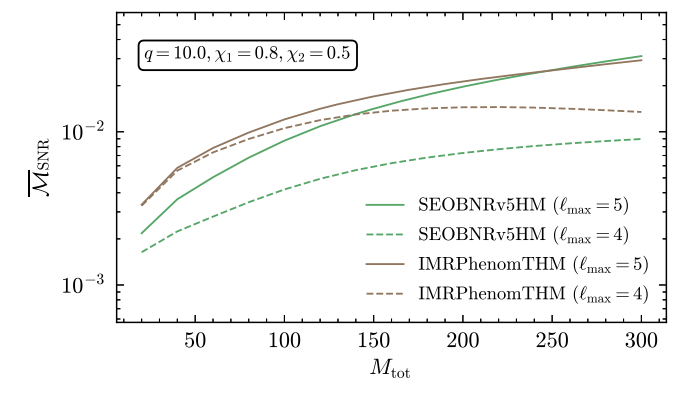


FIG. 34. Sky-and-polarization averaged, SNR-weighted mismatch, for inclination $i=\pi/3$ as a function of the total mass between SEOBNRv5HM, IMRPhenomTHM and the NR simulation BFI:ExtremeAligned:0003, with q=10.0, $\chi_1=0.8,\chi_2=0.5$, using $\ell_{\rm max}=5$ and $\ell_{\rm max}=4$, in both the models and the NR waveform.

We note that the mismatch for high total masses reduces significantly for both models when removing $\ell=5$ multipoles, indicating that part of the disagreement is due to mismodeling of the (5,5) mode, as well as missing contributions in the models from the $(\ell=5, m\neq 5)$ multipoles, which can have a non-negligible impact in the ringdown of such high mass-ratio binaries. From the behavior of the unfaithfulness as a function of the total mass in Fig. 32 we appreciate that SEOBNRv5HM is overall closer to IMRPhenomTHM than to IMRPhenomXHM, as expected given the similar merger-ringdown model, and the comparable NR calibration coverage.

^[1] B. P. Abbott *et al.* (LIGO Scientific and Virgo Collaborations), Observation of gravitational waves from a binary black hole merger, Phys. Rev. Lett. **116**, 061102 (2016).

^[2] B. P. Abbott *et al.* (LIGO Scientific and Virgo Collaborations), GWTC-1: A gravitational-wave transient catalog of compact binary mergers observed by LIGO and Virgo during the first and second observing runs, Phys. Rev. X 9, 031040 (2019).

^[3] T. Venumadhav, B. Zackay, J. Roulet, L. Dai, and M. Zaldarriaga, New binary black hole mergers in the second observing run of Advanced LIGO and Advanced Virgo, Phys. Rev. D 101, 083030 (2020).

^[4] R. Abbott et al. (LIGO Scientific and Virgo Collaborations), GWTC-2: Compact binary coalescences observed by LIGO and Virgo during the first half of the third observing run, Phys. Rev. X 11, 021053 (2021).

^[5] R. Abbott *et al.* (LIGO Scientific and Virgo Collaborations), GWTC-2.1: Deep extended catalog of compact

binary coalescences observed by LIGO and Virgo during the first half of the third observing run, arXiv:2108.01045 [Phys. Rev. D (to be published)].

^[6] R. Abbott et al. (LIGO Scientific, Virgo, and KAGRA Collaborations), GWTC-3: Compact binary coalescences observed by LIGO and Virgo during the second part of the third observing run, Phys. Rev. X 13, 041039 (2023).

^[7] A. H. Nitz, C. D. Capano, S. Kumar, Y.-F. Wang, S. Kastha, M. Schäfer, R. Dhurkunde, and M. Cabero, 3-OGC: Catalog of gravitational waves from compactbinary mergers, Astrophys. J. 922, 76 (2021).

^[8] S. Olsen, T. Venumadhav, J. Mushkin, J. Roulet, B. Zackay, and M. Zaldarriaga, New binary black hole mergers in the LIGO-Virgo O3a data, Phys. Rev. D 106, 043009 (2022).

^[9] J. Aasi *et al.* (LIGO Scientific Collaboration), Advanced LIGO, Classical Quantum Gravity **32**, 074001 (2015).

- [10] F. Acernese *et al.* (Virgo Collaboration), Advanced Virgo: A second-generation interferometric gravitational wave detector, Classical Quantum Gravity **32**, 024001 (2015).
- [11] A. Buikema *et al.* (aLIGO Collaboration), Sensitivity and performance of the Advanced LIGO detectors in the third observing run, Phys. Rev. D **102**, 062003 (2020).
- [12] M. Tse et al., Quantum-enhanced Advanced LIGO detectors in the era of gravitational-wave astronomy, Phys. Rev. Lett. 123, 231107 (2019).
- [13] F. Acernese *et al.* (Virgo Collaboration), Increasing the astrophysical reach of the Advanced Virgo detector via the application of squeezed vacuum states of light, Phys. Rev. Lett. **123**, 231108 (2019).
- [14] M. Punturo *et al.*, The Einstein Telescope: A third-generation gravitational wave observatory, Classical Quantum Gravity **27**, 194002 (2010).
- [15] D. Reitze *et al.*, Cosmic Explorer: The U.S. contribution to gravitational-wave astronomy beyond LIGO, Bull. Am. Astron. Soc. **51**, 035 (2019).
- [16] M. Evans et al., A horizon study for cosmic explorer: Science, observatories, and community, arXiv:2109 09882
- [17] P. Amaro-Seoane, H. Audley, S. Babak, J. Baker, E. Barausse, P. Bender, E. Berti, P. Binetruy, M. Born, D. Bortoluzzi *et al.*, Laser interferometer space antenna, arXiv:1702.00786.
- [18] F. Pretorius, Evolution of binary black hole spacetimes, Phys. Rev. Lett. 95, 121101 (2005).
- [19] M. Campanelli, C. O. Lousto, P. Marronetti, and Y. Zlochower, Accurate evolutions of orbiting black-hole binaries without excision, Phys. Rev. Lett. 96, 111101 (2006).
- [20] J. G. Baker, J. Centrella, D.-I. Choi, M. Koppitz, and J. van Meter, Gravitational wave extraction from an inspiraling configuration of merging black holes, Phys. Rev. Lett. 96, 111102 (2006).
- [21] J. Blackman, S. E. Field, C. R. Galley, B. Szilágyi, M. A. Scheel, M. Tiglio, and D. A. Hemberger, Fast and accurate prediction of numerical relativity waveforms from binary black hole coalescences using surrogate models, Phys. Rev. Lett. 115, 121102 (2015).
- [22] J. Blackman, S. E. Field, M. A. Scheel, C. R. Galley, D. A. Hemberger, P. Schmidt, and R. Smith, A surrogate model of gravitational waveforms from numerical relativity simulations of precessing binary black hole mergers, Phys. Rev. D 95, 104023 (2017).
- [23] J. Blackman, S. E. Field, M. A. Scheel, C. R. Galley, C. D. Ott, M. Boyle, L. E. Kidder, H. P. Pfeiffer, and B. Szilágyi, Numerical relativity waveform surrogate model for generically precessing binary black hole mergers, Phys. Rev. D 96, 024058 (2017).
- [24] V. Varma, S. E. Field, M. A. Scheel, J. Blackman, L. E. Kidder, and H. P. Pfeiffer, Surrogate model of hybridized numerical relativity binary black hole waveforms, Phys. Rev. D 99, 064045 (2019).
- [25] V. Varma, S. E. Field, M. A. Scheel, J. Blackman, D. Gerosa, L. C. Stein, L. E. Kidder, and H. P. Pfeiffer, Surrogate models for precessing binary black hole simulations with unequal masses, Phys. Rev. Res. 1, 033015 (2019).

- [26] D. Williams, I.S. Heng, J. Gair, J. A. Clark, and B. Khamesra, Precessing numerical relativity waveform surrogate model for binary black holes: A Gaussian process regression approach, Phys. Rev. D 101, 063011 (2020).
- [27] N. E. M. Rifat, S. E. Field, G. Khanna, and V. Varma, Surrogate model for gravitational wave signals from comparable and large-mass-ratio black hole binaries, Phys. Rev. D 101, 081502 (2020).
- [28] T. Islam, V. Varma, J. Lodman, S. E. Field, G. Khanna, M. A. Scheel, H. P. Pfeiffer, D. Gerosa, and L. E. Kidder, Eccentric binary black hole surrogate models for the gravitational waveform and remnant properties: Comparable mass, nonspinning case, Phys. Rev. D 103, 064022 (2021).
- [29] T. Islam, S. E. Field, S. A. Hughes, G. Khanna, V. Varma, M. Giesler, M. A. Scheel, L. E. Kidder, and H. P. Pfeiffer, Surrogate model for gravitational wave signals from nonspinning, comparable-to large-mass-ratio black hole binaries built on black hole perturbation theory waveforms calibrated to numerical relativity, Phys. Rev. D 106, 104025 (2022).
- [30] J. Yoo, V. Varma, M. Giesler, M. A. Scheel, C.-J. Haster, H. P. Pfeiffer, L. E. Kidder, and M. Boyle, Targeted large mass ratio numerical relativity surrogate waveform model for GW190814, Phys. Rev. D 106, 044001 (2022).
- [31] Y. Pan, A. Buonanno, J. G. Baker, J. Centrella, B. J. Kelly, S. T. McWilliams, F. Pretorius, and J. R. van Meter, A dataanalysis driven comparison of analytic and numerical coalescing binary waveforms: Nonspinning case, Phys. Rev. D 77, 024014 (2008).
- [32] P. Ajith *et al.*, Phenomenological template family for black-hole coalescence waveforms, Classical Quantum Gravity **24**, S689 (2007).
- [33] P. Ajith *et al.*, Inspiral-merger-ringdown waveforms for black-hole binaries with nonprecessing spins, Phys. Rev. Lett. **106**, 241101 (2011).
- [34] L. Santamaria *et al.*, Matching post-Newtonian and numerical relativity waveforms: Systematic errors and a new phenomenological model for nonprecessing black hole binaries, Phys. Rev. D **82**, 064016 (2010).
- [35] M. Hannam, P. Schmidt, A. Bohé, L. Haegel, S. Husa, F. Ohme, G. Pratten, and M. Pürrer, Simple model of complete precessing black-hole-binary gravitational waveforms, Phys. Rev. Lett. 113, 151101 (2014).
- [36] S. Husa, S. Khan, M. Hannam, M. Pürrer, F. Ohme, X. Jiménez Forteza, and A. Bohé, Frequency-domain gravitational waves from nonprecessing black-hole binaries. I. New numerical waveforms and anatomy of the signal, Phys. Rev. D 93, 044006 (2016).
- [37] S. Khan, S. Husa, M. Hannam, F. Ohme, M. Pürrer, X. Jiménez Forteza, and A. Bohé, Frequency-domain gravitational waves from nonprecessing black-hole binaries. II. A phenomenological model for the advanced detector era, Phys. Rev. D 93, 044007 (2016).
- [38] T. Dietrich, S. Bernuzzi, and W. Tichy, Closed-form tidal approximants for binary neutron star gravitational waveforms constructed from high-resolution numerical relativity simulations, Phys. Rev. D **96**, 121501 (2017).
- [39] L. London, S. Khan, E. Fauchon-Jones, C. García, M. Hannam, S. Husa, X. Jiménez-Forteza, C. Kalaghatgi,

- F. Ohme, and F. Pannarale, First higher-multipole model of gravitational waves from spinning and coalescing black-hole binaries, Phys. Rev. Lett. **120**, 161102 (2018).
- [40] S. Khan, K. Chatziioannou, M. Hannam, and F. Ohme, Phenomenological model for the gravitational-wave signal from precessing binary black holes with two-spin effects, Phys. Rev. D 100, 024059 (2019).
- [41] S. Khan, F. Ohme, K. Chatziioannou, and M. Hannam, Including higher order multipoles in gravitational-wave models for precessing binary black holes, Phys. Rev. D 101, 024056 (2020).
- [42] T. Dietrich, A. Samajdar, S. Khan, N. K. Johnson-McDaniel, R. Dudi, and W. Tichy, Improving the NRTidal model for binary neutron star systems, Phys. Rev. D 100, 044003 (2019).
- [43] J. E. Thompson, E. Fauchon-Jones, S. Khan, E. Nitoglia, F. Pannarale, T. Dietrich, and M. Hannam, Modeling the gravitational wave signature of neutron star black hole coalescences, Phys. Rev. D 101, 124059 (2020).
- [44] G. Pratten, S. Husa, C. Garcia-Quiros, M. Colleoni, A. Ramos-Buades, H. Estelles, and R. Jaume, Setting the cornerstone for a family of models for gravitational waves from compact binaries: The dominant harmonic for nonprecessing quasicircular black holes, Phys. Rev. D 102, 064001 (2020).
- [45] G. Pratten et al., Computationally efficient models for the dominant and subdominant harmonic modes of precessing binary black holes, Phys. Rev. D 103, 104056 (2021).
- [46] C. García-Quirós, M. Colleoni, S. Husa, H. Estellés, G. Pratten, A. Ramos-Buades, M. Mateu-Lucena, and R. Jaume, Multimode frequency-domain model for the gravitational wave signal from nonprecessing black-hole binaries, Phys. Rev. D 102, 064002 (2020).
- [47] H. Estellés, A. Ramos-Buades, S. Husa, C. García-Quirós, M. Colleoni, L. Haegel, and R. Jaume, Phenomenological time domain model for dominant quadrupole gravitational wave signal of coalescing binary black holes, Phys. Rev. D 103, 124060 (2021).
- [48] H. Estellés, S. Husa, M. Colleoni, D. Keitel, M. Mateu-Lucena, C. García-Quirós, A. Ramos-Buades, and A. Borchers, Time-domain phenomenological model of gravitational-wave subdominant harmonics for quasicircular nonprecessing binary black hole coalescences, Phys. Rev. D 105, 084039 (2022).
- [49] H. Estellés, M. Colleoni, C. García-Quirós, S. Husa, D. Keitel, M. Mateu-Lucena, M. d. L. Planas, and A. Ramos-Buades, New twists in compact binary waveform modeling: A fast time-domain model for precession, Phys. Rev. D 105, 084040 (2022).
- [50] E. Hamilton, L. London, J. E. Thompson, E. Fauchon-Jones, M. Hannam, C. Kalaghatgi, S. Khan, F. Pannarale, and A. Vano-Vinuales, Model of gravitational waves from precessing black-hole binaries through merger and ringdown, Phys. Rev. D 104, 124027 (2021).
- [51] A. Buonanno and T. Damour, Effective one-body approach to general relativistic two-body dynamics, Phys. Rev. D 59, 084006 (1999).
- [52] A. Buonanno and T. Damour, Transition from inspiral to plunge in binary black hole coalescences, Phys. Rev. D 62, 064015 (2000).

- [53] T. Damour, P. Jaranowski, and G. Schaefer, On the determination of the last stable orbit for circular general relativistic binaries at the third post-Newtonian approximation, Phys. Rev. D 62, 084011 (2000).
- [54] T. Damour, Coalescence of two spinning black holes: An effective one-body approach, Phys. Rev. D 64, 124013 (2001).
- [55] A. Buonanno, Y. Chen, and T. Damour, Transition from inspiral to plunge in precessing binaries of spinning black holes, Phys. Rev. D 74, 104005 (2006).
- [56] A. Buonanno, G.B. Cook, and F. Pretorius, Inspiral, merger and ring-down of equal-mass black-hole binaries, Phys. Rev. D 75, 124018 (2007).
- [57] A. Buonanno, Y. Pan, J. G. Baker, J. Centrella, B. J. Kelly, S. T. McWilliams, and J. R. van Meter, Toward faithful templates for nonspinning binary black holes using the effective-one-body approach, Phys. Rev. D 76, 104049 (2007).
- [58] T. Damour and A. Nagar, Comparing effective-one-body gravitational waveforms to accurate numerical data, Phys. Rev. D 77, 024043 (2008).
- [59] T. Damour, B. R. Iyer, and A. Nagar, Improved resummation of post-Newtonian multipolar waveforms from circularized compact binaries, Phys. Rev. D 79, 064004 (2009).
- [60] A. Buonanno, Y. Pan, H. P. Pfeiffer, M. A. Scheel, L. T. Buchman, and L. E. Kidder, Effective-one-body waveforms calibrated to numerical relativity simulations: Coalescence of nonspinning, equal-mass black holes, Phys. Rev. D 79, 124028 (2009).
- [61] Y. Pan, A. Buonanno, M. Boyle, L. T. Buchman, L. E. Kidder, H. P. Pfeiffer, and M. A. Scheel, Inspiral-merger-ringdown multipolar waveforms of nonspinning black-hole binaries using the effective-one-body formalism, Phys. Rev. D 84, 124052 (2011).
- [62] T. Damour, A. Nagar, and S. Bernuzzi, Improved effective-one-body description of coalescing nonspinning black-hole binaries and its numerical-relativity completion, Phys. Rev. D 87, 084035 (2013).
- [63] T. Damour, P. Jaranowski, and G. Schäfer, Fourth post-Newtonian effective one-body dynamics, Phys. Rev. D 91, 084024 (2015).
- [64] A. Nagar, G. Pratten, G. Riemenschneider, and R. Gamba, Multipolar effective one body model for nonspinning black hole binaries, Phys. Rev. D 101, 024041 (2020).
- [65] T. Damour, A. Nagar, E. N. Dorband, D. Pollney, and L. Rezzolla, Faithful effective-one-body waveforms of equal-mass coalescing black-hole binaries, Phys. Rev. D 77, 084017 (2008).
- [66] T. Damour, P. Jaranowski, and G. Schaefer, Effective one body approach to the dynamics of two spinning black holes with next-to-leading order spin-orbit coupling, Phys. Rev. D 78, 024009 (2008).
- [67] Y. Pan, A. Buonanno, L. T. Buchman, T. Chu, L. E. Kidder, H. P. Pfeiffer, and M. A. Scheel, Effective-one-body waveforms calibrated to numerical relativity simulations: Coalescence of nonprecessing, spinning, equal-mass black holes, Phys. Rev. D 81, 084041 (2010).
- [68] T. Damour, A. Nagar, M. Hannam, S. Husa, and B. Bruegmann, Accurate effective-one-body waveforms of

- inspiralling and coalescing black-hole binaries, Phys. Rev. D 78, 044039 (2008).
- [69] E. Barausse and A. Buonanno, An improved effective-one-body Hamiltonian for spinning black-hole binaries, Phys. Rev. D 81, 084024 (2010).
- [70] E. Barausse and A. Buonanno, Extending the effectiveone-body Hamiltonian of black-hole binaries to include next-to-next-to-leading spin-orbit couplings, Phys. Rev. D 84, 104027 (2011).
- [71] A. Nagar, Effective one-body Hamiltonian of two spinning black-holes with next-to-next-to-leading order spin-orbit coupling, Phys. Rev. D 84, 084028 (2011); 88, 089901(E) (2013).
- [72] T. Damour and A. Nagar, New effective-one-body description of coalescing nonprecessing spinning black-hole binaries, Phys. Rev. D 90, 044018 (2014).
- [73] S. Balmelli and T. Damour, New effective-one-body Hamiltonian with next-to-leading order spin-spin coupling, Phys. Rev. D **92**, 124022 (2015).
- [74] M. Khalil, J. Steinhoff, J. Vines, and A. Buonanno, Fourth post-Newtonian effective-one-body Hamiltonians with generic spins, Phys. Rev. D 101, 104034 (2020).
- [75] A. Taracchini, Y. Pan, A. Buonanno, E. Barausse, M. Boyle, T. Chu, G. Lovelace, H.P. Pfeiffer, and M.A. Scheel, Prototype effective-one-body model for nonprecessing spinning inspiral-merger-ringdown waveforms, Phys. Rev. D 86, 024011 (2012).
- [76] A. Taracchini *et al.*, Effective-one-body model for black-hole binaries with generic mass ratios and spins, Phys. Rev. D **89**, 061502 (2014).
- [77] A. Bohé et al., Improved effective-one-body model of spinning, nonprecessing binary black holes for the era of gravitational-wave astrophysics with advanced detectors, Phys. Rev. D 95, 044028 (2017).
- [78] R. Cotesta, A. Buonanno, A. Bohé, A. Taracchini, I. Hinder, and S. Ossokine, Enriching the symphony of gravitational waves from binary black holes by tuning higher harmonics, Phys. Rev. D 98, 084028 (2018).
- [79] Y. Pan, A. Buonanno, A. Taracchini, L. E. Kidder, A. H. Mroué, H. P. Pfeiffer, M. A. Scheel, and B. Szilágyi, Inspiral-merger-ringdown waveforms of spinning, precessing black-hole binaries in the effective-one-body formalism, Phys. Rev. D 89, 084006 (2014).
- [80] S. Babak, A. Taracchini, and A. Buonanno, Validating the effective-one-body model of spinning, precessing binary black holes against numerical relativity, Phys. Rev. D 95, 024010 (2017).
- [81] S. Ossokine *et al.*, Multipolar effective-one-body waveforms for precessing binary black holes: Construction and validation, Phys. Rev. D **102**, 044055 (2020).
- [82] A. Nagar, F. Messina, P. Rettegno, D. Bini, T. Damour, A. Geralico, S. Akcay, and S. Bernuzzi, Nonlinear-in-spin effects in effective-one-body waveform models of spin-aligned, inspiralling, neutron star binaries, Phys. Rev. D 99, 044007 (2019).
- [83] A. Nagar *et al.*, Time-domain effective-one-body gravitational waveforms for coalescing compact binaries with nonprecessing spins, tides and self-spin effects, Phys. Rev. D **98**, 104052 (2018).

- [84] S. Akcay, R. Gamba, and S. Bernuzzi, Hybrid post-Newtonian effective-one-body scheme for spin-precessing compact-binary waveforms up to merger, Phys. Rev. D 103, 024014 (2021).
- [85] R. Gamba, S. Akçay, S. Bernuzzi, and J. Williams, Effective-one-body waveforms for precessing coalescing compact binaries with post-Newtonian twist, Phys. Rev. D 106, 024020 (2022).
- [86] D. Bini and T. Damour, Gravitational radiation reaction along general orbits in the effective one-body formalism, Phys. Rev. D 86, 124012 (2012).
- [87] T. Hinderer and S. Babak, Foundations of an effective-one-body model for coalescing binaries on eccentric orbits, Phys. Rev. D 96, 104048 (2017).
- [88] D. Chiaramello and A. Nagar, Faithful analytical effectiveone-body waveform model for spin-aligned, moderately eccentric, coalescing black hole binaries, Phys. Rev. D 101, 101501 (2020).
- [89] A. Nagar, A. Bonino, and P. Rettegno, Effective one-body multipolar waveform model for spin-aligned, quasicircular, eccentric, hyperbolic black hole binaries, Phys. Rev. D 103, 104021 (2021).
- [90] M. Khalil, A. Buonanno, J. Steinhoff, and J. Vines, Radiation-reaction force and multipolar waveforms for eccentric, spin-aligned binaries in the effective-one-body formalism, Phys. Rev. D 104, 024046 (2021).
- [91] A. Ramos-Buades, A. Buonanno, M. Khalil, and S. Ossokine, Effective-one-body multipolar waveforms for eccentric binary black holes with nonprecessing spins, Phys. Rev. D 105, 044035 (2022).
- [92] S. Albanesi, A. Placidi, A. Nagar, M. Orselli, and S. Bernuzzi, New avenue for accurate analytical waveforms and fluxes for eccentric compact binaries, Phys. Rev. D 105, L121503 (2022).
- [93] S. Bernuzzi, A. Nagar, T. Dietrich, and T. Damour, Modeling the dynamics of tidally interacting binary neutron stars up to the merger, Phys. Rev. Lett. 114, 161103 (2015).
- [94] T. Hinderer et al., Effects of neutron-star dynamic tides on gravitational waveforms within the effective-one-body approach, Phys. Rev. Lett. 116, 181101 (2016).
- [95] J. Steinhoff, T. Hinderer, A. Buonanno, and A. Taracchini, Dynamical tides in general relativity: Effective action and effective-one-body Hamiltonian, Phys. Rev. D 94, 104028 (2016)
- [96] S. Akcay, S. Bernuzzi, F. Messina, A. Nagar, N. Ortiz, and P. Rettegno, Effective-one-body multipolar waveform for tidally interacting binary neutron stars up to merger, Phys. Rev. D 99, 044051 (2019).
- [97] J. Steinhoff, T. Hinderer, T. Dietrich, and F. Foucart, Spin effects on neutron star fundamental-mode dynamical tides: Phenomenology and comparison to numerical simulations, Phys. Rev. Res. 3, 033129 (2021).
- [98] A. Matas et al., Aligned-spin neutron-star-black-hole waveform model based on the effective-one-body approach and numerical-relativity simulations, Phys. Rev. D 102, 043023 (2020).
- [99] A. Gonzalez, R. Gamba, M. Breschi, F. Zappa, G. Carullo, S. Bernuzzi, and A. Nagar, Numerical-relativity-informed effective-one-body model for black-hole-neutron-star

- mergers with higher modes and spin precession, Phys. Rev. D **107**, 084026 (2023).
- [100] S. E. Field, C. R. Galley, J. S. Hesthaven, J. Kaye, and M. Tiglio, Fast prediction and evaluation of gravitational waveforms using surrogate models, Phys. Rev. X 4, 031006 (2014).
- [101] M. Pürrer, Frequency domain reduced order models for gravitational waves from aligned-spin compact binaries, Classical Quantum Gravity 31, 195010 (2014).
- [102] M. Pürrer, Frequency domain reduced order model of aligned-spin effective-one-body waveforms with generic mass-ratios and spins, Phys. Rev. D 93, 064041 (2016).
- [103] B. D. Lackey, S. Bernuzzi, C. R. Galley, J. Meidam, and C. Van Den Broeck, Effective-one-body waveforms for binary neutron stars using surrogate models, Phys. Rev. D 95, 104036 (2017).
- [104] B. D. Lackey, M. Pürrer, A. Taracchini, and S. Marsat, Surrogate model for an aligned-spin effective one body waveform model of binary neutron star inspirals using Gaussian process regression, Phys. Rev. D 100, 024002 (2019).
- [105] R. Cotesta, S. Marsat, and M. Pürrer, Frequency domain reduced order model of aligned-spin effective-one-body waveforms with higher-order modes, Phys. Rev. D 101, 124040 (2020).
- [106] B. Gadre, M. Pürrer, S. E. Field, S. Ossokine, and V. Varma, A fully precessing higher-mode surrogate model of effective-one-body waveforms, arXiv:2203.00381.
- [107] J. Tissino, G. Carullo, M. Breschi, R. Gamba, S. Schmidt, and S. Bernuzzi, Combining effective-one-body accuracy and reduced-order-quadrature speed for binary neutron star merger parameter estimation with machine learning, Phys. Rev. D 107, 084037 (2023).
- [108] S. Khan and R. Green, Gravitational-wave surrogate models powered by artificial neural networks, Phys. Rev. D 103, 064015 (2021).
- [109] L. M. Thomas, G. Pratten, and P. Schmidt, Accelerating multimodal gravitational waveforms from precessing compact binaries with artificial neural networks, Phys. Rev. D 106, 104029 (2022).
- [110] M. Dax, S. R. Green, J. Gair, J. H. Macke, A. Buonanno, and B. Schölkopf, Real-time gravitational wave science with neural posterior estimation, Phys. Rev. Lett. 127, 241103 (2021).
- [111] M. Dax, S. R. Green, J. Gair, M. Pürrer, J. Wildberger, J. H. Macke, A. Buonanno, and B. Schölkopf, Neural importance sampling for rapid and reliable gravitational-wave inference, Phys. Rev. Lett. 130, 171403 (2023).
- [112] D. P. Mihaylov, S. Ossokine, A. Buonanno, and A. Ghosh, Fast post-adiabatic waveforms in the time domain: Applications to compact binary coalescences in LIGO and Virgo, Phys. Rev. D **104**, 124087 (2021).
- [113] A. Nagar, G. Riemenschneider, G. Pratten, P. Rettegno, and F. Messina, Multipolar effective one body waveform model for spin-aligned black hole binaries, Phys. Rev. D **102**, 024077 (2020).
- [114] G. Riemenschneider, P. Rettegno, M. Breschi, A. Albertini, R. Gamba, S. Bernuzzi, and A. Nagar, Assessment of consistent next-to-quasicircular corrections and postadiabatic

- approximation in effective-one-body multipolar waveforms for binary black hole coalescences, Phys. Rev. D 104, 104045 (2021).
- [115] https://observing.docs.ligo.org/plan/ (accessed: 2023-02-25).
- [116] T. Akutsu et al. (KAGRA Collaboration), Overview of KAGRA: Detector design and construction history, Prog. Theor. Exp. Phys. 2021, 05A101 (2021).
- [117] G. Pratten, P. Schmidt, R. Buscicchio, and L. M. Thomas, Measuring precession in asymmetric compact binaries, Phys. Rev. Res. **2**, 043096 (2020).
- [118] M. Colleoni, M. Mateu-Lucena, H. Estellés, C. García-Quirós, D. Keitel, G. Pratten, A. Ramos-Buades, and S. Husa, Towards the routine use of subdominant harmonics in gravitational-wave inference: Reanalysis of GW 190412 with generation X waveform models, Phys. Rev. D 103, 024029 (2021).
- [119] T. Damour, Gravitational scattering, post-Minkowskian approximation and effective one-body theory, Phys. Rev. D **94**, 104015 (2016).
- [120] T. Damour, High-energy gravitational scattering and the general relativistic two-body problem, Phys. Rev. D 97, 044038 (2018).
- [121] A. Antonelli, A. Buonanno, J. Steinhoff, M. van de Meent, and J. Vines, Energetics of two-body Hamiltonians in post-Minkowskian gravity, Phys. Rev. D 99, 104004 (2019).
- [122] P. H. Damgaard and P. Vanhove, Remodeling the effective one-body formalism in post-Minkowskian gravity, Phys. Rev. D 104, 104029 (2021).
- [123] M. Khalil, A. Buonanno, J. Steinhoff, and J. Vines, Energetics and scattering of gravitational two-body systems at fourth post-Minkowskian order, Phys. Rev. D 106, 024042 (2022).
- [124] T. Damour and P. Rettegno, Strong-field scattering of two black holes: Numerical relativity meets post-Minkowskian gravity, Phys. Rev. D **107**, 064051 (2023).
- [125] M. van de Meent, A. Buonanno, D. P. Mihaylov, S. Ossokine, L. Pompili, N. Warburton, A. Pound, B. Wardell, L. Durkan, and J. Miller, this issue, Enhancing the SEOBNRv5 effective-one-body waveform model with second-order gravitational self-force fluxes, Phys. Rev. D 108, 124038 (2023).
- [126] M. Khalil, A. Buonanno, H. Estellés, D. P. Mihaylov, S. Ossokine, L. Pompili, and A. Ramos-Buades, following paper, Theoretical groundwork supporting the precessing-spin two-body dynamics of the effective-one-body waveform models SEOBNRv5, Phys. Rev. D 108, 124036 (2023).
- [127] Q. Henry, S. Marsat, and M. Khalil, Spin contributions to the gravitational-waveform modes for spin-aligned binaries at the 3.5PN order, Phys. Rev. D 106, 124018 (2022).
- [128] N. Warburton, A. Pound, B. Wardell, J. Miller, and L. Durkan, Gravitational-wave energy flux for compact binaries through second order in the mass ratio, Phys. Rev. Lett. 127, 151102 (2021).
- [129] B. Wardell, A. Pound, N. Warburton, J. Miller, L. Durkan, and A. Le Tiec, Gravitational waveforms for compact binaries from second-order self-force theory, Phys. Rev. Lett. 130, 241402 (2023).
- [130] http://www.black-holes.org/waveforms.

- [131] M. Boyle *et al.*, The SXS Collaboration catalog of binary black hole simulations, Classical Quantum Gravity **36**, 195006 (2019).
- [132] T. Chu, H. Fong, P. Kumar, H. P. Pfeiffer, M. Boyle, D. A. Hemberger, L. E. Kidder, M. A. Scheel, and B. Szilagyi, On the accuracy and precision of numerical waveforms: Effect of waveform extraction methodology, Classical Quantum Gravity 33, 165001 (2016).
- [133] D. A. Hemberger, G. Lovelace, T. J. Loredo, L. E. Kidder, M. A. Scheel, B. Szilagyi, N. W. Taylor, and S. A. Teukolsky, Final spin and radiated energy in numerical simulations of binary black holes with equal masses and equal, aligned or anti-aligned spins, Phys. Rev. D 88, 064014 (2013).
- [134] M. A. Scheel, M. Giesler, D. A. Hemberger, G. Lovelace, K. Kuper, M. Boyle, B. Szilagyi, and L. E. Kidder, Improved methods for simulating nearly extremal binary black holes, Classical Quantum Gravity 32, 105009 (2015).
- [135] G. Lovelace et al., Nearly extremal apparent horizons in simulations of merging black holes, Classical Quantum Gravity 32, 065007 (2015).
- [136] B. P. Abbott *et al.* (Virgo and LIGO Scientific Collaborations), Directly comparing GW150914 with numerical solutions of Einstein's equations for binary black hole coalescence, Phys. Rev. D **94**, 064035 (2016).
- [137] G. Lovelace et al., Modeling the source of GW150914 with targeted numerical-relativity simulations, Classical Quantum Gravity 33, 244002 (2016).
- [138] B. P. Abbott *et al.* (Virgo and LIGO Scientific Collaborations), GW151226: Observation of gravitational waves from a 22-solar-mass binary black hole coalescence, Phys. Rev. Lett. 116, 241103 (2016).
- [139] P. Kumar, K. Barkett, S. Bhagwat, N. Afshari, D. A. Brown, G. Lovelace, M. A. Scheel, and B. Szilagyi, Accuracy and precision of gravitational-wave models of inspiraling neutron star-black hole binaries with spin: Comparison with matter-free numerical relativity in the low-frequency regime, Phys. Rev. D 92, 102001 (2015).
- [140] A. H. Mroue *et al.*, Catalog of 174 binary black hole simulations for gravitational wave astronomy, Phys. Rev. Lett. 111, 241104 (2013).
- [141] R. Haas *et al.*, The Einstein Toolkit (2022), to find out more, visit http://einsteintoolkit.org.
- [142] E. Barausse, A. Buonanno, S. A. Hughes, G. Khanna, S. O'Sullivan, and Y. Pan, Modeling multipolar gravitational-wave emission from small mass-ratio mergers, Phys. Rev. D **85**, 024046 (2012).
- [143] A. Taracchini, A. Buonanno, G. Khanna, and S. A. Hughes, Small mass plunging into a Kerr black hole: Anatomy of the inspiral-merger-ringdown waveforms, Phys. Rev. D 90, 084025 (2014).
- [144] D. P. Mihaylov, S. Ossokine, A. Buonanno, H. Estelles, L. Pompili, M. Pürrer, and A. Ramos-Buades, pySEOBNR: A software package for the next generation of effective-one-body multipolar waveform models, arXiv:2303.18203.
- [145] A. Ramos-Buades, A. Buonanno, H. Estellés, M. Khalil, D. P. Mihaylov, S. Ossokine, L. Pompili, and M. Shiferaw, this issue, Next generation of accurate and

- efficient multipolar precessing-spin effective-one-body waveforms for binary black holes, Phys. Rev. D **108**, 124037 (2023).
- [146] E. Barausse, E. Racine, and A. Buonanno, Hamiltonian of a spinning test-particle in curved spacetime, Phys. Rev. D 80, 104025 (2009); 85, 069904(E) (2012).
- [147] J. Vines, D. Kunst, J. Steinhoff, and T. Hinderer, Canonical Hamiltonian for an extended test body in curved spacetime: To quadratic order in spin, Phys. Rev. D 93, 103008 (2016); 104, 029902(E) (2021).
- [148] T. Damour and A. Nagar, Faithful effective-one-body waveforms of small-mass-ratio coalescing black-hole binaries, Phys. Rev. D 76, 064028 (2007).
- [149] D. Bini, T. Damour, and A. Geralico, Novel approach to binary dynamics: Application to the fifth post-Newtonian level, Phys. Rev. Lett. 123, 231104 (2019).
- [150] D. Bini, T. Damour, and A. Geralico, Binary dynamics at the fifth and fifth-and-a-half post-Newtonian orders, Phys. Rev. D 102, 024062 (2020).
- [151] L. Barack and N. Sago, Gravitational self-force on a particle in eccentric orbit around a Schwarzschild black hole, Phys. Rev. D 81, 084021 (2010).
- [152] S. Akcay, L. Barack, T. Damour, and N. Sago, Gravitational self-force and the effective-one-body formalism between the innermost stable circular orbit and the light ring, Phys. Rev. D 86, 104041 (2012).
- [153] S. Isoyama, L. Barack, S. R. Dolan, A. Le Tiec, H. Nakano, A. G. Shah, T. Tanaka, and N. Warburton, Gravitational self-force correction to the innermost stable circular equatorial orbit of a Kerr black hole, Phys. Rev. Lett. 113, 161101 (2014).
- [154] A. Antonelli, C. Kavanagh, M. Khalil, J. Steinhoff, and J. Vines, Gravitational spin-orbit coupling through third-subleading post-Newtonian order: From first-order self-force to arbitrary mass ratios, Phys. Rev. Lett. 125, 011103 (2020).
- [155] A. Antonelli, C. Kavanagh, M. Khalil, J. Steinhoff, and J. Vines, Gravitational spin-orbit and aligned spin₁-spin₂ couplings through third-subleading post-Newtonian orders, Phys. Rev. D 102, 124024 (2020).
- [156] M. K. Mandal, P. Mastrolia, R. Patil, and J. Steinhoff, Gravitational spin-orbit Hamiltonian at NNNLO in the post-Newtonian framework, J. High Energy Phys. 03 (2023) 130.
- [157] J.-W. Kim, M. Levi, and Z. Yin, N³LO spin-orbit interaction via the EFT of spinning gravitating objects, J. High Energy Phys. 05 (2023) 184.
- [158] J. Vines and J. Steinhoff, Spin-multipole effects in binary black holes and the test-body limit, Phys. Rev. D 97, 064010 (2018).
- [159] Y. Pan, A. Buonanno, R. Fujita, E. Racine, and H. Tagoshi, Post-Newtonian factorized multipolar waveforms for spinning, non-precessing black-hole binaries, Phys. Rev. D 83, 064003 (2011); 87, 109901(E) (2013).
- [160] A. Nagar and P. Rettegno, Efficient effective one body time-domain gravitational waveforms, Phys. Rev. D 99, 021501 (2019).
- [161] P. Rettegno, F. Martinetti, A. Nagar, D. Bini, G. Riemenschneider, and T. Damour, Comparing effective

- one body Hamiltonians for spin-aligned coalescing binaries, Phys. Rev. D **101**, 104027 (2020).
- [162] L. Blanchet, Gravitational wave tails of tails, Classical Quantum Gravity 15, 113 (1998); 22, 3381(E) (2005).
- [163] L. Blanchet, G. Faye, B. R. Iyer, and S. Sinha, The third post-Newtonian gravitational wave polarisations and associated spherical harmonic modes for inspiralling compact binaries in quasicircular orbits, Classical Quantum Gravity 25, 165003 (2008); 29, 239501(E) (2012).
- [164] Q. Henry, Complete gravitational-waveform amplitude modes for quasicircular compact binaries to the 3.5PN order, Phys. Rev. D 107, 044057 (2023).
- [165] J. M. Bardeen, W. H. Press, and S. A. Teukolsky, Rotating black holes: Locally nonrotating frames, energy extraction, and scalar synchrotron radiation, Astrophys. J. 178, 347 (1972).
- [166] X. Jiménez-Forteza, D. Keitel, S. Husa, M. Hannam, S. Khan, and M. Pürrer, Hierarchical data-driven approach to fitting numerical relativity data for nonprecessing binary black holes with an application to final spin and radiated energy, Phys. Rev. D 95, 064024 (2017).
- [167] F. Hofmann, E. Barausse, and L. Rezzolla, The final spin from binary black holes in quasicircular orbits, Astrophys. J. Lett. 825, L19 (2016).
- [168] R. H. Price and G. Khanna, Arrival times of gravitational radiation peaks for binary inspiral, Phys. Rev. D 94, 104026 (2016).
- [169] L. C. Stein, QNM: A Python package for calculating Kerr quasinormal modes, separation constants, and sphericalspheroidal mixing coefficients, J. Open Source Software 4, 1683 (2019).
- [170] I. Guyon, J. Weston, S. Barnhill, and V. Vapnik, Gene selection for cancer classification using support vector machines, Mach. Learn. 46, 389 (2002).
- [171] B. J. Kelly and J. G. Baker, Decoding mode mixing in black-hole merger ringdown, Phys. Rev. D 87, 084004 (2013).
- [172] E. Berti, V. Cardoso, and M. Casals, Eigenvalues and eigenfunctions of spin-weighted spheroidal harmonics in four and higher dimensions, Phys. Rev. D 73, 024013 (2006); 73, 109902(E) (2006).
- [173] E. Berti and A. Klein, Mixing of spherical and spheroidal modes in perturbed Kerr black holes, Phys. Rev. D 90, 064012 (2014).
- [174] L. London and E. Fauchon-Jones, On modeling for Kerr black holes: Basis learning, QNM frequencies, and spherical-spheroidal mixing coefficients, Classical Quantum Gravity **36**, 235015 (2019).
- [175] A. Kumar Mehta, P. Tiwari, N. K. Johnson-McDaniel, C. K. Mishra, V. Varma, and P. Ajith, Including mode mixing in a higher-multipole model for gravitational waveforms from nonspinning black-hole binaries, Phys. Rev. D 100, 024032 (2019).
- [176] A. Nagar and P. Rettegno, Next generation: Impact of highorder analytical information on effective one body waveform models for noncircularized, spin-aligned black hole binaries, Phys. Rev. D **104**, 104004 (2021).

- [177] L. S. Finn and D. F. Chernoff, Observing binary inspiral in gravitational radiation: One interferometer, Phys. Rev. D 47, 2198 (1993).
- [178] B. S. Sathyaprakash and S. V. Dhurandhar, Choice of filters for the detection of gravitational waves from coalescing binaries, Phys. Rev. D 44, 3819 (1991).
- [179] L. Barsotti, P. Fritschel, M. Evans, and S. Gras (LIGO Collaboration), Updated Advanced LIGO sensitivity design curve (2018), LIGO Document T1800044-v5.
- [180] D. J. A. McKechan, C. Robinson, and B. S. Sathyaprakash, A tapering window for time-domain templates and simulated signals in the detection of gravitational waves from coalescing compact binaries, Classical Quantum Gravity **27**, 084020 (2010).
- [181] M. Pürrer and C.-J. Haster, Gravitational waveform accuracy requirements for future ground-based detectors, Phys. Rev. Res. 2, 023151 (2020).
- [182] J. Skilling, Nested sampling for general Bayesian computation, Bayesian Anal. 1, 833 (2006).
- [183] M. J. Williams, J. Veitch, and C. Messenger, Nested sampling with normalizing flows for gravitational-wave inference, Phys. Rev. D 103, 103006 (2021).
- [184] G. Ashton *et al.*, Bilby: A user-friendly Bayesian inference library for gravitational-wave astronomy, Astrophys. J. Suppl. Ser. **241**, 27 (2019).
- [185] D. Foreman-Mackey, D. W. Hogg, D. Lang, and J. Goodman, EMCEE: The MCMC Hammer, Publ. Astron. Soc. Pac. 125, 306 (2013).
- [186] C. Capano, Y. Pan, and A. Buonanno, Impact of higher harmonics in searching for gravitational waves from non-spinning binary black holes, Phys. Rev. D **89**, 102003 (2014).
- [187] M. K. Mandal, P. Mastrolia, R. Patil, and J. Steinhoff, Gravitational quadratic-in-spin Hamiltonian at NNNLO in the post-Newtonian framework, J. High Energy Phys. 07 (2023) 128.
- [188] J.-W. Kim, M. Levi, and Z. Yin, N³LO quadratic-in-spin interactions for generic compact binaries, J. High Energy Phys. 03 (2023) 098.
- [189] M. Levi, R. Morales, and Z. Yin, From the EFT of spinning gravitating objects to Poincaré and gauge invariance, J. High Energy Phys. 09 (2023) 090.
- [190] M. Levi and Z. Yin, Completing the fifth PN precision frontier via the EFT of spinning gravitating objects, J. High Energy Phys. 04 (2023) 079.
- [191] M. Levi, S. Mougiakakos, and M. Vieira, Gravitational cubic-in-spin interaction at the next-to-leading post-Newtonian order, J. High Energy Phys. 01 (2019) 036.
- [192] M. Levi and F. Teng, NLO gravitational quartic-in-spin interaction, J. High Energy Phys. 01 (2020) 066.
- [193] M. Boyle, A. Buonanno, L. E. Kidder, A. H. Mroue, Y. Pan, H. P. Pfeiffer, and M. A. Scheel, High-accuracy numerical simulation of black-hole binaries: Computation of the gravitational-wave energy flux and comparisons with post-Newtonian approximants, Phys. Rev. D 78, 104020 (2008).

- [194] A. Albertini, A. Nagar, P. Rettegno, S. Albanesi, and R. Gamba, Waveforms and fluxes: Towards a self-consistent effective one body waveform model for nonprecessing, coalescing black-hole binaries for third generation detectors, Phys. Rev. D 105, 084025 (2022).
- [195] T. Damour, A. Nagar, D. Pollney, and C. Reisswig, Energy versus angular momentum in black hole binaries, Phys. Rev. Lett. 108, 131101 (2012).
- [196] A. Nagar, T. Damour, C. Reisswig, and D. Pollney, Energetics and phasing of nonprecessing spinning coalescing black hole binaries, Phys. Rev. D 93, 044046 (2016).
- [197] S. Ossokine, T. Dietrich, E. Foley, R. Katebi, and G. Lovelace, Assessing the energetics of spinning binary black hole systems, Phys. Rev. D 98, 104057 (2018).
- [198] T. Dietrich, S. Bernuzzi, M. Ujevic, and W. Tichy, Gravitational waves and mass ejecta from binary neutron star mergers: Effect of the stars' rotation, Phys. Rev. D 95, 044045 (2017).
- [199] LIGO Scientific Collaboration, LIGO Algorithm Library— LALSuite, free software (GPL) (2018).
- [200] S. Behnel, R. Bradshaw, C. Citro, L. Dalcin, D. S. Seljebotn, and K. Smith, Cython: The best of both worlds, Comput. Sci. Eng. 13, 31 (2011).
- [201] S. K. Lam, A. Pitrou, and S. Seibert, Numba: A LLVM-based Python JIT compiler, in *Proceedings of the Second Workshop on the LLVM Compiler Infrastructure in HPC, LLVM '15* (Association for Computing Machinery, New York, NY, USA, 2015).
- [202] https://github.com/pydata/numexpr.
- [203] C. R. Harris *et al.*, Array programming with NumPy, Nature (London) **585**, 357 (2020).
- [204] E. Thrane and C. Talbot, An introduction to Bayesian inference in gravitational-wave astronomy: Parameter estimation, model selection, and hierarchical models, Publ. Astron. Soc. Aust. 36, e010 (2019); 37, e036(E) (2020).
- [205] G. Ashton and C. Talbot, Bilby-MCMC: An MCMC sampler for gravitational-wave inference, Mon. Not. R. Astron. Soc. 507, 2037 (2021).
- [206] M. J. Williams, J. Veitch, and C. Messenger, Importance nested sampling with normalising flows, Mach. Learn. Sci. Tech. 4, 035011 (2023).
- [207] J. S. Speagle, DYNESTY: A dynamic nested sampling package for estimating Bayesian posteriors and evidences, Mon. Not. R. Astron. Soc. 493, 3132 (2020).
- [208] T. Callister, A thesaurus for common priors in gravitational-wave astronomy, arXiv:2104.09508.

- [209] K. Chatziioannou et al., On the properties of the massive binary black hole merger GW170729, Phys. Rev. D 100, 104015 (2019).
- [210] R. Abbott *et al.* (LIGO Scientific and Virgo Collaborations), GW190814: Gravitational waves from the coalescence of a 23 solar mass black hole with a 2.6 solar mass compact object, Astrophys. J. Lett. **896**, L44 (2020).
- [211] R. Abbott *et al.* (LIGO Scientific and Virgo Collaborations), Open data from the first and second observing runs of Advanced LIGO and Advanced Virgo, SoftwareX 13, 100658 (2021).
- [212] Z. Doctor, B. Farr, D. E. Holz, and M. Pürrer, Statistical gravitational waveform models: What to simulate next?, Phys. Rev. D 96, 123011 (2017).
- [213] Y. E. Setyawati, M. Pürrer, and F. Ohme, Regression methods in waveform modeling: A comparative study, Classical Quantum Gravity 37, 075012 (2020).
- [214] S. Hild *et al.*, Sensitivity studies for third-generation gravitational wave observatories, Classical Quantum Gravity 28, 094013 (2011).
- [215] R. Abbott *et al.* (LIGO Scientific and Virgo Collaborations), Tests of general relativity with binary black holes from the second LIGO-Virgo gravitational-wave transient catalog, Phys. Rev. D **103**, 122002 (2021).
- [216] R. Abbott et al. (LIGO Scientific, Virgo, and KAGRA Collaborations), Tests of general relativity with GWTC-3, arXiv:2112.06861 [Phys. Rev. D (to be published)].
- [217] A. Ghosh, R. Brito, and A. Buonanno, Constraints on quasinormal-mode frequencies with LIGO-Virgo binary–black-hole observations, Phys. Rev. D 103, 124041 (2021).
- [218] A. K. Mehta, A. Buonanno, R. Cotesta, A. Ghosh, N. Sennett, and J. Steinhoff, Tests of general relativity with gravitational-wave observations using a flexible theory-independent method, Phys. Rev. D 107, 044020 (2023).
- [219] E. Maggio, H. O. Silva, A. Buonanno, and A. Ghosh, Tests of general relativity in the nonlinear regime: A parametrized plunge-merger-ringdown gravitational waveform model, Phys. Rev. D 108, 024043 (2023).
- [220] D. Ferguson, K. Jani, P. Laguna, and D. Shoemaker, Assessing the readiness of numerical relativity for LISA and 3G detectors, Phys. Rev. D 104, 044037 (2021).
- [221] https://git.ligo.org/waveforms/software/pyseobnr.
- [222] https://gwosc.org/.
- [223] D. Bini, T. Damour, and A. Geralico, Sixth post-Newtonian nonlocal-in-time dynamics of binary systems, Phys. Rev. D 102, 084047 (2020).